University of California, Santa Cruz

A Multi-Catalytic Approach to Reactive Oxygen Species Generation for Direct Water Disinfection

A dissertation submitted in partial satisfaction

of the requirements for the degree of

DOCTOR OF PHILOSOPHY

in

CHEMISTRY

by

John Tressel

June 2026

The Dissertation of John Tressel approved:

_____
Professor Shaowei Chen, Chair

_____
Professor Alexander Ayzner

_____
Professor Ted Holman

_____
Peter F. Biehl

Vice Provost and Dean of Graduate Studies

Table of Contents

LIST OF FIGURES

Chapter 2

Figure 11. Growth curves of *E. coli* (a) in the absence of catalysts under visible light irradiation for up to 3 h and (b,c) in the presence of TiO_2-600 but (b) in the dark and (c) under visible light irradiation for up to 3 h.

Figure 12. White light *E. coli* growth curves under white light irradiation in the presence of (a) P25, (b) TiO_2-TF, (c) TiO_2-200, (d) TiO_2-300, (e) TiO_2-400, and (f) TiO_2-500.

Figure 13. Lag phase delays for all samples after 150 minutes of white light irradiation calculated from White *E. coli* growth curves.

Figure 14. Photocatalytic degradation of methylene blue dye degradation in the absence and presence of varied samples under (a) white light irradiation and (b) as a dark control for 120 minutes.

Figure 15. SEM images of *E. coli* in the presence of TiO_2-600 (a,b) after 3 h in the dark and (c,d) after 3 h of visible light irradiation. Panels (a, c) are the secondary electron images and (b, d) are the backscattered electron image.

Figure 16. EPR spectra of the sample series with DMPO as the spin trap before (dotted curves) and after (solid curves) visible light irradiation for 3 h.

Figure 16. Growth curves of *E. coli* (a) under sonication for 2 h in the absence of catalysts, as well as in the presence of 4%CubTiO (b) without sonication as a control for 2 h and (c) under sonication for 2 h. (d) Bar chart of the lag phase delay after 40 min of sonication of the sample series. **Figure 17.** Growth Curves of *E. coli* in the presence of (a) bTiO, (b) 1%CubTiO, (c) 2%CubTiO, and (d) 8%CubTiO under sonication for up to 2 h.

Figure 18. Growth curves of *E. coli*: (a) control, and in the presence of (b) 4%bFeTiO, (c) 4%bCoTio, and (d) 4%bMnTiO under sonication for up to 2 h.

Figure 19. EPR spectra of the sample series with DMPO as the spin trap before (dotted curves) and after (solid curves) sonication for 10 min.

LIST OF TABLES

ABSTRACT

A Multi-Catalytic Approach to Reactive Oxygen Species Generation for Direct Water Disinfection

JOHN TRESSEL

Chapter 1 provides background information on the current standards for producing hydrogen peroxide, as well as a foundation for the oxygen reduction reaction as a possible replacement. Then delving into electrocatalytic, piezocatalytic and photocatalytic nanomaterials for reactive oxygen species generation. Finally the effect those species can have on bacteria.

Chapter 2 and **Chapter 3** detail two studies focused on the use of porphyrin based electrocatalysts to generate H_2O_2. In **Chapter 2**, copper chlorophyllin modified via magnetic induction heating was found to selectively produce hydrogen peroxide via the two electron oxygen reduction reaction. **Chapter 3** is an expansion of this, utilizing tetraphenyl porphyrin to examine the effects of changing side chains and metal centers has on material synthesis catalytic activity. Here copper tetraphenyl porphyrin and cobalt tetraphenyl porphyrin were found to produce hydrogen peroxide via the two electron oxygen reduction reaction, but at lower initially heating temperature than copper chlorophyllin.

Chapter 4 explores modified mixed oxidation state titanium suboxide as a photocatalyst. Here the modified oxides were able to efficiently utilize visible light

for reactive oxygen species production which was applied to *E. coli* inhibition and organic dye degradation.

Chapter 5 expands on the modification of titanium oxide via addition of other metal oxide heterostructure additions. This was done to increase piezocatalytic performance, here copper oxide was found to be the most effective addition for piezocatalysis and reactive oxygen species generation and again were applied to *E. coli* inhibition and organic dye degradation.

Chapter 6 summarizes the work completed and its potential impact on reactive oxygen species generation

DEDICATION

To My Family

ACKNOWLEDGEMENTS

Ten years in barely a blink, it feels strange getting ready to leave UCSC for a second time. Unfortunately, I doubt I can find an excuse to come back for a third degree. With that I would like to thank Professor Shaowei Chen for letting some kid who could barely balance a redox reaction have the time to learn. For his patient mentorship when I needed it and him knowing when to guide me forward when I was unsure of what to do on my own. Being able to see the dedication and focus you have to the field of chemistry is inspiring and at times even a little intimidating. Thank you Professor Bud Bridges for being extremely patient with me while I stumble through Linux controls while teaching me about XAS. Thank you Professor Chad Saltikov for his guidance in microbiology and experimental design. Thank you to Dr. Kevin Singewald for assisting me with EPR experiments. Thank you to Brandon Cheney for helping me with SEM measurements. I would like to thank my committee, Ted Holman and Alex Ayzner. Not just for their time while I was a graduate student but also going all the way back to my undergraduate where they made sure I had my foundation to get this far. Also, I ended up TAing 163b every year graduate school so Alex being thorough in teaching really paid off. And Ted introducing me to crystal symmetry back in inorganic which played a very important role my piezocatalytic work. Thank you to all my lab mates, Dr. Forrest Nichols, Dr. Qiming Liu, Dr. Bingzhe Yu, Dr. Davida Dubois, Dingjie Pan, Colton Jones, Tianchen Cui, Xingjian Song, and Josue Pizano, would have gone even crazier if it wasn't for all of you. Thank you to my undergrads Abdelrahman Warshana, Alex Nguyen,

Kevin Nguyen and Angel Hidalgo for all their hard work and dedication. I am grateful for the funding from ARCS and Sigma Xi. Thank you to Lawrence Berkeley National Laboratory and the SLAC National Accelerator Laboratory and their corresponding staff scientists for their support and training. Thank you to Amanda for always keeping me grounded. Thank you to Josie and Ellie for never letting me get too cocky. Thank you to my mom and dad for always being my biggest supporters.

The text of this dissertation includes reprints of the following previously published material:

- John Tressel, Qiming Liu, Davida DuBois, Bingzhe Yu, Abdelrahman Warshana, Frank Bridges, Chad Saltikov, and Shaowei Chen, “Ultrafast Modification of Copper Chlorophyllin by Magnetic Induction Heating for Water Electrodisinfection by Selective Reduction of Oxygen to Hydrogen Peroxide” The Journal of Physical Chemistry C 2025 129 (7), 3931-3941.
- John Tressel, Alex Nguyen, Phat Nguyen, Colton Jones, Tianchen Cui, Abdelrahman Warshana, Kevin Singewald, Glenn Millhauser, Chad Saltikov, Shaowei Chen, “Ultrafast Synthesis of Titanium Suboxide via Magnetic Induction Heating for Enhanced Photodynamic Activity” Chemistry–A European Journal, 2025 p.e03354.

The corresponding author, Dr. Shaowei Chen, listed in each publication, supervised the research which is the basis for this dissertation

Chapter 1 Introduction

1.1 Industrial hydrogen peroxide and the anthraquinone process

Hydrogen peroxide (H_2O_2) is listed as one of the 100 most important chemicals in the world, that has found a wide range of applications, such as chemical manufacturing, wastewater treatment, and textile bleaching.[1-3] Hydrogen peroxide is considered to be one of the most environmentally friendly oxidants because only water is produced as a byproduct of its oxidation.[4] As such hydrogen peroxide is in an ideal position to replace chlorine-based bleaches to exclude halogenated products in waste streams.[5] Currently, large scale H_2O_2 production relies primarily on the industrial anthraquinone process in which hydrogen, atmospheric oxygen, and an anthraquinone derivative are utilized in the reaction cycle. The crude hydrogen peroxide obtained is then purified and concentrated and is usually marketed with an added stabilizer as aqueous solutions regularly with an end product greater than 70 wt%.[6, 7] While this process currently produces about 98% of global hydrogen peroxide demands it is inherently energy-intensive and generates environmentally hazardous byproducts Moreover, the storage and transportation of the concentrated H_2O_2 solutions pose significant personal safety and environmental risks, particularly in the event of a chemical spill.[8, 9]

1.2 Two electron oxygen reduction reaction

One of the most investigated alternatives to the anthraquinone process is the direct synthesis of H_2O_2 from H_2 and O_2 via the two-electron oxygen reduction reaction

(ORR). This allows for the decentralized production of H_2O_2 without the risk of transportation or environmentally hazardous by products.[10] Mechanistically, there is also a competing pathway for ORR the four-electron ORR, which produces water and is already a key half-reaction in various electrochemical systems though focused on energy storage and conversion.[11, 12] Both pathways are hampered by sluggish kinetics, involving multiple proton-coupled electron transfer steps and high activation barriers.[13, 14] Typically $2e^-$ ORR requires an end on binding of O_2 to the catalytic site. Followed by the addition of a proton generating a *OOH intermediate.[15]

$$O_2 + 2H^+ + 2e^- \rightarrow H_2O_2 \quad (1)$$

$$O_2 + * \rightarrow OO* \quad (2)$$

$$OO* + (H^+ + e^-) \rightarrow OOH* \quad (3)$$

$$OOH* + (H^+ + e^-) \rightarrow * + H_2O_2 \quad (4)$$

While the 4e- ORR favors a side on binding helping facilitate the O-O bond cleavage after the formation of the OOH* intermediate.[16]

$$O_2 + 4H^+ + 4e^- \rightarrow H_2O \quad (5)$$

$$O_2 + * \rightarrow OO* \quad (6)$$

$$OO* + (H^+ + e^-) \rightarrow OOH* \quad (7)$$

$$OOH* + (H^+ + e^-) \rightarrow O* + H_2O \quad (8)$$

$$O* + (H^+ + e^-) \rightarrow OH* \quad (9)$$

$$OH^* + (H^+ + e^-) \rightarrow * + H_2O \qquad (10)$$

In short catalysts tailored for the $2e^-$ ORR pathway need to stabilize the O-O bond in OOH*, thereby favoring the direct release of H_2O_2. Strategies to achieve this include modifying the active metal site, it's coordination and support structures.

1.3 Electrocatalytic design

To ensure the selective production of peroxide, the careful design of catalytic active sites must be considered. The key step separating the $2e^-$ ORR vs $4e^-$ ORR is the cleavage of the O-O bond.[17] This is typically achieved by the side on binding of the O_2 by both oxygen atoms at once vs the end on binding of one oxygen that is favored by the $2e^-$ ORR.[18] The type of O_2 binding can be controlled by the available catalytic active sites. Isolated metal atoms found in single atom catalysts allow for the efficient binding of O_2 but do not allow for more than one oxygen at a time, forcing end on binding.[10, 19] While nanoparticles with multiple metal and metal oxide sites in close proximity allow for side on binding of both oxygens at once and the cleavage of the O-O bond.[20] Because of this the efficient production of single atom catalytic sites are vital for the production of $2e^-$ ORR catalysts. Of these sites metal-N_4 have been highlighted for their high activity. Though there are several factors to consider here too, like the identity of the central metal atom which strongly influences the adsorption behavior of oxygen intermediates. Such as FeN_4 which even with limited side on binding often strongly binds O_2 favoring the O–O bond cleavage and thus the $4e^-$ pathway toward water production.[21] Or in contrast, CuN_4 centers which generally

exhibit weaker oxygen adsorption, generally suppressing O-O cleavage and making them highly selective for peroxide formation.[22] The oxidation state can also determine the activity, like for CoN_x sites being able to be highly effective for both the $2e^-$ and $4e^-$ pathways but being modulated via Co^{2+} vs Co^{3+} oxidation and CoN_4 vs CoN_5 coordination.[23, 24] In addition to the metal identity, the local coordination structure surrounding the active site can significantly modify catalytic performance. Nitrogen coordination stabilizes isolated metal atoms within the carbon matrix while simultaneously altering the electronic density of the metal center, here even subtle distortions from the ideal square-planar $M–N_4$ configuration may substantially alter catalytic behavior.[25] Like in CoN_4 vs CoN_5 variations in nitrogen coordination geometry can change the adsorption strength of oxygen intermediates and therefore influencing the balance between $2e^-$ and $4e^-$ ORR pathways. Finally, even the carbon support itself also contributes significantly to catalytic performance. Highly graphitized carbon materials provide excellent electrical conductivity, enabling rapid electron transport to active sites during the reduction reaction and porous structures provide high catalytic surface areas.[26] Whereas overly defective structures can cause a breakdown in the carbon network and a decrease in electrical conductivity.[27]

1.4 Photocatalytic generation of reactive oxygen species

Until now, only the design of electrocatalysts has been discussed. However, an intrinsic short coming of electrocatalysts is the need for an additional energy source to supply the electrical charge. As such mechanisms for water purification that do not require a human made energy source should also be examined. Of these

photocatalysts have received a significant amount of attention due to their ability to produce potent reactive oxygen species that can be utilized to kill bacteria using only natural light as an energy source. This can be done by a photocatalytic material absorbing light with similar energy as the material's bandgap, exciting electrons from the valence band to the conduction band. The excited electron-hole pair is then able to react with nearby species to generate radicals.[28] While in water there is a natural abundance of O_2 and H_2O molecules leading photocatalysts to generate reactive oxygen species. The most commonly studied of these are superoxide, formed when an excited electron is transferred from the conduction band to O_2, and hydroxyl typically generated at the valance band hole by the oxidation of H_2O. While these reactive oxygen species are highly reactive, they consequently have extremely short lifetimes.[29] This requires the catalytic materials to be able to be dispersed directly into the solution in need of disinfection, unlike electrocatalysis where the product can be stored and used later. As such photocatalysts are typically made of semiconductive materials, like TiO_2 that are low cost, and highly biocompatible. However, TiO_2 like many of these materials, can only utilize higher energy UV light compared to visible light which is more abundant in solar light. Because of this semiconductor design to better shrink the photocatalytic band gap and increase visible light utilization has become a focal point of photocatalytic research.

1.5 Piezocatalytic generation of reactive oxygen species

Another method of reactive oxygen species generation is piezocatalysis. Piezoelectric materials can generate surface charges when under mechanical stress,

such vibrations, ultrasound, or even flowing water. These surface charges can then generate reactive oxygen species like superoxide and hydroxyl similarly to photocatalysis.[30, 31] This surface charge occurs due to the displacement of charge centers within noncentrosymmetric crystalline structures while under stress.[32] Typically these materials are characterized by a piezoelectric coefficient (d_{33}) that defines the charge generated by a materials under a controlled force (pC N^{-1}). The most widely studied piezocatalyst have been ceramic materials like BaTiO3 with high d33s due to their natural lack of inversion centers in their crystal structures.[33, 34] While polymer-based materials like PVDF have also been examined. Piezocatalysis can also be utilized more easily than photocatalysis with water sources possessing poor light penetration like turbid water. Overall piezoelectric materials show immense potential in future water purification and bacterial inhibition applications.

1.6 Effects of reactive oxygen species on bacteria

Reactive oxygen species are known to induce oxidative stress that compromises cellular components including DNA, proteins, and cell membranes which readily result in bacterial death.[35] Proteins being prone to oxidation can be easily damaged, leading to misfolding, enzymatic inactivation, and complete protein degradation. Beyond direct protein damage leading to cell death, reactive oxygen species can impact bases in DNA leading to mutations that disrupt replication thus leading to inhibited mitosis. Because of this bacteria have defensive mechanisms to defend against oxidative stress like the production of enzymes like superoxide dismutase and catalase.[36] These work by neutralizing reactive oxygen species by converting them to

water and oxygen molecules.[37] Additionally the cell's structure is its own defense, with most nanomaterials being too large for bacterial uptake the bacterial membrane must be damaged before direct oxidative stress can be applied to the interior proteins.[38, 39] As such over whelming all the bacteria's defenses is necessary for complete bacterial inhibition.

1.7 References

(1) Zhao, E.; Xue, W.; Qin, S.; Guo, Y.; Xin, X.; Wang, H.; Zhang, Y.; Zuo, S. A review of H2O2 electrosynthesis by 2-electron ORR and 2-electron WOR: From catalysts to electrochemical cells. *Coordination Chemistry Reviews* **2025**, *545*, 217042.

(2) Chang, Q.; Zhang, P.; Mostaghimi, A. H. B.; Zhao, X.; Denny, S. R.; Lee, J. H.; Gao, H.; Zhang, Y.; Xin, H. L.; Siahrostami, S. Promoting H2O2 production via 2-electron oxygen reduction by coordinating partially oxidized Pd with defect carbon. *Nature communications* **2020**, *11* (1), 2178.

(3) Hu, Y.; Zhang, J.; Shen, T.; Li, Z.; Chen, K.; Lu, Y.; Zhang, J.; Wang, D. Efficient electrochemical production of H2O2 on hollow N-doped carbon nanospheres with abundant micropores. *ACS Applied Materials & Interfaces* **2021**, *13* (25), 29551-29557.

(4) Nishimi, T.; Kamachi, T.; Kato, K.; Kato, T.; Yoshizawa, K. Mechanistic study on the production of hydrogen peroxide in the anthraquinone process. Wiley Online Library: 2011.

(5) Ingle, A. A.; Ansari, S. Z.; Shende, D. Z.; Wasewar, K. L.; Pandit, A. B. Progress and prospective of heterogeneous catalysts for H2O2 production via anthraquinone process. *Environmental Science and Pollution Research* **2022**, *29* (57), 86468-86484.

(6) Tang, J.; Zhao, T.; Solanki, D.; Miao, X.; Zhou, W.; Hu, S. Selective hydrogen peroxide conversion tailored by surface, interface, and device engineering. *Joule* **2021**, *5* (6), 1432-1461.

(7) Campos-Martin, J. M.; Blanco-Brieva, G.; Fierro, J. L. G. Hydrogen peroxide synthesis: an outlook beyond the anthraquinone process. *Angewandte Chemie International Edition* **2006**, *45* (42), 6962-6984.

(8) Wen, Y.; Zhang, T.; Wang, J.; Pan, Z.; Wang, T.; Yamashita, H.; Qian, X.; Zhao, Y. Electrochemical reactors for continuous decentralized H2O2 production. *Angewandte Chemie* **2022**, *134* (35), e202205972.

(9) Perry, S. C.; Mavrikis, S.; Wang, L.; de León, C. P. Future perspectives for the advancement of electrochemical hydrogen peroxide production. *Current Opinion in Electrochemistry* **2021**, *30*, 100792.

(10) Song, M.; Liu, W.; Zhang, J.; Zhang, C.; Huang, X.; Wang, D. Single-atom catalysts for H2O2 electrosynthesis via two-electron oxygen reduction reaction. *Advanced Functional Materials* **2023**, *33* (15), 2212087.

(11) Vo, T. G.; Gao, J.; Liu, Y. Recent development and future frontiers of oxygen reduction reaction in neutral media and seawater. *Advanced Functional Materials* **2024**, *34* (23), 2314282.

(12) Yang, Q.; Xiao, Z.; Kong, D.; Zhang, T.; Duan, X.; Zhou, S.; Niu, Y.; Shen, Y.; Sun, H.; Wang, S. New insight to the role of edges and heteroatoms in nanocarbons for oxygen reduction reaction. *Nano Energy* **2019**, *66*, 104096.

(13) Anwar, M. F.; Yu, Y.; Rasool, S.; Akbar, N.; Huang, J.; Singh, M.; Gupta, P.; Wan, S.; Huang, Q.-A.; Yang, F. Insights into the proton-coupled electron transfer mechanism in fuel cells. *ACS Applied Materials & Interfaces* **2025**, *17* (12), 18371-18382.

(14) Di Noto, V.; Negro, E.; Patil, B.; Lorandi, F.; Boudjelida, S.; Bang, Y. H.; Vezzu, K.; Pagot, G.; Crociani, L.; Nale, A. Hierarchical metal–[carbon nitride shell/carbon core] electrocatalysts: A promising new general approach to tackle the ORR bottleneck in low-temperature fuel cells. *ACS catalysis* **2022**, *12* (19), 12291-12301.

(15) Lai, F.; Shang, H.; Jiao, Y.; Chen, X.; Zhang, T.; Liu, X. Recent progress and perspective on electrocatalysis in neutral media: Mechanisms, materials, and advanced characterizations. *Interdisciplinary Materials* **2024**, *3* (4), 492-529.

(16) Kulkarni, A.; Siahrostami, S.; Patel, A.; Nørskov, J. K. Understanding catalytic activity trends in the oxygen reduction reaction. *Chemical reviews* **2018**, *118* (5), 2302-2312.

(17) Zhang, Y.; Chen, X.; Zhang, H.; Ge, X. Screening of catalytic oxygen reduction reaction activity of 2, 9-dihalo-1, 10-phenanthroline metal complexes: The role of transition metals and halogen substitution. *Journal of Colloid and Interface Science* **2022**, *609*, 130-138.

(18) Wu, M.; Zhan, X.; Yang, S.; Zheng, J.; Cui, X.; Xia, B. Y.; Sun, S.; Yang, Y. The 2e-vs. 4e-Pathways for ORR in Rechargeable Zinc-Air Batteries. *Energy & Environmental Science* **2026**.

(19) Liu, K.; Fu, J.; Lin, Y.; Luo, T.; Ni, G.; Li, H.; Lin, Z.; Liu, M. Insights into the activity of single-atom Fe-NC catalysts for oxygen reduction reaction. *Nature Communications* **2022**, *13* (1), 2075.

(20) Ye, C.; Zhou, Y.; Li, H.; Shen, Y. Single-iron, cobalt, nickel, and copper-atom catalysts for the selective reduction of oxygen to H 2 O 2. *Green Chemistry* **2023**, *25* (10), 3931-3939.

(21) Li, S.; Shi, L.; Guo, Y.; Wang, J.; Liu, D.; Zhao, S. Selective oxygen reduction reaction: mechanism understanding, catalyst design and practical application. *Chemical science* **2024**, *15* (29), 11188-11228.

(22) Sun, Y.; Silvioli, L.; Sahraie, N. R.; Ju, W.; Li, J.; Zitolo, A.; Li, S.; Bagger, A.; Arnarson, L.; Wang, X. Activity–selectivity trends in the electrochemical production of hydrogen peroxide over single-site metal–nitrogen–carbon catalysts. *Journal of the American Chemical Society* **2019**, *141* (31), 12372-12381.

(23) Yang, B.; Li, X.; Cheng, Q.; Jia, X.; Liu, Y.; Xiang, Z. A highly efficient axial coordinated CoN5 electrocatalyst via pyrolysis-free strategy for alkaline polymer electrolyte fuel cells. *Nano Energy* **2022**, *101*, 107565.

(24) Wang, W.; Hu, Y.; Li, P.; Liu, Y.; Chen, S. Realizing the 4e–/2e–pathway transition of O2 reduction on Co–N4–C catalysts by regulating the chemical structures beyond the second coordination shells. *ACS Catalysis* **2024**, *14* (8), 5961-5971.

(25) Tong, Y.; Wang, L.; Hou, F.; Dou, S. X.; Liang, J. Electrocatalytic oxygen reduction to produce hydrogen peroxide: rational design from single-atom catalysts to devices. *Electrochemical energy reviews* **2022**, *5* (3), 7.

(26) Wang, H.; Jerigova, M.; Hou, J.; Tarakina, N. V.; Delacroix, S.; López-Salas, N.; Strauss, V. Modulating between 2e− and 4e− pathways in the oxygen reduction reaction with laser-synthesized iron oxide-grafted nitrogen-doped carbon. *Journal of Materials Chemistry A* **2022**, *10* (45), 24156-24166.

(27) Muñoz-Morales, M.; Ramírez, A.; Cañizares, A.; Llanos, J.; Ania, C. Evaluating key properties of carbon materials as cathodes for the electrogeneration of hydrogen peroxide. *Carbon* **2023**, *210*, 118082.

(28) He, W.; Jia, H.; Yang, D.; Xiao, P.; Fan, X.; Zheng, Z.; Kim, H.-K.; Wamer, W. G.; Yin, J.-J. Composition directed generation of reactive oxygen species in irradiated mixed metal sulfides correlated with their photocatalytic activities. *ACS Applied Materials & Interfaces* **2015**, *7* (30), 16440-16449.

(29) Tain, R. W.; Scotti, A. M.; Li, W.; Zhou, X. J.; Cai, K. Imaging short-lived reactive oxygen species (ROS) with endogenous contrast MRI. *Journal of Magnetic Resonance Imaging* **2018**, *47* (1), 222-229.

(30) Roy, S.; Wang, S.; Ullah, Z.; Hao, H.; Xu, R.; Roy, J.; Gong, T.; Hasan, I.; Jiang, W.; Li, M.; et al. Defect-Engineered Biomimetic Piezoelectric Nanocomposites With Enhanced ROS Production, Macrophage Re-polarization, and Ca2+ Channel Activation for Therapy of MRSA-Infected Wounds and Osteomyelitis. *Small* **2025**, *21* (10), 2411906. DOI: https://doi.org/10.1002/smll.202411906.

(31) Ren, Z.; Chen, F.; Zhao, Q.; Zhao, G.; Li, H.; Sun, W.; Huang, H.; Ma, T. Efficient CO2 reduction to reveal the piezocatalytic mechanism: From displacement current to active sites. *Applied Catalysis B: Environmental* **2023**, *320*, 122007.

(32) Zhao, L.; Xu, M.; Yang, S.; Zhu, Z.; Qi, J.; Meng, F. Production of hydrogen peroxide by piezocatalytic processes: mechanisms, recent advances, and prospects. *ACS Sustainable Chemistry & Engineering* **2025**, *13* (24), 8853-8869.

(33) Sun, Y.; Shen, S.; Deng, W.; Tian, G.; Xiong, D.; Zhang, H.; Yang, T.; Wang, S.; Chen, J.; Yang, W. Suppressing piezoelectric screening effect at atomic scale for enhanced piezoelectricity. *Nano Energy* **2023**, *105*, 108024.

(34) Lei, J.; Wang, C.; Feng, X.; Ma, L.; Liu, X.; Luo, Y.; Tan, L.; Wu, S.; Yang, C. Sulfur-regulated defect engineering for enhanced ultrasonic piezocatalytic therapy of bacteria-infected bone defects. *Chemical Engineering Journal* **2022**, *435*, 134624. DOI: https://doi.org/10.1016/j.cej.2022.134624.

(35) Li, Y.; Zhang, W.; Niu, J.; Chen, Y. Mechanism of photogenerated reactive oxygen species and correlation with the antibacterial properties of engineered metal-oxide nanoparticles. *ACS nano* **2012**, *6* (6), 5164-5173.

(36) Halawa, E. M.; Fadel, M.; Al-Rabia, M. W.; Behairy, A.; Nouh, N. A.; Abdo, M.; Olga, R.; Fericean, L.; Atwa, A. M.; El-Nablaway, M. Antibiotic action and resistance: updated review of mechanisms, spread, influencing factors, and alternative approaches for combating resistance. *Frontiers in Pharmacology* **2024**, *14*, 1305294.

(37) Dwyer, D. J.; Kohanski, M. A.; Collins, J. J. Role of reactive oxygen species in antibiotic action and resistance. *Current opinion in microbiology* **2009**, *12* (5), 482-489.

(38) Vaishampayan, A.; Grohmann, E. Antimicrobials functioning through ROS-mediated mechanisms: current insights. *Microorganisms* **2021**, *10* (1), 61.

(39) Thangudu, S.; Su, C.-H. Review of light activated antibacterial nanomaterials in the second biological window. *Journal of Nanobiotechnology* **2025**, *23* (1), 293.

Chapter 2 Ultrafast Modification of Copper Chlorophyllin by Magnetic Induction Heating for Water Electrodisinfection by Selective Reduction of Oxygen to Hydrogen Peroxide

Reproduced with permission form (John Tressel, Qiming Liu, Davida DuBois, Bingzhe Yu, Abdelrahman Warshana, Frank Bridges, Chad Saltikov, and Shaowei Chen, “Ultrafast Modification of Copper Chlorophyllin by Magnetic Induction Heating for Water Electrodisinfection by Selective Reduction of Oxygen to Hydrogen Peroxide” The Journal of Physical Chemistry C 2025 129 (7), 3931-3941.)

2.1 Abstract

The two-electron oxygen reduction reaction has emerged as an effective strategy to replace the anthraquinone process for the on-site green production of hydrogen peroxide that can be used for electrochemical disinfection of water. Herein, sodium copper chlorophyllin is modified by magnetic induction heating at controlled currents (300 to 500 A) for seconds to produce CuNC nanocomposites, where the CuN_4 coordination moieties are retained and embedded within a carbon scaffold, as manifested in transmission electron microscopy, X-ray absorption spectroscopy, X-ray photoelectron spectroscopy, and Raman measurements. In electrochemical tests the CuNC nanocomposites exhibit an apparent electrocatalytic activity towards the selective two-electron oxygen reduction to hydrogen peroxide in alkaline media, and the sample prepared at 400 A for 10 s stands out as the best among the series, with a H_2O_2 yield close to 90%. Such a unique property can be exploited for on-site water treatment/disinfection, as manifested in the effective degradation of organic dye pollutants (e.g., methylene blue) and removal of waterborne pathogens (e.g., Escherichia coli). Results from this study highlight the unique potential of magnetic induction heating in the ultrafast production of functional nanocomposites as high-performance electrocatalysts for diverse applications.

2.2 Introduction

Hydrogen peroxide (H_2O_2) is a commodity chemical that has found a wide range of applications, such as chemical production, water disinfection, and wastewater

treatment.[1-4] Currently H_2O_2 is produced primarily through the industrial anthraquinone process that is energy-intensive and may impact the environment with toxic byproducts.[5] In addition, there is a high risk to the environment of chemical spills due to storage and transportation requirements of concentrated H_2O_2 commonly above 70% by weight.[6] Yet, as most applications require only a low concentration of H_2O_2, such as 8% for water treatment, and 30% for most chemical synthesis, on-site production of H_2O_2 has attracted extensive interest, and one of the most prominent technologies is the electrochemical two-electron oxygen reduction reaction ($2e^-$ ORR) due to its possibility of decentralized green production of H_2O_2.[6-8] The major challenge in this electrochemical approach is the selectivity of the $2e^-$ pathway ($O_2 + 2H^+ + 2e^- \rightarrow H_2O_2$) over the $4e^-$ one ($O_2 + 4H^+ + 4e^- \rightarrow H_2O$).[9, 10] Mechanistically, the $2e^-$ pathway can be facilitated by end-on binding of the O2 molecules onto the catalytic active centers leading to the formation of the *OOH intermediate, while the $4e^-$ pathway favors side-on binding which causes a stretching of the O-O bond and leads to its breakage.[11, 12] Therefore, it calls for rational design of the electronic structure of the catalysts to achieve selective $2e^-$ ORR.

Precious metal-based nanoparticles have been the leading catalysts towards selective $2e^-$ ORR. For instance, PtHg alloy nanoparticles have been the benchmark catalyst which possess a selectivity over 95% at the overpotential (η) of -70 mV towards $2e^-$ ORR for H_2O_2 production in alkaline media.[13, 14] PdAu alloy nanoparticles also show a high activity in acidic media over 90% selectivity at the overpotential of -100 mV.[15] Yet the high cost and limited natural abundance of precious metals hinder their

widespread applications. Thus recently extensive research has been devoted to the rational design and engineering of carbon-based nanocomposites with earth-abundant transition metals, such as Co, Cu, and Ni, that have been known to be effective ORR catalysts.[16-19] For example, Yu et al.[7] prepared Cu/C nanocomposites by controlled pyrolysis of a Cu-containing metal-organic framework (MOF) precursor, and observed that the selective electrocatalytic activity towards $2e^-$ ORR was enhanced from 45% to 68% at +0.1 V, due to electrochemical activation that facilitated the enrichment of Cu2O species in the sample. Additionally, single atom catalysts (SACs) have shown significant promise, where the high selectivity for $2e^-$ ORR is facilitated by the spatial separation of the active sites (thus end-on adsorption of intermediates is favored), and metal, nitrogen-codoped carbon (M-N-C) nanocomposites represent a unique option.[2, 20, 21] For instance, Co-N-C nanocomposites have been shown to be 80% selective towards H_2O_2 production at the overpotential of -100 mV.[22] Cu-N-C have also garnered significant interest, where the CuN_x coordination configuration can be engineered for optimal binding of reaction intermediates.[23-25],[26] For instance, Wang et al.[27] prepared carbon composites with CuN_x moieties via direct pyrolysis of a Cu-containing MOF and observed a selectivity up to 65% in the production of H_2O_2 from $2e^-$ ORR.

These M-N-C nanocomposites are traditionally prepared by controlled pyrolysis which is time and energy intensive. Recently, magnetic induction heating (MIH) has emerged as an ultrafast synthesis technique that utilizes the instant generation of an Eddy current when a conductor is immersed into a strong AC magnetic field to heat a

metal surface reaching a temperature over 1000 °C within seconds.[28, 29] Such Joule heating can be readily controlled by the induction current and heating time.[30-32] This has indeed been demonstrated in several recent studies in the preparation of a wide range of functional nanocomposites that exhibited unprecedented electrocatalytic activity towards hydrogen evolution reaction (HER) and oxygen evolution reaction (OER), e.g., FeNi spinels with a good mixing of the Fe and Ni phases,[33] defective carbon-encapsulated Co nanoparticle composites,[30] Ru nanoparticles with RuClx residues,[34] Ru/C nanocomposites,[35, 36] and amorphous MoSx composites.[37] This was largely ascribed to the rapid heating that resulted in the formation of nonequilibrium structures and/or incomplete thermal decomposition of the precursors.

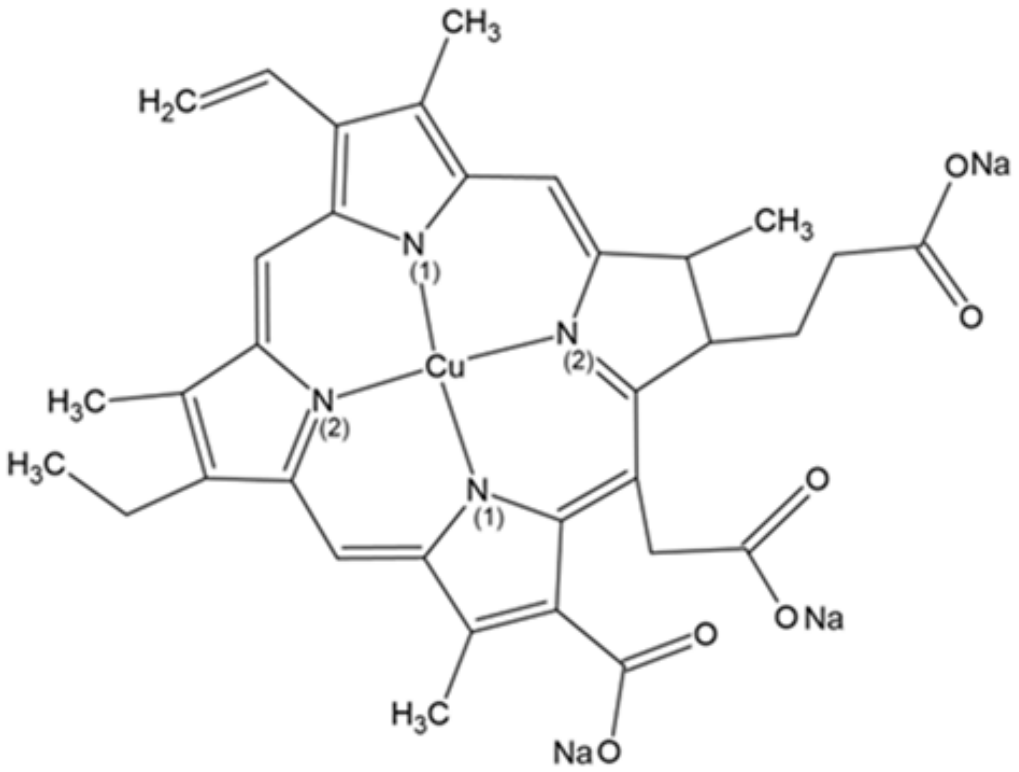

Figure 1. Skeletal structural model of copper chlorophyllin. Note that there are two types of pyrrolic N that bind to the Cu center: N(1) the pyrrolic N and N(2) the aza N.

Herein, copper chlorophyllin (CuCh, Image 1), a porphyrin derivative with a Cu^{2+} center chelated to four pyrrolic N (CuN_4), was treated with MIH at controlled induction currents for a short period of time (up to 12 s). The obtained Cu-N-C nanocomposites exhibited an excellent performance towards the selective $2e^-$ ORR to H_2O_2 in alkaline media. This was due to the rapid heating that facilitated the retention of the CuN_4 moiety of CuCh which is known to be catalytically active towards $2e^-$ ORR.[23-26] Electrochemical measurements showed that the sample prepared at 400 A for 10 s stood out as the best among the series and possessed a selectivity close to 90% of H_2O_2 yield, a unique activity that could be exploited for the on-site effective degradation of organic dye pollutants (e.g., methylene blue) and electrochemical disinfection of water by eradicating waterborne pathogenic bacteria like Escherichia coli (E. coli).

2.3. Results and Discussion

2.3.1 Structural characterizations

The sample structures were first characterized by TEM measurements. From the TEM images of CuNC-400 in **Figure 2a-c**, one can see that the sample possessed a mostly amorphous structure with short-range lattice fringes, where the interplanar spacing of ca. 0.33 nm is consistent with the (002) planes of graphitic carbon,[38] suggesting effective production of a carbon scaffold from the CuCh precursor.

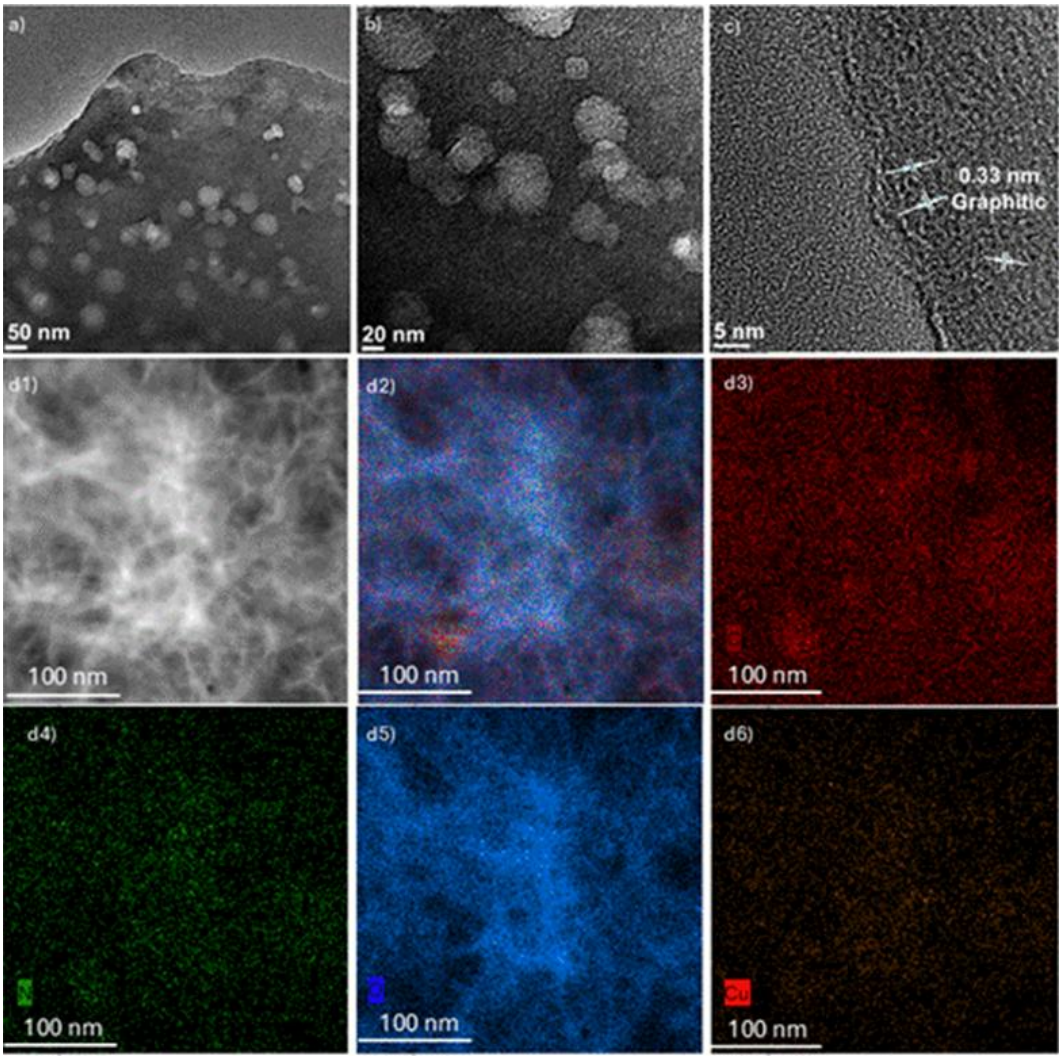

Figure 2. Bright-field TEM images of CuNC-400 at different magnifications. Scale bars are (a) 50 nm, (b) 20 nm and (c) 5 nm. (d1) SEM image, and EDS maps of (d2) all elements, (d3) C, (d4) N, (d5) O, and (d6) Cu. Scale bars are all 100 nm.

In addition, a number of cavities (20 to 60 nm) can be found to be embedded within the carbon matrix, likely a result of acid leaching that removed metal (oxide) nanoparticles (**Figure 3**).

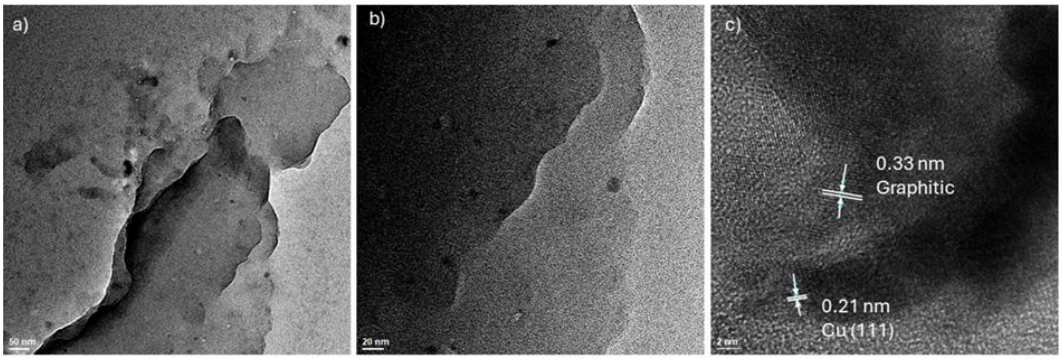

Figure 3. Bright-field TEM images of CuNC-400-10 before acid leaching with HNO_3.

In elemental mapping analysis based on energy-dispersive X-ray spectroscopy (EDS) measurements (**Figure 2d1-d6**), the elements of C, N, O, and Cu can be clearly seen to be homogeneously distributed throughout the sample, and the absence of particulate materials suggests atomic dispersion of the Cu centers within the carbon matrix. Further insights were gathered from XPS measurements. From the survey spectra (**Figure 4**), the Cu 2p, O 1s, N 1s, and C 1s electrons can be readily resolved at ca. 932, 530, 400, and 284 eV, respectively.

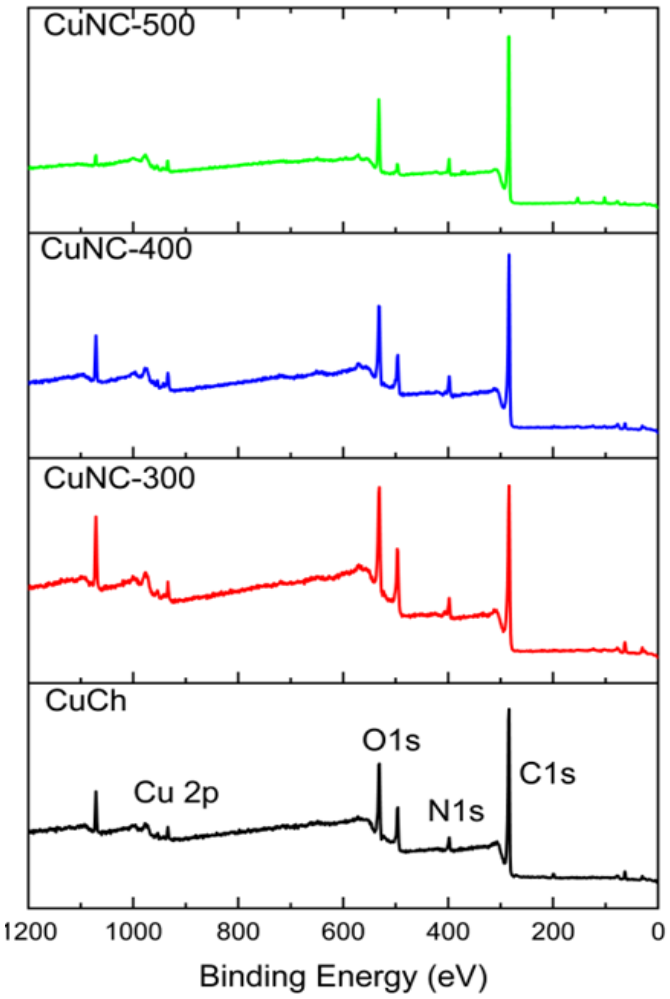

Figure 4. XPS Survey spectra of the sample series.

From the integrated peak areas, the elemental contents can be estimated and compared. From **Table 1**, one can see that CuNC-400 consisted of 74.98 at% C, 5.40 at% N, 15.27 at% O, and 1.49 at% Cu. For CuNC-300, the C, N and Cu contents were slightly lower (70.46 at%, 4.79 at% and 1.35 at%) but the O content was somewhat higher (19.62 at%). CuNC-500 exhibited an opposite trend (78.83 at% C, 4.13 at% N, 15.23 at% O, and 1.22 at% Cu).

Table 1. Elemental contents (at%) of the sample series from XPS measurements

Peak		CuCh	CuNC-300	CuNC-400	CuNC-500
C 1s	C=C	38.44	38.38	37.79	17.44
	C-C	18.95	15.96	15.24	27.06
	C-N/O	12.10	8.72	9.76	28.38
	C=N/O	10.18	10.17	14.34	6.43
	Total C	79.67	73.23	77.13	79.31
N 1s	N(1)	2.33	2.34	2.73	1.63
	N(2)	1.43	2.64	3.01	2.52
	Total N	3.81	4.98	5.74	4.15
O 1s	C=O	4.92	7.14	5.87	10.50
	C-O	10.63	13.25	9.70	4.82
	Total O	15.55	20.39	15.57	15.32
Cu		1.03	1.40	1.56	1.21

These results suggest enhanced graphitization of the CuCh precursor with increasing MIH temperature.

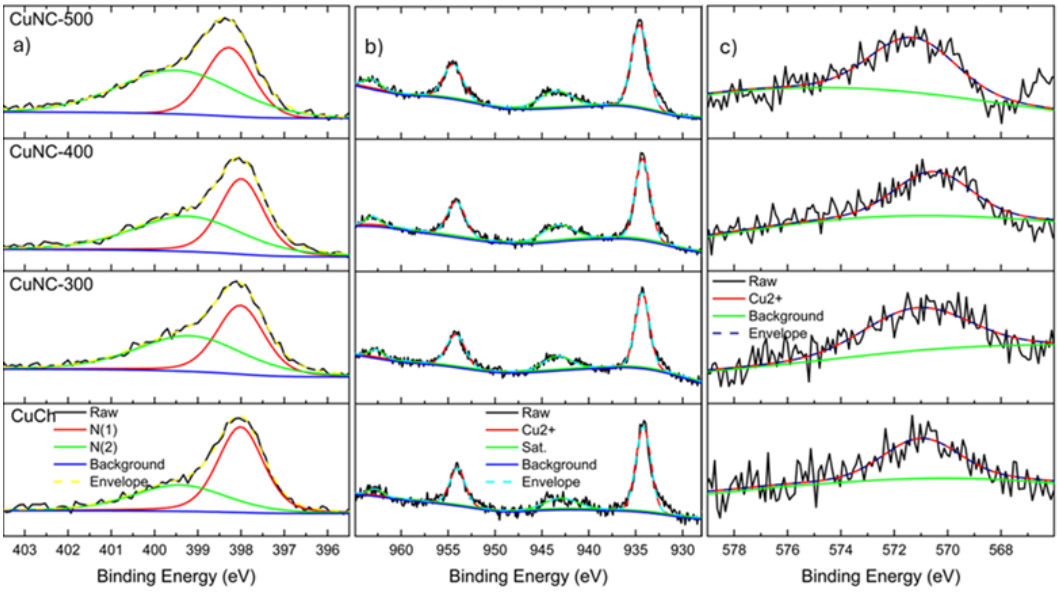

Figure 5. High-resolution XPS scans of the (a) N 1s, (b) Cu 2p and (c) Cu LMM electrons of CuCh and the CuNC samples. Black curves are experimental data and colored curves are deconvolution fits.

The high-resolution scans of the N 1s electrons are shown in **Figure 5a** where the CuCh precursor can be seen to consist of a major peak at 398.0 eV and a minor one at 399.4 eV that can be assigned to the two types of pyrrolic N that bind to the Cu centers, N(1) the sp2 N and N(2) the sp3 N (Scheme 1),[39, 40] respectively. Notably, upon MIH treatment, these two peaks were retained with the CuNC samples, although the fraction of N(1) diminished from ca. 62% for CuCh to 47% for CuNC-300, 48% for CuNC-400, and 40% for CuNC-500 (**Table 1**). In addition, whereas the binding energy of the N(2) remained virtually invariant, the N(1) peak can be seen to shift to a higher energy with increasing MIH temperature, 398.0 eV for CuNC-300, 398.1 eV for CuNC-400, and 398.3 eV for CuNC-500 (**Table 2**). These observations are likely

due to increasing thermal decomposition of the peripheral hydrocarbon segments of CuCh that wrinkled the original planar CuN_4 moiety (Scheme 1).

Table 2. Binding energies (eV) of all elemental components by deconvolution of the XPS data

Peak		**CuCh**	**CuNC-300**	**CuNC-400**	**CuNC-500**
C 1s	C=C	284.2	284.1	284.1	284.2
	C-C	284.8	284.8	284.8	284.8
	C-N/O	285.8	286.0	285.6	285.3
	C=N/O	287.9	288.0	287.7	288.5
N 1s	N(1)	398.0	398.0	398.1	398.3
	N(2)	399.4	399.2	399.2	399.5
O 1s	C=O	530.8	531.0	530.9	531.5
	C-O	532.0	532.4	532.4	532.4
Cu 2p	LMM	570.9	571.2	570.5	571.3
	$2p_{3/2}$	934.2	934.3	934.3	934.6
	Satillite	943.0	943.3	943.2	943.4
	$2p_{1/2}$	954.0	954.2	954.2	954.5
	Satillite	962.8	962.6	963.1	963.1

Figure 5b shows the corresponding Cu 2p spectra. The CuCh precursor can be seen to possess a doublet at 934.2/954.0 eV due to the 2p3/2/2p1/2 electrons of Cu^{2+}, with the corresponding Cu^{2+} satellites at ca. 943.0 and 962.8 eV, [41, 42]and no Cu^0 or Cu^+ peaks at ca. 932/952 eV can be resolved.[7] Notably, after MIH treatment, the Cu 2p binding energies exhibited a clear blue-shift with increasing heating current (temperature), which coincided with the increase of the N 1s binding energy observed above, suggesting increasingly electron-deficient Cu centers within the nanocomposites. Consistent results were obtained from the Cu LMM spectra (**Figure 5c**). The CuCh precursor and CuNC samples can be seen to possess a single component at 570.9 eV arising from Cu^{2+}, again with no clear Cu^0 or Cu^+ peaks at ca. 574.4 or 569.3 eV.[43] The lack of metallic Cu^0 or Cu^+ peaks and the even distribution of Cu species seen in the EDS-based elemental mapping analysis (**Figure 1d**) signifies atomic dispersion of the Cu centers within the carbon matrix, mostly due to the rapid heating that facilitated the retention of the CuN_4 coordination moieties.

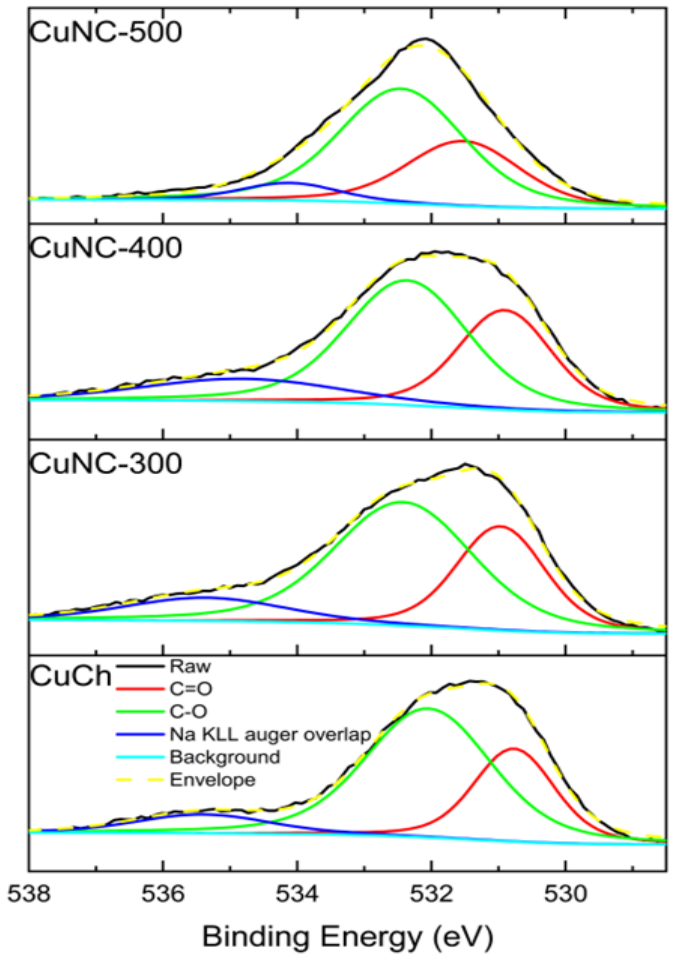

Figure 6. XPS O 1s Spectra of the sample series.

Note that in the O 1s spectra (**Figure 6**) no metal oxide peak can be resolved below 530 eV, confirming the absence of copper oxide in the samples after acid leaching.[44] Significantly, based on the integrated peak areas (**Table 1**), the atomic ratio of N:Cu can be estimated to be ca. 3.70 for CuCh, which decreased only slightly to 3.55 for CuNC-300, 3.62 for CuNC-400, and 3.44 for CuNC-500. This indicates that the CuN_4 moiety of copper chlorophyllin was not significantly damaged during the rapid MIH

treatment, and the retention was the best with CuNC-400, a critical tribute to the ORR activity.

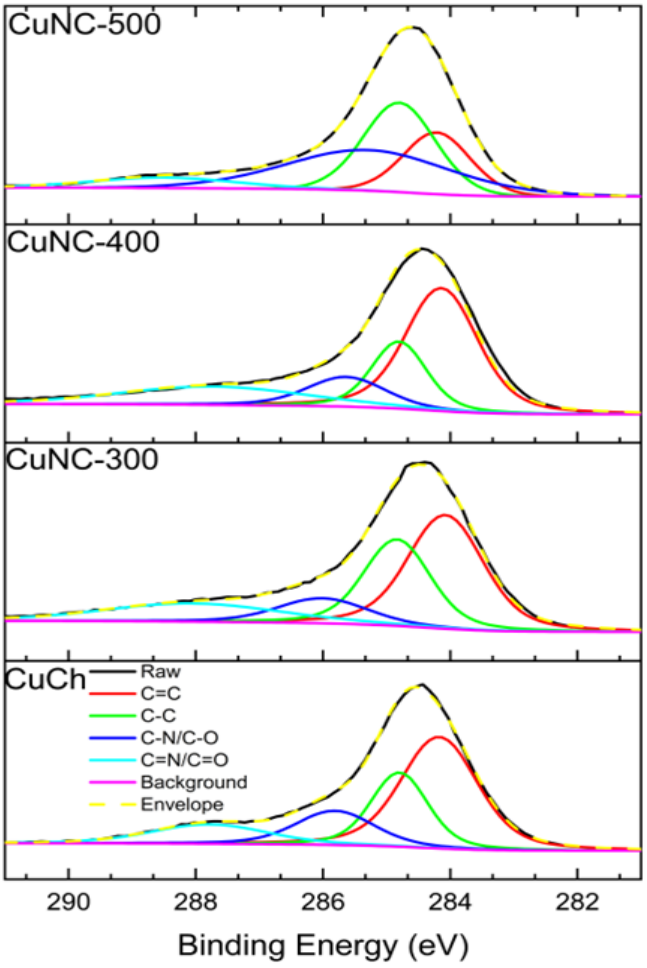

Figure 7. XPS C 1s Spectra of the sample series

The C 1s spectra are shown in **Figure 7**, where three species can be resolved for all samples, 284.2 eV for sp2 C, 288.3 eV for C=O, and 285.5 eV for C-O.[45] Of these, CuNC-400 can be seen to possess the highest content of sp2 C (**Table 1**), suggestive of the optimal conditions for the production of a graphitic carbon scaffold from the CuCh precursor.

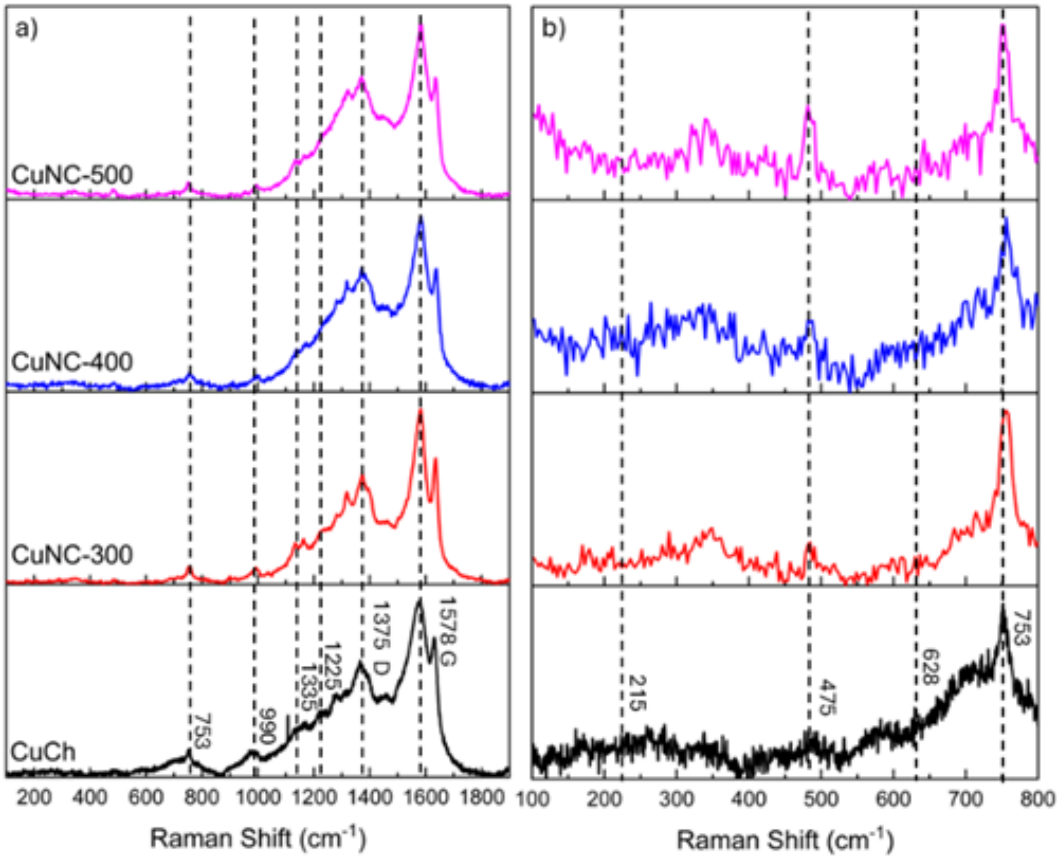

Figure 8. (a) Raman spectra of the CuCh and CuNC samples, and (b) zoom in of the 100 to 800 cm^{-1} range.

Further structural insights were obtained from Raman measurements. From **Figure 8a**, the CuCh precursor can be seen to exhibit a series of fingerprint vibrations, δ(CaCbEt) at 753 cm^{-1}, δ(CbEt) and δ(CaNCa) at 990 cm^{-1}, δ(CbEt) and δ(CaN) at 1135 cm^{-1}, and δ(CaH) and δ(CmH) at 1225 cm^{-1}.[46, 47] Notably, all remained visible in the CuNC samples except that the peak intensity diminished with increasing MIH temperature (in particular the 1225 cm^{-1} vibrations). This suggests that the C-N-C cornerstone of the porphyrin ring survived the MIH treatment, but the outer carbon

fragments were degraded markedly, consistent with results from the \above XPS measurements. Indeed, the CuNC samples can be seen to exhibit the D and G bands of graphitic carbon at 1371 and 1582 cm^{-1}, respectively, and the ratio of the band intensity (ID/IG) can be seen to increase somewhat from 0.77 for CuNC-300 to 0.89 for CuNC-400 and 0.99 for CuNC-500, suggestive of the formation of a slightly increasingly defective carbon scaffold.[48] Notably, the Cu-N bending vibrations remained visible at 215, 475 and 628 cm^{-1} for the CuCh precursor and the CuNC samples (**Figure 8b**).[49-55] This was in good alignment with the retention of the CuN_4 moiety after MIH treatment.

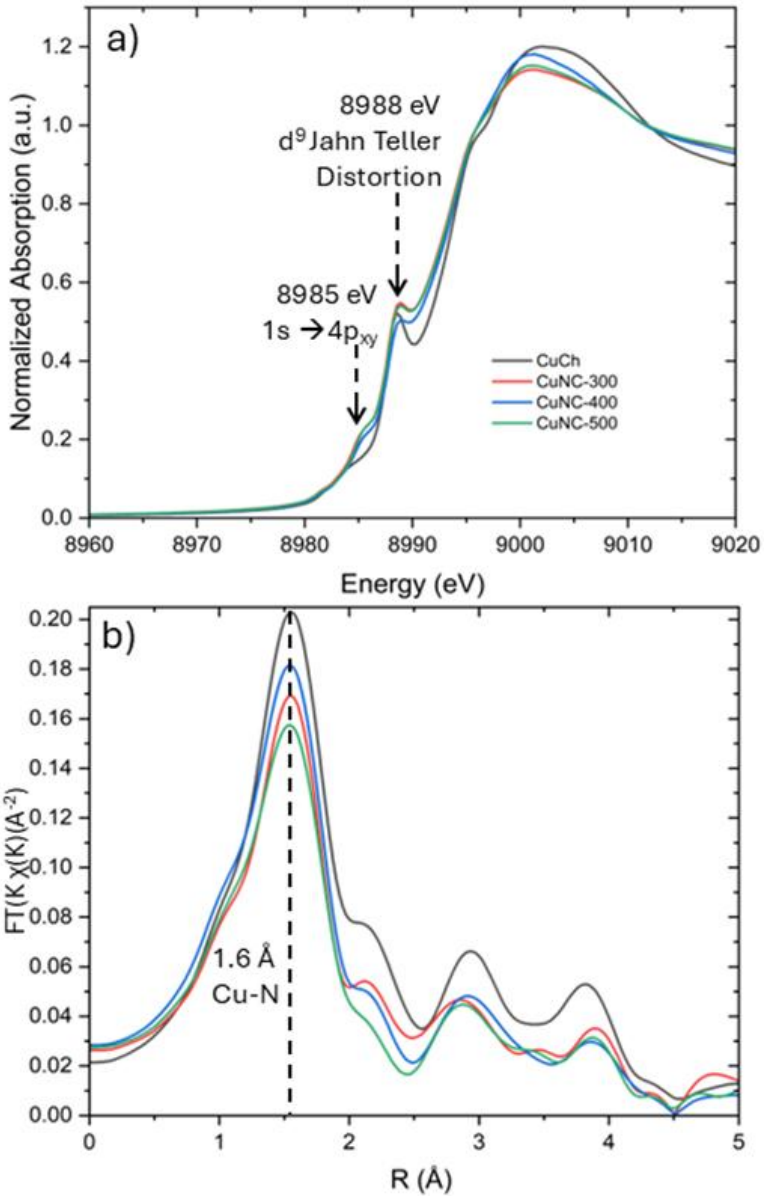

Figure 9. (a) X-ray absorption near-edge spectra (XANES) of Cu K, (b) the corresponding Fourier transformed extended X-ray absorption spectra (FT-EXAFS) of the CuCh and CuNC samples

Further structural insights were obtained from XAS measurements, with the CuCh precursor as a reference. From the Cu K-edge X-ray absorption near edge structure

(XANES) profiles in **Figure 9a**, the CuCh precursor can be seen to possess two peaks at ca. 8985 and 8988 eV that are the typical Cu^{2+} pre-edge shoulders. The former is produced by the 1s → $4p_{xy}$ electron transition of the square-planar CuN_4 moiety,[56-58] whereas the latter is due to Jahn Teller distortion of Cu^{2+}[59, 60] These pre-edge features remained prominent with the CuNC samples, consistent with the retention of the CuN_4 moiety by rapid MIH heating. Yet, one can see that the 1s → $4p_{xy}$ transition peak increased in intensity, whereas the Jahn Teller distortion peak diminished in intensity, suggestive of a decrease of the z axial coordination in CuNC as compared to that in CuCh.[56-60] That is, the Cu atomic configuration was distorted somewhat after MIH heating. Notably, the Cu^{+} peak that is typically seen at 8982 eV for Cu^{+} chelated to nitrogen ligands is absent in all samples, consistent with results from the above XPS measurements (**Figure 5**).[61, 62]

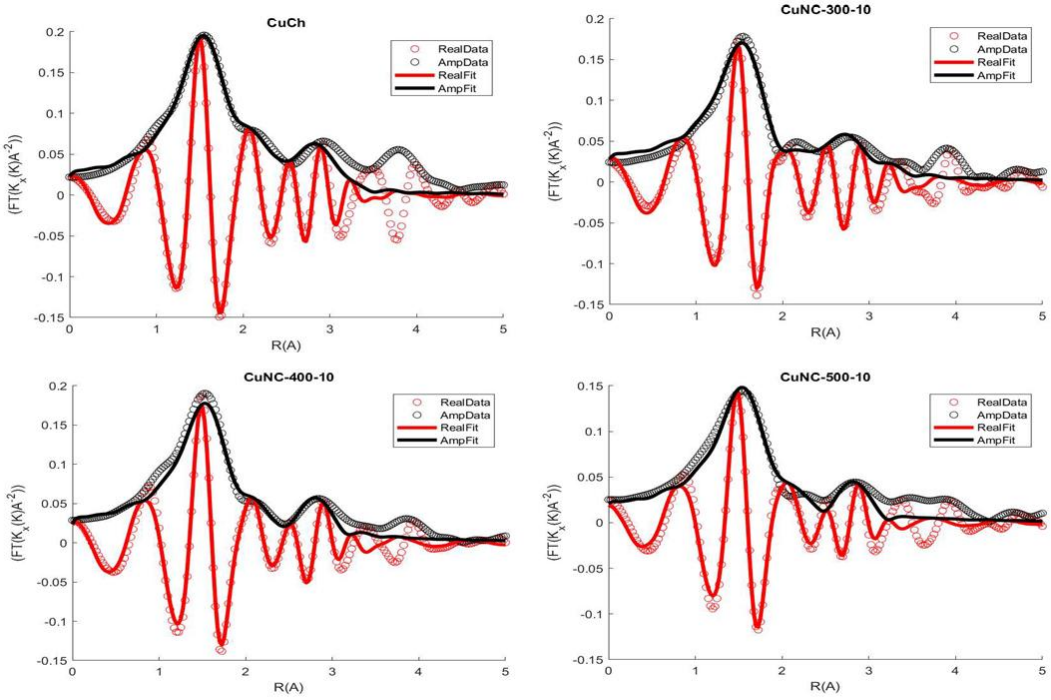

Figure 10. Fitting results of the Cu K-edge EXAFS of the sample series.

The corresponding Fourier-transformed extended X-ray absorption fine structures (FT-EXAFS) are shown in **Figure 9b**. All CuNC samples can be seen to exhibit a profile that is very consistent with that of CuCh, with a dominant peak at ca. 1.6 Å for the Cu-N path.[61, 63] Furthermore, fitting of this peak (**Figure 10**) yields a coordination number (CN) of ca. 4 and an effective pair distance of ca. 1.95 Å for both the CuCh precursor and CuNC samples (**Table 3**), suggesting a bond length of 1.95 Å for the primary Cu-N bond.[62] This further confirms that the CuN_4 structure was retained during MIH treatment thanks largely to the rapid heating.

Table 3. Fitting results of the Cu K edge XAS spectra of the samples series

Samples	**Peak**	**Effective Pair Distance (Å)**	**σ^2**	**CN**
CuCh	Cu-N	1.955	0.038	4.001
	Cu-C 2nd shell	2.456	0.010	8.003
	Cu-Cu	2.587	0.019	0.786
	Multi scattering	2.550	0.002	1.000
	Multi scattering	3.253	0.003	6.334
CuNC-300	Cu-N	1.955	0.004	3.999
	Cu-C 2nd shell	2.419	0.011	8.274

	Cu-Cu	2.574	0.023	0.760
	Multi scattering	2.798	0.004	1.001
	Multi scattering	3.267	0.020	4.411
CuNC-400	Cu-N	1.954	0.004	4.000
	Cu-C 2nd shell	2.470	0.008	7.228
	Cu-Cu	2.594	0.014	0.429
	Multi scattering	3.077	0.003	1.000
	Multi scattering	3.269	0.002	3.820
CuNC-500	Cu-N	1.952	0.004	3.998
	C 2nd shell	2.624	0.008	10.499
	Cu-Cu	2.711	0.002	0.0563
	Multi scattering	2.798	0.002	0.999
	Multi scattering	3.269	0.002	3.257

What did change during the MIH heating was the peaks beyond the first shell. In **Figure 9b** a clear shoulder can be seen at 2.2 Å, which is much larger in the CuCh precursor and becomes less prominent with increasing MIH heating.[64, 65] This peak matches well with the second shell of carbon (Cu-N-C) around the central CuN_4 moiety as well as overlapping with a possible Cu-Cu peak. As such this peak was fitted with both at an effective pair distance of 2.4 and 2.5 Å respectively.[66] From the fitting one can see that the CN of the second shell did not decrease significantly from the initial value of 8 while the effective pair distance became elongated from 2.46 Å for CuCh to 2.62 Å for the CuNC samples (**Table 3**). This suggested partial damage of the second shell of carbons. Along with this, the Cu-Cu peak started at CN of 0.79 and an effective pair distance of 2.59 Å to a CN of 0.06 and an effective pair distance of 2.71 Å. This indicates that there is virtually no Cu^0 in these samples which is consistent with the absence of Cu nanoparticulates in the samples.

Finally, the outer shells of carbon could not be clearly distinguished due to multiple scatterings causing interference but two distinct multi scattering group fittings at the effective pair distance 2.7 and 3.2 Å were made and together could fit the broad EXAFS peak at 2.9 Å. These multi scattering peaks show a decay of the CN from 6.34 for CuCh to 3.26 for CuNC-500. This, along with the EXAFS data becoming smoother with a higher heating temperature, indicates a more disordered environment and significant defects in the carbon scaffold, in good agreement with results from the Raman measurements (**Figure 8**). Overall, results from the XAS measurements further confirmed that the CuN_4 moiety was largely retained after MIH treatment of

the CuCh precursor, although the outside carbon shells became increasingly defective. It was this unique CuN_4 SAC structure that was responsible for the remarkable $2e^-$ ORR activity observed below. Additionally, further study will be necessary to determine how well this remarkable conservation of the metal-N_4 structure can be extended to other metal centers. As if this can be expanded this is possibly a fast and easy method of producing many metal-N_4 catalyst that could be tuned for a desired reaction.

2.3.2 Electrocatalytic activity

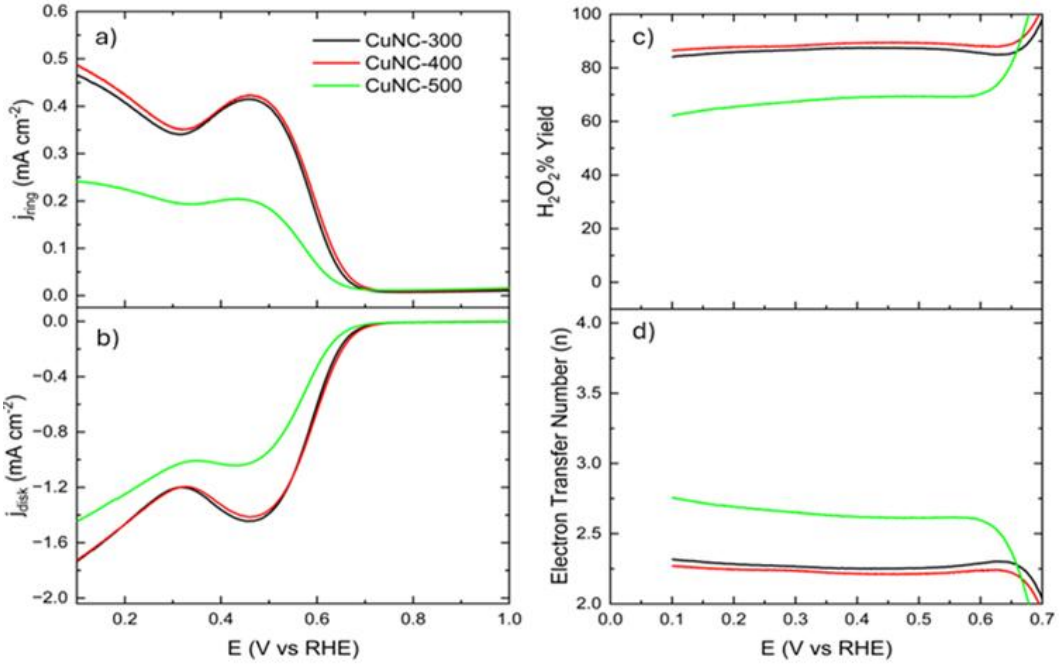

Figure 11. (a) RRDE ring and (b) disk voltammograms of the CuNC samples prepared at different MIH currents in oxygen-saturated 0.1 M KOH at the potential sweep rate of 10 mV s^{-1} and rotation rate of 1600 rpm. Ring potential was fixed at +1.5 V. (c) The corresponding H_2O_2 yield and (d) electron transfer number (n) at different electrode potentials.

The electrocatalytic activity of the CuNC samples were evaluated with a rotating ring-disk electrode (RRDE) in oxygen-saturated 0.1 M KOH. From the polarization curves in **Figure 11a-b**, all samples can be seen to exhibit an apparent electrocatalytic activity towards ORR, where nonzero voltametric currents started to appear as the disk potential was swept negatively. Yet the activity varied markedly among the series. Specifically, the onset potential (E_{onset}), which was defined as the potential to

reach the current density of 0.1 mA cm^{-2}, decreased in the order of CuNC-400 (+0.68 V) > CuNC-300 (+0.67 V) > CuNC-500 (+0.65 V). These onset potentials were remarkably close to the formal potential of +0.70 V for $2e^-$ ORR.[67] A similar trend can be seen with the collection current at the ring electrode, suggesting high electrocatalytic activity of the CuNC samples, and the CuNC-400 sample stood out as the best among the series in H_2O_2 production. The corresponding electron transfer number (n) and H_2O_2 % yield is depicted in **Figure 11c-d**. One can see that within the wide potential range of +0.65 to +0.10 V, CuNC-400 exhibited an n value of ca. 2.2 with a H_2O_2 yield close to 90%. Such performance was markedly better than those of CuNC-300 (2.3, 87%) and CuNC-500 (2.6, 69%).

Table 4. Summary of the ORR performance in 0.1 M KOH from Figure 11.

Sample	**E_{onset} (V)**	**j_{disk} (at +0.46 V, mA cm^{-2})**	**j_{ring} (at +0.46 V, mA cm^{-2})**	**n (+0.46 V)**	**H_2O_2% (+0.46V)**
CuNC-300	+0.67	-1.41	0.41	2.25	87.46
CuNC-400	+0.68	-1.45	0.43	2.21	89.44
CuNC-500	+0.65	-1.02	0.20	2.61	69.37
CuNC-400+EDTA	+0.66	-1.14	0.13	2.99	50.38
CuNC-400+KSCN	+0.65	-1.09	0.10	3.20	39.98

This suggests that 400 A was the optimal induction current in sample preparation (**Table 4**). In fact, the performance is highly comparable to the leading results of relevant SACs reported recently in the literature (**Table 5**). However the CuNC catalysts can be synthesized significantly faster due to few and quicker heating steps and exhibited excellent catalytic performance in several mediums. Also, in comparison to samples prepared at 400 A for different heating times (e.g., from 8 to 12 s), 10 s was identified as the best condition (not shown).

Table 5. Comparison of ORR performance with relevant SACs in the literature

Sample	**Active Moiety**	**Electrolyte**	**E_{onset} (V)**	**n (+0.46 V)**	**H_2O_2% (+0.46 V)**	**Reference**
CuNC-400	CuN_4	0.1 M KOH	+0.68	2.2	89.44	This Work
h_1-Pt-CuS_x	PtS_x	0.1 M $HClO_4$	+0.65	2.1	95	[68]
PFC-72-Co	CoN_4	0.1 M $HClO_4$	+0.68	2.2	90	[69]
Co-N-C	CoN_5	0.5 M NaCl	+0.61	2.1	95	[70]
ZnNC	ZnN_4	0.1 M KOH	+0.78	2.3	86	[71]

Co-N_2-C/HO	CoN_2	0.1 M KOH	+0.81	2.2	91	[72]
ZnCu-MOF (H)	Cu_1-O_3	0.1 M KOH	+0.74	2.2	90	[73]
Mn CD/C	MnN_4	0.1 M KOH	+0.79	2.2	90	[74]
W_1/NO-C	$W_1N_1O_2$-C	0.1 M KOH	+0.82	2.2	90	[75]
Fe-CNT	Fe-C-O	0.1 M KOH	+0.82	2.3	85	[76]

To unravel the catalytic active site, metal poisoning tests were conducted using KSCN and EDTA. The former is known to adsorb strongly onto metal sites whereas the latter is prone to chelation with single metal centers, where the blocking leads to apparent diminishment of the catalytic activity.[77-79] Experimentally, when KSCN or EDTA (10 mM) was added into the 0.1 M KOH electrolyte (**Figure 12a-b**), RRDE tests showed that the onset potential shifted negatively to +0.65 V for EDTA and +0.66 V for KSCN, along with a decrease of the disk current to -1.14 mA cm^{-2} for the former and -1.09 mA cm^{-2} for the latter at +0.46 V, indicating that the ORR activity was primarily due to the metal sites which could be effectively poisoned by the chelating agents. An even more significant change can be seen in the ring current, which decreased by more than 60% to 0.14 mA cm^{-2} for EDTA and 0.10 mA cm^{-2}

KSCN. In fact, the H_2O_2 yield diminished markedly to only 51% for EDTA and 40% for KSCN (**Figure 12c**). The fact that a similar poisoning effect was observed with KSCN and EDTA further suggests that the ORR active sites were indeed the Cu metal centers atomically dispersed within the carbon matrix.

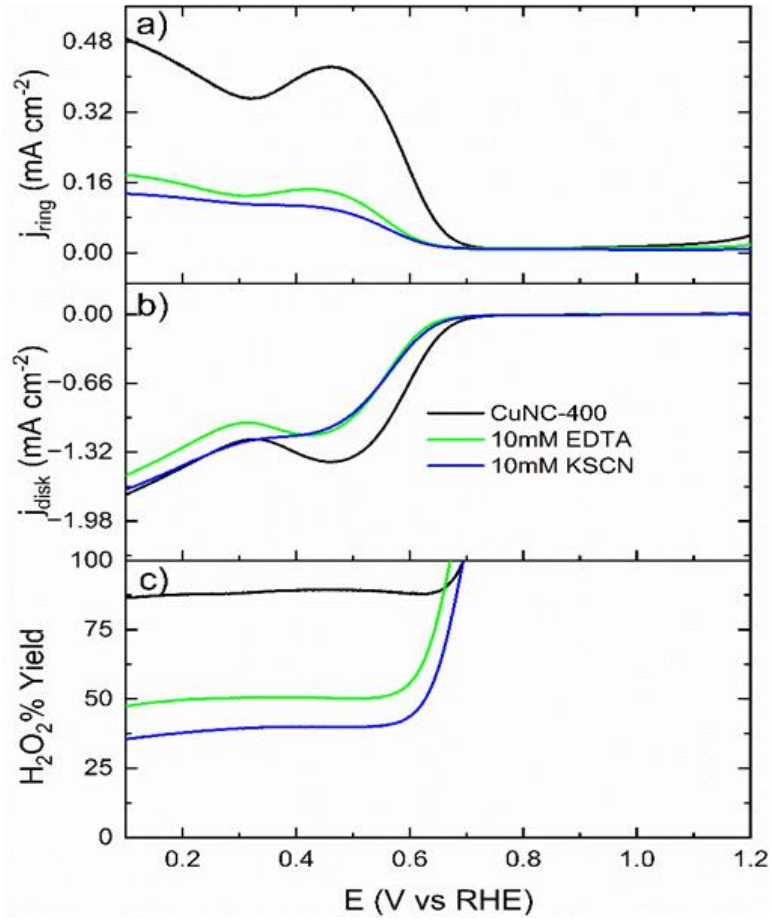

Figure 12. (a) RRDE ring and (b) disk voltammograms and (c) the H_2O_2 yield of CuNC-400 before and after the addition of 10 mM EDTA or KSCN in oxygen-saturated 0.1 M KOH at the potential sweep rate of 10 mV s^{-1} and rotation rate of 1600 rpm.

2.3.3 Disinfection applications

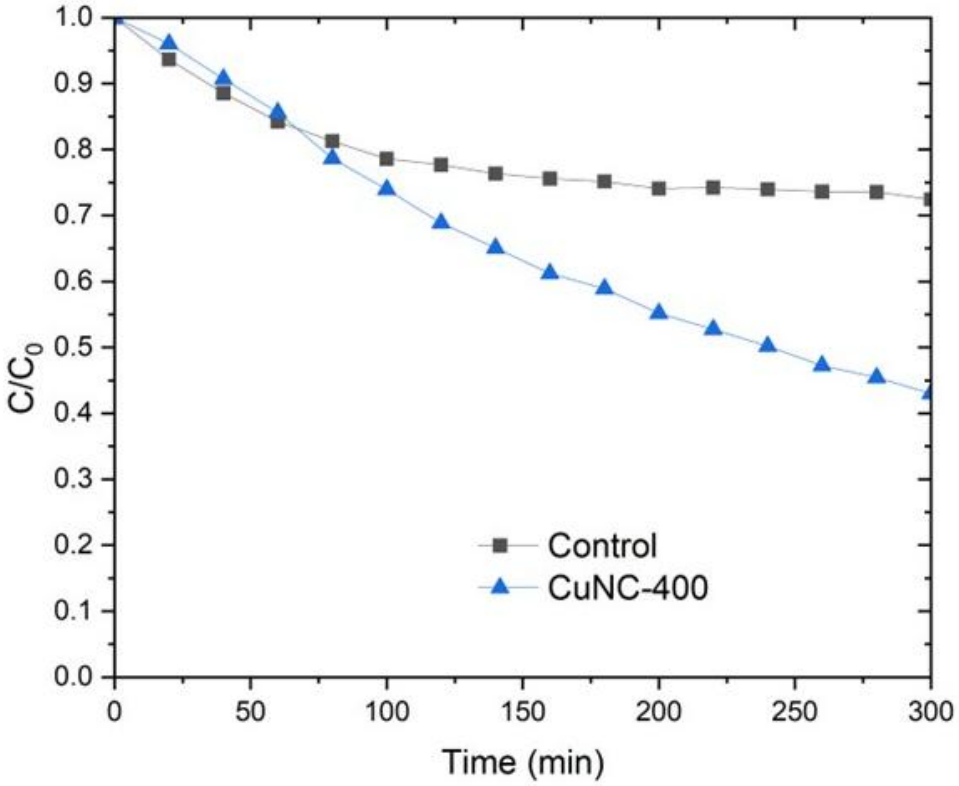

Figure 13. Methylene blue degradation by CuNC-400 at +0.46 V for 300 min in 0.1 M KOH, in comparison to the blank control with a bare electrode.

The selective production of H_2O_2 from oxygen reduction can be exploited for on-site applications, in particular, the degradation of organic dyes and disinfection of water. For the organic dye degradation, a 25 mg L^{-1} solution of MB in 0.1 M KOH was prepared and 75 mL was added into an electrochemical cell where the working electrode was held at the potential of +0.46 V.

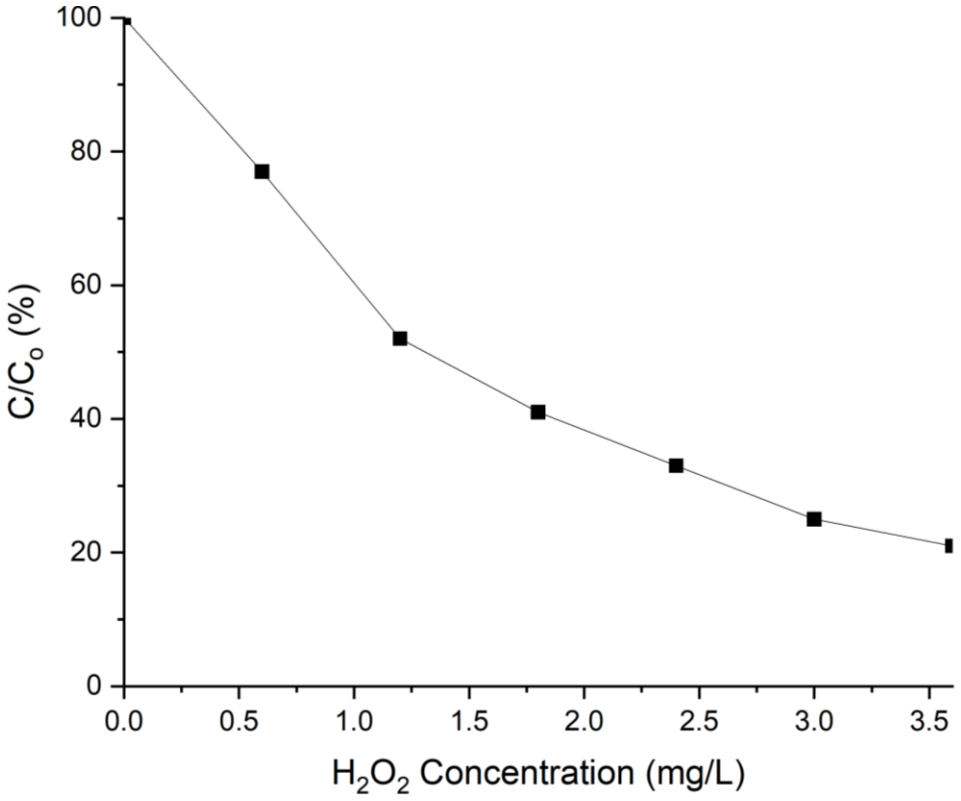

Figure 14. MB dye degradation with standard H_2O_2 solutions.

From **Figure 13**, one can see that 57.1% of the dye was removed after 300 min's electrochemical treatment with CuNC-400, corresponding to the production of ca. 1.7 mg L^{-1} of H_2O_2 (**Figure 14**). By contrast, for a bare electrode, less than 25% of MB was removed under the same experimental conditions.

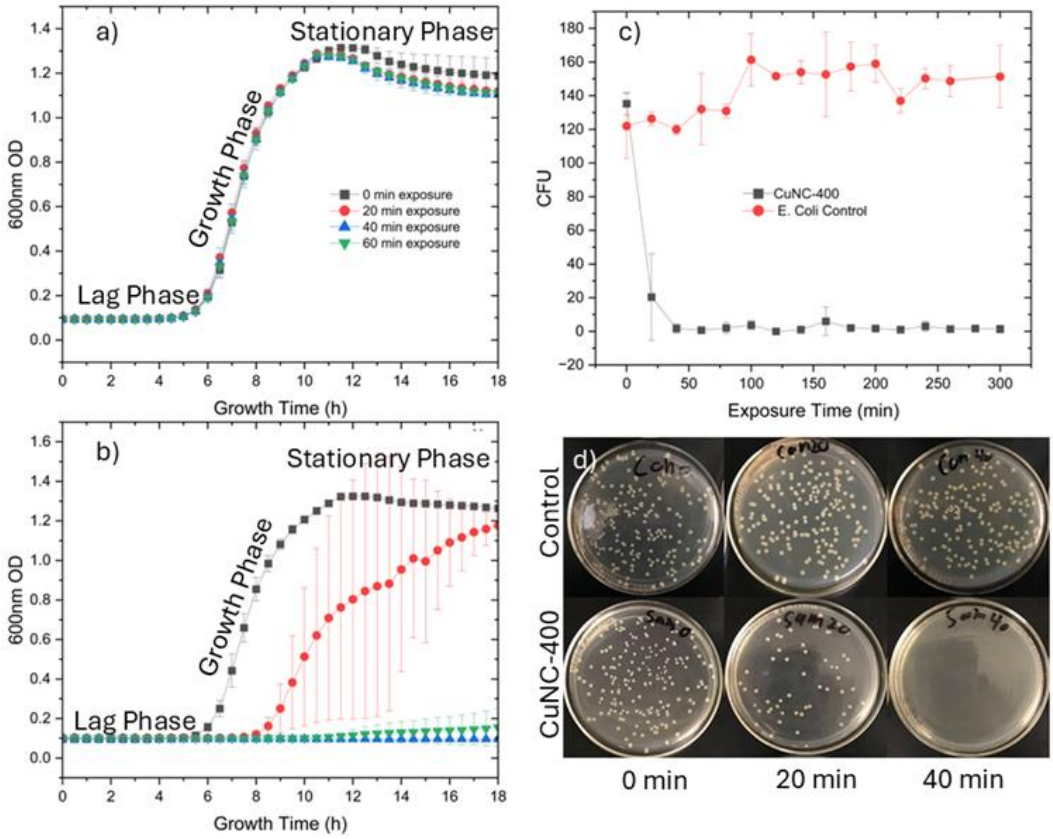

Figure 15. Growth curves of E. Coli in 96-well plates after electrochemical disinfection for up to 60 min with (a) a bare electrode and (b) a CuNC-400 modified electrode at +0.46 V. (c) CFU counts of E. Coli on LB petri dishes after electrochemical disinfection at +0.46 V for up to 300 min with a CuNC-400 modified electrode, in comparison to the blank control, with select photographs shown in (d).

Such a unique property could also be exploited for electrochemical disinfection of water. From **Figure 15a**, it can be seen that for the control experiment with a bare electrode where the potential was held at +0.46 V for up to 60 min, the E. coli cells exhibited a rather consistent growth curve with a lag phase of ca. 5.5 h. In stark contrast, the bacterial growth was markedly inhibited with a CuNC-400 modified

electrode (**Figure 15b**), where the lag phase can be seen to prolong to ca. 8 h after 20 min's electrochemical treatment, with the corresponding growth rate decreased by over 50% from 0.208 to 0.098 h^{-1}; and after 40 min's electrochemical treatment, bacterial growth was inhibited completely (**Table 6**).

Table 6. Comparison of *E. coli* growth in the absence and presence of electrochemical disinfection by CuNC-400 at +0.46 V for up to 60 min

Sample	Treatment Time (min)	Lag Phase (h)	Stationary Phase Start Time (h)	Growth Phase Rate (h^{-1})	Growth Phase Duration (h)	Generation Time (min)
E coli control	0	5	11.5	0.231	6.5	41.7
	20	5	11.5	0.228	6.5	41.8
	40	5	11.5	0.229	6.5	41.3
	60	5	11.5	0.230	6.5	40.6
CuNC-400	0	5.5	12.5	0.208	7	40.3
	20	8.5	-	0.098	>9	48.8
	40	No bacterial growth observed				

Additionally, the generation time (the amount of time needed for the splitting of a bacterial cell into two new cells) also increased from 40.3 min prior to electrochemical treatment to 48.8 min after 20 min's disinfection (**Table 6**). This all

indicates significant growth inhibition after just 20 min of exposure and nearly complete disinfection after 40 min's exposure.

2.4. Experimental Section

2.4.1 Chemicals

Sodium copper chlorophyllin (CuCh, 98.5%, Spectrum Chemical MFG. Corp.), ethylenediaminetetraacetic acid (EDTA, ≥99.0%, Aldrich), potassium thiocyanate (KSCN, 99.0%, Aldrich), nitric acid (HNO3, Aldrich), potassium hydroxide (KOH, Fisher Chemicals), Nafion®117 solution (5% in a mixture of lower aliphatic alcohols and water, Aldrich), and methylene blue hydrate (MB, Acros Organics) were all used as received. Water was purified with a Barnstead Nanopure Water System (resistivity 18.3 MΩ cm)

2.4.2 Sample synthesis

The MIH setup has been described in detail previously.[35, 36] In a typical experiment, 100 mg of CuCh was placed on an iron sheet lined with graphitic paper in a quartz tube that had been purged with Ar gas and subject to MIH treatment at controlled induction currents (X = 300, 400, and 500 A) for 10 s. After heating, the samples were washed with water, ethanol, and acetone, until a clear supernatant was produced. The samples were then subject to acid leaching to remove metal (oxide) nanoparticles whereby 10 mg of the sample were dispersed in 10 mL of 1.0 M HNO3 under magnetic stirring at room temperature for 3 h, followed by rinsing with a copious amount of Nanopure water. The resultant samples were denoted as CuNC-X.

2.4.3 Characterization

Transmission electron microscopy (TEM) images were acquired with a Tecni G2 operated at 200 kV. Scanning electron microscopy (SEM) and energy-dispersive X-ray spectroscopy (EDS) studies were conducted with an Apreo SEM microscope. X-ray photoelectron spectroscopy (XPS) measurements were carried out with a Thermo Fisher K-alpha system, where the binding energy was calibrated against the C 1s binding energy. Raman measurements were conducted using a Horiba Jobin Yvon Lab-RAM ARAMIS automated scanning confocal Raman microscope under 532 nm excitation. UV-vis absorption measurements were conducted with a Perkin-Elmer Lamda 35 spectrometer. X-ray absorption spectroscopy (XAS) measurements were conducted at the temperature of 10 K using an Oxford liquid helium cryostat at beamline 4–1 of the Stanford Synchrotron Radiation Light source. The obtained XAS data were reduced, fitted, and analyzed with the RSXAP software.[80] The Fourier Transform range was 3.5–12.5 and the fit range was 1.2-3.0. The theoretical functions for the simulated structure and each path were calculated by WebAtoms.[81]

2.4.4 Electrochemistry

Electrochemical performance was examined with a CHI 710 electrochemical workstation in a three-electrode configuration using a Hg/HgO reference electrode, a graphite rod counter electrode, and a gold ring-glassy carbon disk working electrode (disk surface area 0.196 cm2). The reference electrode was calibrated against a reversible hydrogen electrode (RHE), and all potentials in the present study were

referenced to the RHE. The catalyst inks were prepared by dispersing 2 mg of the samples prepared above into a mixed solution containing 300 μL of ethanol, 700 μL of H2O, and 10 μL of Nafion under sonication for 30 min. Then 20 μL of the inks was dropcast onto the glassy carbon disk electrode surface and dried naturally at room temperature before being coated with 3 μL of 20 wt % Nafion. The catalyst loading was ca. 0.204 mg cm^{-2}.

2.4.5 Methylene blue degradation

MB degradation was performed using the three-electrode setup described above, with the addition of 25 mg L^{-1} MB in the 0.1 M KOH supporting electrolyte. The electrode potential was held at +0.46 V and the absorbance of the electrolyte solution was monitored at different time points with a UV-vis spectrometer. A control experiment was conducted with the same setup but with only a bare working electrode.

2.4.6 Electrochemical disinfection of water

E. coli cells were grown in Luria−Bertani (LB) agar in a 37 °C incubator. A single colony was selected and used to inoculate 3 mL of LB broth and allowed to shake at 37 °C for 18 h. The resulting liquid was centrifuged at 5000 rpm for 5 min and resuspended in phosphate buffered saline (PBS) 3 times before being diluted to an optical density (OD) of 0.1 at 600 nm. Then 1 mL of the spiked PBS solution was diluted into 99 mL of sterile 0.5 M Na2SO4. 75 mL of this solution was poured into the electrochemical cell, and the working electrode was held at the potential of +0.46 V for 1 h, with 10 mL aliquots removed every 20 min and pipetted into a 96-well

plate along with 200 mL of sterile LB broth. The 96-well plate was placed in a Molecular Device VERSA max microplate reader, where the OD was measured at 600 nm every 30 min with intermittent shaking between each reading over a 18 h incubation period at 37 °C.

2.5. Conclusions

In this study, CuNC nanocomposites were prepared by MIH-based ultrafast synthesis using CuCh as the precursor. Due to the rapid heating, the peripheral hydrocarbon fragments of CuCh were thermally decomposed into graphitic carbon, whereas the CuN_4 coordination moieties were retained and dispersed within the carbon matrix. With this unique SAC structure, the CuNC nanocomposites exhibited apparent electrocatalytic activity towards the selective reduction of oxygen to hydrogen peroxide via the $2e^-$ ORR route; and the sample prepared at 400 A for 10 s displayed the best performance among the series, with up to 90% selectivity for H_2O_2 production, which was highly comparable to the leading results of relevant SACs reported in the literature. Such a unique property could be exploited for the on-site production of H_2O_2, a key ingredient in water treatment/disinfection, as demonstrated by the degradation of organic dye pollutants and eradication of waterborne pathogenic bacteria. Results of this study showcase the unique feasibility of MIH in the preparation of SACs as high-performance electrocatalysts.

2.6 References

(1) Goti, A.; Cardona, F. Hydrogen peroxide in green oxidation reactions: recent catalytic processes. 2008, Springer: pp 191-212.

(2) Chang, Q.; Zhang, P.; Mostaghimi, A. H. B.; Zhao, X.; Denny, S. R.; Lee, J. H.; Gao, H.; Zhang, Y.; Xin, H. L.; Siahrostami, S. Promoting H2O2 production via 2-electron oxygen reduction by coordinating partially oxidized Pd with defect carbon. *Nature communications* **2020**, *11* (1), 2178.

(3) Hu, Y.; Zhang, J.; Shen, T.; Li, Z.; Chen, K.; Lu, Y.; Zhang, J.; Wang, D. Efficient electrochemical production of H2O2 on hollow N-doped carbon nanospheres with abundant micropores. *ACS Applied Materials & Interfaces* **2021**, *13* (25), 29551-29557.

(4) Fukuzumi, S.; Yamada, Y.; Karlin, K. D. Hydrogen peroxide as a sustainable energy carrier: electrocatalytic production of hydrogen peroxide and the fuel cell. *Electrochimica acta* **2012**, *82*, 493-511.

(5) Campos-Martin, J. M.; Blanco-Brieva, G.; Fierro, J. L. G. Hydrogen peroxide synthesis: an outlook beyond the anthraquinone process. *Angewandte Chemie International Edition* **2006**, *45* (42), 6962-6984.

(6) Yang, S.; Verdaguer-Casadevall, A.; Arnarson, L.; Silvioli, L.; Colic, V.; Frydendal, R.; Rossmeisl, J.; Chorkendorff, I.; Stephens, I. E. L. Toward the decentralized electrochemical production of H2O2: a focus on the catalysis. *Acs Catalysis* **2018**, *8* (5), 4064-4081.

(7) Yu, B.; Diniz, J.; Lofgren, K.; Liu, Q.; Mercado, R.; Nichols, F.; Oliver, S. R. J.; Chen, S. Copper/Carbon Nanocomposites for Electrocatalytic Reduction of Oxygen to Hydrogen Peroxide. *ACS Sustainable Chemistry & Engineering* **2022**, *10* (47), 15501-15507.

(8) Jiang, Y.; Ni, P.; Chen, C.; Lu, Y.; Yang, P.; Kong, B.; Fisher, A.; Wang, X. Selective electrochemical H2O2 production through two-electron oxygen electrochemistry. *Advanced Energy Materials* **2018**, *8* (31), 1801909.

(9) Wang, W.; Hu, Y.; Liu, Y.; Zheng, Z.; Chen, S. Self-powered and highly efficient production of H2O2 through a Zn–Air battery with oxygenated carbon electrocatalyst. *ACS applied materials & interfaces* **2018**, *10* (38), 31855-31859.

(10) Pang, Y.; Xie, H.; Sun, Y.; Titirici, M.-M.; Chai, G.-L. Electrochemical oxygen reduction for H 2 O 2 production: catalysts, pH effects and mechanisms. *Journal of Materials Chemistry A* **2020**, *8* (47), 24996-25016.

(11) Xiao, M.; Chen, Y.; Zhu, J.; Zhang, H.; Zhao, X.; Gao, L.; Wang, X.; Zhao, J.; Ge, J.; Jiang, Z. Climbing the apex of the ORR volcano plot via binuclear site construction: electronic and geometric engineering. *Journal of the American Chemical Society* **2019**, *141* (44), 17763-17770.

(12) Zhang, Y.; Chen, X.; Zhang, H.; Ge, X. Screening of catalytic oxygen reduction reaction activity of 2, 9-dihalo-1, 10-phenanthroline metal complexes: The role of transition metals and halogen substitution. *Journal of Colloid and Interface Science* **2022**, *609*, 130-138.

(13) Siahrostami, S.; Verdaguer-Casadevall, A.; Karamad, M.; Deiana, D.; Malacrida, P.; Wickman, B.; Escudero-Escribano, M.; Paoli, E. A.; Frydendal, R.; Hansen, T. W. Enabling direct H2O2 production through rational electrocatalyst design. *Nature materials* **2013**, *12* (12), 1137-1143.

(14) Chen, Z.; Chen, S.; Siahrostami, S.; Chakthranont, P.; Hahn, C.; Nordlund, D.; Dimosthenis, S.; Nørskov, J. K.; Bao, Z.; Jaramillo, T. F. Development of a reactor with carbon catalysts for modular-scale, low-cost electrochemical generation of H 2 O 2. *Reaction chemistry & engineering* **2017**, *2* (2), 239-245.

(15) Zhao, X.; Yang, H.; Xu, J.; Cheng, T.; Li, Y. Bimetallic PdAu nanoframes for electrochemical H2O2 production in acids. *ACS Materials Letters* **2021**, *3* (7), 996-1002.

(16) Fei, H.; Dong, J.; Feng, Y.; Allen, C. S.; Wan, C.; Volosskiy, B.; Li, M.; Zhao, Z.; Wang, Y.; Sun, H. General synthesis and definitive structural identification of MN4C4 single-atom catalysts with tunable electrocatalytic activities. *Nature Catalysis* **2018**, *1* (1), 63-72.

(17) Campos, M.; Siriwatcharapiboon, W.; Potter, R. J.; Horswell, S. L. Selectivity of cobalt-based catalysts towards hydrogen peroxide formation during the reduction of oxygen. *Catalysis today* **2013**, *202*, 135-143.

(18) Yang, Y.; Zhang, H.; Liang, Z.; Yin, Y.; Mei, B.; Song, F.; Sun, F.; Gu, S.; Jiang, Z.; Wu, Y. Role of local coordination in bimetallic sites for oxygen reduction: A theoretical analysis. *Journal of Energy Chemistry* **2020**, *44*, 131-137.

(19) Zhu, T.; Han, Y.; Liu, S.; Yuan, B.; Liu, Y.; Ma, H. Porous materials confining single atoms for catalysis. *Frontiers in Chemistry* **2021**, *9*, 717201.

(20) Liu, K.; Fu, J.; Lin, Y.; Luo, T.; Ni, G.; Li, H.; Lin, Z.; Liu, M. Insights into the activity of single-atom Fe-NC catalysts for oxygen reduction reaction. *Nature Communications* **2022**, *13* (1), 2075.

(21) Song, M.; Liu, W.; Zhang, J.; Zhang, C.; Huang, X.; Wang, D. Single-atom catalysts for H2O2 electrosynthesis via two-electron oxygen reduction reaction. *Advanced Functional Materials* **2023**, *33* (15), 2212087.

(22) Sun, Y.; Silvioli, L.; Sahraie, N. R.; Ju, W.; Li, J.; Zitolo, A.; Li, S.; Bagger, A.; Arnarson, L.; Wang, X. Activity–selectivity trends in the electrochemical production of hydrogen peroxide over single-site metal–nitrogen–carbon catalysts. *Journal of the American Chemical Society* **2019**, *141* (31), 12372-12381.

(23) Yang, L.; Xu, H.; Liu, H.; Zeng, X.; Cheng, D.; Huang, Y.; Zheng, L.; Cao, R.; Cao, D. Oxygen-reconstituted active species of single-atom Cu catalysts for oxygen reduction reaction. *Research* **2020**.

(24) Wang, J.; Li, K.; Xu, R.; Li, S.; Li, Y.; Xia, M.; John, S. T.; Wu, Z. Rational design of the first and second coordination spheres for copper single-atom catalyst to boost highly efficient oxygen reduction. *Applied Surface Science* **2022**, *605*, 154832.

(25) Zhu, W.; Chen, S. Recent Progress of Single-atom Catalysts in the Electrocatalytic Reduction of Oxygen to Hydrogen Peroxide. *Electroanalysis* **2020**, *32* (12), 2591-2602.

(26) Li, H.; Zhu, B.; Cheng, B.; Luo, G.; Xu, J.; Cao, S. Single-atom Cu anchored on N-doped graphene/carbon nitride heterojunction for enhanced photocatalytic H2O2 production. *Journal of Materials Science & Technology* **2023**, *161*, 192-200.

(27) Wang, Y.; Xue, Y.; Zhang, C. Copper embedded in nitrogen-doped carbon matrix derived from metal-organic frameworks for boosting peroxide production and electro-Fenton catalysis. *Electrochimica Acta* **2021**, *368*, 137643.

(28) Liu, Q.; Chen, S. W. Ultrafast synthesis of electrocatalysts. *Trends in Chemistry* **2022**.

(29) Lucía, O.; Maussion, P.; Dede, E. J.; Burdío, J. M. Induction heating technology and its applications: past developments, current technology, and future challenges. *IEEE Transactions on industrial electronics* **2013**, *61* (5), 2509-2520.

(30) Liu, Q.; McNair, S.; Nichols, F.; Lu, B.; Yu, B.; Pan, D.; Ko, J.; Bhuller, A.; Bridges, F.; Chen, S. Ultrafast synthesis of cobalt/carbon nanocomposites by magnetic induction heating for oxygen evolution reaction. *Advanced Sensor and Energy Materials* **2023**, *2* (1), 100046. DOI: https://doi.org/10.1016/j.asems.2023.100046.

(31) Wang, W. E. I.; Tuci, G.; Duong-Viet, C.; Liu, Y.; Rossin, A.; Luconi, L.; Nhut, J.-M.; Nguyen-Dinh, L.; Pham-Huu, C.; Giambastiani, G. Induction heating: An enabling technology for the heat management in catalytic processes. *ACS Catalysis* **2019**, *9* (9), 7921-7935.

(32) Zhao, T.; Xu, C.; Ma, W.; Liu, Z.; Zhou, T.; Liu, Z.; Feng, S.; Zhu, M.; Kang, N.; Sun, D.-M. Ultrafast growth of nanocrystalline graphene films by quenching and grain-

size-dependent strength and bandgap opening. *Nature communications* **2019**, *10* (1), 4854.

(33) Lu, B.; Liu, Q.; Wang, C.; Masood, Z.; Morris, D. J.; Nichols, F.; Mercado, R.; Zhang, P.; Ge, Q.; Xin, H. L.; et al. Ultrafast Preparation of Nonequilibrium FeNi Spinels by Magnetic Induction Heating for Unprecedented Oxygen Evolution Electrocatalysis. *Research 2022*, 9756983. DOI: 10.34133/2022/9756983 (accessed 2023/03/03).

(34) Liu, Q. M.; Lu, B. Z.; Nichols, F.; Ko, J.; Mercado, R.; Bridges, F.; Chen, S. W. Rapid preparation of carbon-supported ruthenium nanoparticles by magnetic induction heating for efficient hydrogen evolution reaction in both acidic and alkaline media. *Susmat* **2022**, *2* (3), 335-346. DOI: 10.1002/sus2.66.

(35) Yu, B. Z.; Liu, Q. M.; Pan, D. J.; Singewald, K.; Dubois, D.; Tressel, J.; Hou, B. Y.; Millhauser, G. L.; Bridges, F.; Chen, S. W. Ultrafast preparation of ruthenium nanoparticle/molybdenum oxide/nitrogen-doped carbon nanocomposites by magnetic induction heating for efficient hydrogen evolution reaction. *J Mater Chem A* **2024**, *12* (26), 16087-16097. DOI: 10.1039/d4ta00884g.

(36) Pan, D. J.; Liu, Q. M.; Yu, B. Z.; DuBois, D. B.; Tressel, J.; Yu, S.; Kaleekal, N.; Trabanino, S.; Jeon, Y.; Bridges, F.; et al. Rapid Synthesis of Ruthenium-Copper Nanocomposites as High-Performance Bifunctional Electrocatalysts for Electrochemical Water Splitting. *Small* **2024**, 2404729. DOI: 10.1002/smll.202404729.

(37) Liu, Q. M.; Nichols, F.; Bhuller, A.; Singewald, K.; Kuo, H. L.; Lu, J. Q.; Millhauser, G. L.; Bridges, F.; Ge, Q. F.; Chen, S. W. Ultrafast synthesis of amorphous

molybdenum sulfide by magnetic induction heating for hydrogen evolution reaction. *Applied Catalysis B-Environment and Energy* **2024**, *342*, 123399. DOI: 10.1016/j.apcatb.2023.123399.

(38) Kumawat, M. K.; Thakur, M.; Gurung, R. B.; Srivastava, R. Graphene quantum dots for cell proliferation, nucleus imaging, and photoluminescent sensing applications. *Scientific reports* **2017**, *7* (1), 15858.

(39) Miura, A.; Takei, T.; Kumada, N. Synthesis of Cu3N from CuO and NaNH2. *Journal of Asian Ceramic Societies* **2014**, *2* (4), 326-328.

(40) Li, Y.; Xiao, J.; Shubina, T. E.; Chen, M.; Shi, Z.; Schmid, M.; Steinrück, H.-P.; Gottfried, J. M.; Lin, N. Coordination and metalation bifunctionality of Cu with 5, 10, 15, 20-tetra (4-pyridyl) porphyrin: toward a mixed-valence two-dimensional coordination network. *Journal of the American Chemical Society* **2012**, *134* (14), 6401-6408.

(41) Liang, Z.-Q.; Zhuang, T.-T.; Seifitokaldani, A.; Li, J.; Huang, C.-W.; Tan, C.-S.; Li, Y.; De Luna, P.; Dinh, C. T.; Hu, Y. Copper-on-nitride enhances the stable electrosynthesis of multi-carbon products from CO2. *Nature communications* **2018**, *9* (1), 3828.

(42) Sithole, R. K.; Machogo, L. F. E.; Airo, M. A.; Gqoba, S. S.; Moloto, M. J.; Shumbula, P.; Van Wyk, J.; Moloto, N. Synthesis and characterization of Cu 3 N nanoparticles using pyrrole-2-carbaldpropyliminato Cu (II) complex and Cu (NO 3) 2 as single-source precursors: the search for an ideal precursor. *New Journal of Chemistry* **2018**, *42* (4), 3042-3049.

(43) Finšgar, M. X-ray excited Auger Cu L3L4, 5M4, 5 spectra measured at low take-off angles as a fingerprint for a Cu-organics connection. *Journal of Electron Spectroscopy and Related Phenomena* **2018**, *222*, 10-14.

(44) Khan, M. A.; Nayan, N.; Ahmad, M. K.; Soon, C. F. Surface study of CuO nanopetals by advanced nanocharacterization techniques with enhanced optical and catalytic properties. *Nanomaterials* **2020**, *10* (7), 1298.

(45) Chen, X.; Wang, X.; Fang, D. A review on C1s XPS-spectra for some kinds of carbon materials. *Fullerenes, Nanotubes and Carbon Nanostructures* **2020**, *28* (12), 1048-1058.

(46) Lian, W.-N.; Shiue, J.; Wang, H.-H.; Hong, W.-C.; Shih, P.-H.; Hsu, C.-K.; Huang, C.-Y.; Hsing, C.-R.; Wei, C.-M.; Wang, J.-K. Rapid detection of copper chlorophyll in vegetable oils based on surface-enhanced Raman spectroscopy. *Food Additives & Contaminants: Part A* **2015**, *32* (5), 627-634.

(47) Hildebrandt, P.; Spiro, T. G. Surface-enhanced resonance Raman spectroscopy of copper chlorophyllin on silver and gold colloids. *The Journal of Physical Chemistry* **1988**, *92* (12), 3355-3360.

(48) He, T.; Zhang, Y. Q.; Chen, Y.; Zhang, Z. Z.; Wang, H. Y.; Hu, Y. F.; Liu, M.; Pao, C. W.; Chen, J. L.; Chang, L. Y.; et al. Single iron atoms stabilized by microporous defects of biomass-derived carbon aerogels as high-performance cathode electrocatalysts for aluminum-air batteries. *J Mater Chem A* **2019**, *7* (36), 20840-20846. DOI: 10.1039/c9ta05981d.

(49) Caswell, D. S.; Spiro, T. G. Ultraviolet resonance Raman spectroscopy of imidazole, histidine, and Cu (imidazole) 42+: Implications for protein studies. *Journal of the American Chemical Society* **1986**, *108* (21), 6470-6477.

(50) Thamann, T. J.; Frank, P.; Willis, L. J.; Loehr, T. M. Normal coordinate analysis of the copper center of azurin and the assignment of its resonance Raman spectrum. *Proceedings of the National Academy of Sciences* **1982**, *79* (20), 6396-6400.

(51) Prakash, O.; Singh, S. K.; Singh, B.; Singh, R. K. Investigation of coordination properties of isolated adenine to copper metal: a systematic spectroscopic and DFT study. *Spectrochimica Acta Part A: Molecular and Biomolecular Spectroscopy* **2013**, *112*, 410-416.

(52) Chan, H. Y. H.; Weaver, M. J. A vibrational structural analysis of benzotriazole adsorption and phase film formation on copper using surface-enhanced Raman spectroscopy. *Langmuir* **1999**, *15* (9), 3348-3355.

(53) Siiman, O.; Young, N. M.; Carey, P. R. Resonance raman spectra of" blue" copper proteins and the nature of their copper sites. *Journal of the American Chemical Society* **1976**, *98* (3), 744-748.

(54) Lee, W.-J.; Chang, Y.-H. Growth without postannealing of monoclinic VO2 thin film by atomic layer deposition using VCl4 as precursor. *Coatings* **2018**, *8* (12), 431.

(55) Sajeev, A.; Paul, A. M.; Nivetha, R.; Gothandapani, K.; Gopal, T. S.; Jacob, G.; Muthuramamoorty, M.; Pandiaraj, S.; Alodhayb, A.; Kim, S. Y. Development of Cu3N electrocatalyst for hydrogen evolution reaction in alkaline medium. *Scientific Reports* **2022**, *12* (1), 2004.

(56) Bunker, G. *Introduction to XAFS: a practical guide to X-ray absorption fine structure spectroscopy*; Cambridge University Press, 2010.

(57) Rudolph, J.; Jacob, C. R. Revisiting the dependence of Cu K-edge X-ray absorption spectra on oxidation state and coordination environment. *Inorganic Chemistry* **2018**, *57* (17), 10591-10607.

(58) Tomson, N. C.; Williams, K. D.; Dai, X.; Sproules, S.; DeBeer, S.; Warren, T. H.; Wieghardt, K. Re-evaluating the Cu K pre-edge XAS transition in complexes with covalent metal–ligand interactions. *Chemical science* **2015**, *6* (4), 2474-2487.

(59) Alwis, L.; Mucalo, M. R.; Ingham, B.; Kappen, P. A Combined SNIFTIRS and XANES Study of Electrically Polarized Copper Electrodes in DMSO and DMF Solutions of Cyanate (NCO−), Thiocyanate (NCS−) and Selenocyanate (NCSe−) Ions. *Journal of The Electrochemical Society* **2015**, *162* (7), H434.

(60) Onori, G.; Santucci, A.; Belli, A. S. M.; Della Longa, S.; Bianconi, A.; Palladino, L. Cu K-edge XANES of Cu (II) ions in aqueous solution: a measure of the axial ligand distances. *Chemical physics letters* **1988**, *149* (3), 289-294.

(61) Sokol, H. J.; Ebrahim, A. M.; Caratzoulas, S.; Frenkel, A. I.; Valla, J. A. In Situ XAFS, XRD, and DFT characterization of the sulfur adsorption sites on Cu and Ce exchanged Y zeolites. *The Journal of Physical Chemistry C* **2022**, *126* (3), 1496-1512.

(62) Geoghegan, B. L.; Liu, Y.; Peredkov, S.; Dechert, S.; Meyer, F.; DeBeer, S.; Cutsail Iii, G. E. Combining valence-to-core x-ray emission and Cu k-edge x-ray absorption spectroscopies to experimentally assess oxidation state in organometallic Cu

(I)/(II)/(III) complexes. *Journal of the American Chemical Society* **2022**, *144* (6), 2520-2534.

(63) Kuzmin, A.; Anspoks, A.; Kalinko, A.; Timoshenko, J.; Nataf, L.; Baudelet, F.; Irifune, T. Origin of Pressure-Induced Metallization in Cu3N: An X-ray Absorption Spectroscopy Study. *physica status solidi (b)* **2018**, *255* (11), 1800073.

(64) Liu, Q.; Peng, Y.; Masood, Z.; DuBois, D.; Tressel, J.; Nichols, F.; Ashby, P.; Mercado, R.; Assafa, T.; Pan, D. Stable Cuprous Hydroxide Nanostructures by Organic Ligand Functionalization. *Advanced Materials* **2023**, *35* (8), 2208665.

(65) Grundner, S.; Markovits, M. A. C.; Li, G.; Tromp, M.; Pidko, E. A.; Hensen, E. J. M.; Jentys, A.; Sanchez-Sanchez, M.; Lercher, J. A. Single-site trinuclear copper oxygen clusters in mordenite for selective conversion of methane to methanol. *Nature communications* **2015**, *6* (1), 7546.

(66) Lieberman, R. L.; Kondapalli, K. C.; Shrestha, D. B.; Hakemian, A. S.; Smith, S. M.; Telser, J.; Kuzelka, J.; Gupta, R.; Borovik, A. S.; Lippard, S. J.; et al. Characterization of the particulate methane monooxygenase metal centers in multiple redox states by X-ray absorption spectroscopy. *Inorganic Chemistry* **2006**, *45* (20), 8372-8381. DOI: 10.1021/ic060739v.

(67) Li, N.; Huang, C.; Wang, X.; Feng, Y.; An, J. Electrosynthesis of hydrogen peroxide via two-electron oxygen reduction reaction: A critical review focus on hydrophilicity/hydrophobicity of carbonaceous electrode. *Chemical Engineering Journal* **2022**, *450*, 138246.

(68) Shen, R.; Chen, W.; Peng, Q.; Lu, S.; Zheng, L.; Cao, X.; Wang, Y.; Zhu, W.; Zhang, J.; Zhuang, Z. High-concentration single atomic Pt sites on hollow CuSx for selective O2 reduction to H2O2 in acid solution. *Chem* **2019**, *5* (8), 2099-2110.

(69) Zhao, X.; Yin, Q.; Mao, X.; Cheng, C.; Zhang, L.; Wang, L.; Liu, T.-F.; Li, Y.; Li, Y. Theory-guided design of hydrogen-bonded cobaltoporphyrin frameworks for highly selective electrochemical H2O2 production in acid. *Nature Communications* **2022**, *13* (1), 2721.

(70) Zhao, Q.; Wang, Y.; Lai, W.-H.; Xiao, F.; Lyu, Y.; Liao, C.; Shao, M. Approaching a high-rate and sustainable production of hydrogen peroxide: oxygen reduction on Co–N–C single-atom electrocatalysts in simulated seawater. *Energy & environmental science* **2021**, *14* (10), 5444-5456.

(71) Tang, J.; Xu, S.; Sun, K.; Gao, X.; Chen, A.; Tian, S.; Zhou, D.; Sun, X. Recycling synthesis of single-atom Zn-nitrogen-carbon catalyst for electrocatalytic reduction of O2 to H2O2. *Science China Materials* **2022**, *65* (12), 3490-3496.

(72) Hwang, C. K.; Kim, S.; Yoon, K. R.; Le, T. T.; Hoang, C. V.; Choi, J. W.; Zhang, W.; Paek, S. Y.; Lee, C. H.; Lee, J. H. Arc plasma-deposited Co single-atom catalysts supported on an aligned carbon nanofiber for hydrogen peroxide electrosynthesis and an electro-Fenton process. *Carbon Energy* **2024**, *6* (11), e582.

(73) Pei, Z.; Li, Y.; Fan, G.; Guo, Y.; Luan, D.; Gu, X.; Lou, X. W. Low-Coordinated Conductive ZnCu Metal-Organic Frameworks for Highly Selective H2O2 Electrosynthesis. *Small* **2024**, 2403808.

(74) Zeng, Y.; Tan, X.; Zhuang, Z.; Chen, C.; Peng, Q. Nature-inspired N, O Co-Coordinated Manganese Single-Atom Catalyst for Efficient Hydrogen Peroxide Electrosynthesis. *Angewandte Chemie* **2024**, e202416715.

(75) Zhang, F.; Zhu, Y.; Tang, C.; Chen, Y.; Qian, B.; Hu, Z.; Chang, Y. C.; Pao, C. W.; Lin, Q.; Kazemi, S. A. High-efficiency electrosynthesis of hydrogen peroxide from oxygen reduction enabled by a tungsten single atom catalyst with unique terdentate N1O2 coordination. *Advanced Functional Materials* **2022**, *32* (16), 2110224.

(76) Jiang, K.; Back, S.; Akey, A. J.; Xia, C.; Hu, Y.; Liang, W.; Schaak, D.; Stavitski, E.; Nørskov, J. K.; Siahrostami, S. Highly selective oxygen reduction to hydrogen peroxide on transition metal single atom coordination. *Nature communications* **2019**, *10* (1), 3997.

(77) Zaitoun, M. A.; Lin, C.-T. Chelating behavior between metal ions and EDTA in sol− gel matrix. *The Journal of Physical Chemistry B* **1997**, *101* (10), 1857-1860.

(78) Smith, S. W. The role of chelation in the treatment of other metal poisonings. *Journal of Medical Toxicology* **2013**, *9*, 355-369.

(79) Mercado, R.; Wahl, C.; En Lu, J.; Zhang, T.; Lu, B.; Zhang, P.; Lu, J. Q.; Allen, A. L.; Zhang, J. Z.; Chen, S. Nitrogen-doped porous carbon cages for electrocatalytic reduction of oxygen: enhanced performance with iron and cobalt dual metal centers. *ChemCatChem* **2020**, *12* (12), 3230-3239.

(80) Booth, C. H.; Bridges, F. Real-Space X-ray Absorption Package (RSXAP). **2021**.

(81) Ravel, B.; Newville, M. ATHENA, ARTEMIS, HEPHAESTUS: data analysis for X-ray absorption spectroscopy using IFEFFIT. *Journal of synchrotron radiation* **2005**, *12* (4), 537-541.

Chapter 3 Ultrafast Modification of Metal Tetraphenyl porphyrin Complexes by Magnetic Induction Heating for the Selective Electroreduction of Oxygen to Hydrogen Peroxide

3.1 Abstract

The two-electron oxygen reduction reaction has emerged as an effective strategy to replace the anthraquinone process for the on-site production of hydrogen peroxide. Herein, copper and cobalt tetraphenyl porphyrin complexes are modified using magnetic induction heating to produce M-N-C nanocomposites. X-ray absorption spectroscopy, X-ray photoelectron spectroscopy, and Raman measurements confirm the retention of the metal-N_4 coordination moiety. In electrochemical tests the obtained single atom catalysts exhibit an apparent electrocatalytic activity towards the selective two-electron oxygen reduction to hydrogen peroxide in alkaline media, with a H_2O_2 yield up to 90%. Such a unique property can be exploited for on-site water treatment/disinfection, as manifested in the effective degradation of methylene blue dye and removal of *Escherichia coli* (*E. coli*). Results from this study highlight the unique potential of magnetic induction heating in the ultrafast production of functional nanocomposites as high-performance electrocatalysts.

3.2. Introduction

Hydrogen peroxide (H_2O_2) is listed as one of the 100 most important chemicals in the world that has found a wide range of applications, such as chemical manufacturing, wastewater treatment, and textile bleaching.[1-3] At present, large scale H_2O_2 production relies predominantly on the industrial anthraquinone process that is inherently energy-intensive and generates environmentally hazardous byproducts.[4] Moreover, the storage and transportation of the concentrated H_2O_2 solutions (regularly >70 wt%) pose

significant personal safety and environmental risks, particularly in the event of a chemical spill.[5, 6] However, most end-use applications demand significantly lower concentrations, ca. 30% for chemical synthesis, 6% for water treatment and 3% for first aid disinfectant,[7] which has motivated the development of decentralized onsite H_2O_2 production methods. Here the two-electron ($2e^-$ ORR) has emerged offering sustainable and scalable H_2O_2 production under mild conditions.[8] The major hurtle in this electrochemical approach is the selectivity of the $2e^-$ pathway ($O_2 + 2H^+ + 2e^- \rightarrow H_2O_2$) over the $4e^-$ one ($O_2 + 4H^+ + 4e^- \rightarrow H_2O$).[9, 10] Mechanistically the two methods are governed by the O_2 binding configuration to the catalytic active site.[11] The $2e^-$ pathway is facilitated by end-on binding of the O_2 molecules onto the catalytic active centers leading to a formation of the *OOH intermediate and partial reduction to H_2O_2, while the $4e^-$ pathway favors a side-on binding which causes a stretching of the O-O bond and leads to its breakage and complete reduction to H_2O.[12] These considerations underscore the importance of active site design to stabilize favorable reaction intermediates and suppress the O-O bond dissociation. To date, noble metal-based nanoparticles have demonstrated the highest activity towards selective $2e^-$ ORR. For instance, $PtHg_4$ alloy nanoparticles have been the benchmark catalyst exhibiting selectivity over 95% at low overpotential (η) of -60 mV towards $2e^-$ ORR for H_2O_2 production in alkaline media.[13] Similarly, PdAu alloy nanoparticles display a high activity in acidic media and >90% selectivity at a moderate overpotential of -100 mV.[14] Nevertheless, the high cost and limited natural abundance of the precious metals hinder the widespread applications of these noble metal-based catalysts. Consequently recent

efforts have been increasingly focused on the development off carbon-based nanocomposites with earth-abundant transition metals, such as Co, Cu, and Ni, which offer a promising balance between catalytic performance, cost and scalability.[15, 16] For instance, Yu et al.[17] prepared copper/carbon nanocomposites by controlled pyrolysis of a copper-containing metal organic framework and observed an apparent electrocatalytic activity towards 2e- ORR in alkaline media, which was markedly enhanced by electrochemical activation, with the selectivity increased from ca. 45% to 68% (at +0.1 V), due to the enrichment of the Cu_2O species. Wang et al.[18] prepared nanocomposites consisting of cobalt-doped carbon nanotubes and MXenes, This was done by the formation of MXenes via hydrofluoric acid stirring of Ti_3AlC_2 followed by the aqueous mixing and pyrolysis of the MXenes, dicyandiamide and Co precursors to produce a bamboo like carbon nanotube structure. Which possessed a high electrocatalytic activity towards 2e- ORR at 95% selectivity, by tuning the extranuclear Co electrons at the Co-NCNT/MXene interface and hence modulating the *OOH binding energy. Carbon-based single atom catalysts (SACs) represent another viable option with significant promise, where the high selectivity for 2e- ORR can be facilitated by the spatial separation of the active sites thusly end-on adsorption of intermediates are favored. Among these, metal-nitrogen-codoped carbon (M-N-C) nanocomposites that feature porphyrin-like metal-N_4 moieties have been attracting particular attention.[19, 20] For instance, Cu-N-C and Co-N-C have been identified as some of the most promising SACs. Ye et al.[21] prepared Cu-N-C and Co-N-C nanosheets via the wet injection of a polystyrene emulsion with the metal precursors

followed by mixing and pyrolysis. They observed a high current density of 2.15 mA cm^{-2} and near 100% selectivity towards 2e- ORR in 0.1 M KOH, as compared to Cu nanoparticles, due to increased side-on O_2 binding. Similarly, Zhu et al.[22] synthesized CoN_4 nanocomposites by the aqueous mixing of a covalent triazine framework, CTF-B, and Co precursor followed by a dual heating step under Ar and then CO_2. After which they observed spin state modulation via the Co-N bond length and were able to mitigate the normally high *OOH adsorption on CoN_4 by a increase of the Co spin state reaching a $2e^-$ ORR selectivity of 91%. In these earlier studies, the M-N-C nanocomposites were prepared by controlled pyrolysis which is time and energy intensive and typically contained a mix of nanoparticulates and single atom moieties. Recently, magnetic induction heating (MIH) has emerged as an ultrafast synthesis technique that utilizes the instant generation of an eddy current when a conductor is immersed into a strong AC magnetic field to heat a metal surface reaching a temperature over 1000 °C within seconds.[23] Such Joule heating can be readily controlled by the induction current and heating time.[24] This has indeed been demonstrated in several recent studies in the preparation of a variety of functional nanocomposites that exhibited unprecedented electrocatalytic activity towards hydrogen evolution reaction (HER) and oxygen evolution reaction (OER), e.g., FeNi spinels with a good mixing of the Fe and Ni phases,[25] defective carbon-encapsulated Co nanoparticle composites,[24] amorphous chlorophyllin derived CuN_4 electrocatalysts[26] and mixed phase titanium suboxide.[27] This was largely ascribed to

the rapid heating that resulted in the formation of nonequilibrium structure and/or incomplete thermal decomposition of the precursors.

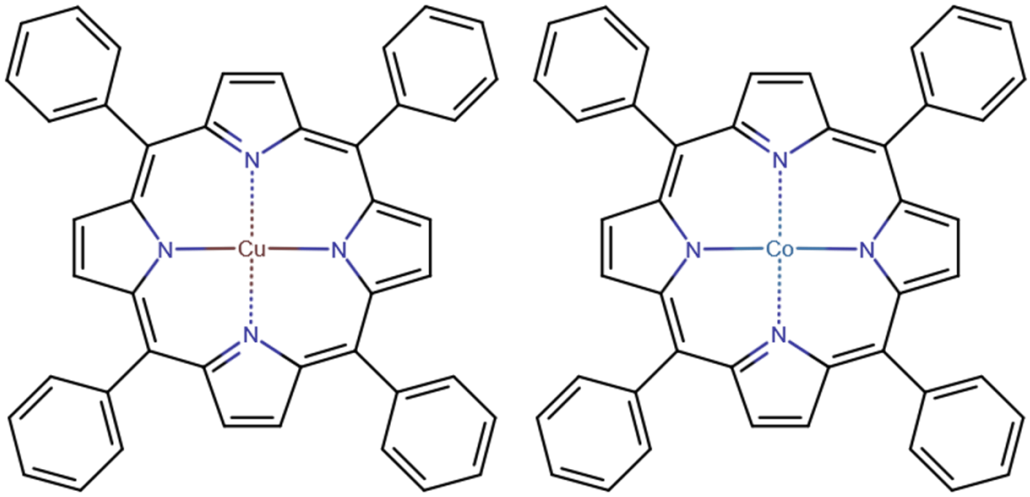

Figure 1. Skeletal model of copper tetraphenyl porphyrin and cobalt tetraphenyl porphyrin

Herein, metal tetraphenyl porphyrins (MTPP, **Figure 1**), a porphyrin derivative with a metal center chelated to four pyrrolic N (MN_4), was treated with MIH at controlled induction currents for 10 seconds. The obtained M-N-C nanocomposites exhibited an excellent performance towards the selective $2e^-$ ORR to H_2O_2 in alkaline media. This was due to the rapid heating that facilitated the retention of the MN_4 moiety of MTPP which is known to be catalytically active towards $2e^-$ ORR.[28-31,] Electrochemical measurements showed that the CuTPP at 300 A for 10 s stood out as the best among the series and possessed a selectivity up to 89% of H_2O_2 yield and CoTPP 200A with a selectivity of 85%, a unique activity that could be exploited for the on-site effective degradation of organic dye and electrochemical disinfection of water.

3.3. Results and Discussion

3.3.1 Structural characterizations

First structural insights were gathered from XPS measurements. From the survey spectra (**Figure 2**), the Co 2p, O 1s, N 1s, and C 1s electrons can be readily resolved at ca. 780, 530, 400, and 284 eV for all the CoTPP samples.

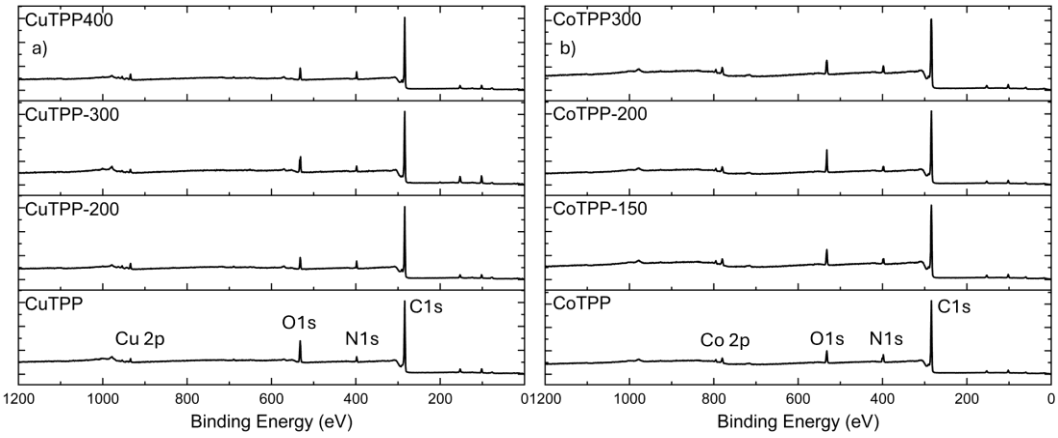

Figure 2. XPS Survey spectra of the (a) CuTTP and (b) CoTPP sample series.

From the integrated peak areas, the elemental contents can be estimated and compared (**Tables 1-4**), the peaks can similarly be found for the CuTPP samples with the removal of the Co 2p peak and the addition of the Cu 2p ca. 932 eV.

Table 1. Elemental contents (at%) of the CuTPP series from XPS measurements

Peak		CuTPP	CuTPP-200	CuTPP-300	CuTPP-400
C 1s	C=C	20.62	41.84	43.93	48.99
	C-C	35.6	38.68	34.98	32.91
	C-N/O	14.3	3	3.4	3.02
	C=N/O	8.88	3.25	1.13	3.27
	Total C	79.4	86.77	83.44	88.19
N 1s	N-Cu	2.28	4.77	3.3	3.93
	Pyrrolic	2.13	0.37	0.25	0.33
	Total N	4.41	5.14	3.55	4.26
O 1s	C=O	10.66	5.97	10.71	5.52
	C-O	4.7	0.75	1.4	1.39
	Total O	15.36	6.72	12.11	6.91
Cu		4.85	3.81	3.94	6.36

Table 2. Elemental contents (at%) of the CoTPP series from XPS measurements

Peak		CoTPP	CoTPP-150	CoTPP-200	CoTPP-300
C 1s	C=C	31.23	22.28	37.36	31.23
	C-C	46.94	31.86	25.33	18.06
	C-N/O	7.74	10.42	13.1	14.71
	C=N/O	2.25	11.86	x	x
	Total C	88.16	76.42	75.79	64
N 1s	N-Cu	1.79	6.87	7.31	4.39
	Pyrrolic	2.28	0.48	0.57	0.45
	Total N	4.07	7.35	7.88	4.84
O 1s	C=O	4.48	9.67	2.16	9.39
	C-O	2.42	4.92	12.19	20.7
	Total O	9.18	15.07	14.92	30.54
Co 2p	Co^{3+}	0.76	0.9	0.89	0.55
	Co^{2+}	0.19	0.82	1.07	0.48
	Total Co	0.95	1.72	1.96	1.03

Table 3. Binding energies (eV) of all elements of the CuTPP series from XPS measurements

Peak		CuTPP	CuTPP-200	CuTPP-300	CuTPP-400
C 1s	C=C	284.07	284.28	284.21	284.27
	C-C	284.80	284.80	284.80	284.80
	C-N/O	285.94	287.24	286.54	287.20
	C=N/O	287.96	291.30	291.08	291.26
N 1s	N-Cu	397.76	397.72	397.85	397.72
	Pyrrolic	399.00	400.74	400.90	400.71
O 1s	C=O	531.47	531.47	531.63	531.46
	C-O	532.80	532.53	533.25	532.02
Cu 2p	Cu^{2+} $2p_{3/2}$	934.01	934.09	934.20	934.03
	Satilite	940.60	940.57	940.77	940.12
	Satilite	943.52	943.09	943.64	943.43
	Cu^{2+} $2p_{3/2}$	953.80	953.92	953.99	953.77
	Satilite	961.77	962.17	962.43	962.46

Table 4. Binding energies (eV) of all elemental components of the CoTPP series from XPS measurements

Peak		CoTPP	CoTPP-150	CoTPP-200	CoTPP-300
C 1s	C=C	284.22	284.08	284.13	284.10
	C-C	284.80	284.80	284.80	284.80
	C-N/O	286.29	285.71	286.96	286.97
	C=N/O	291.27	287.76	x	x
N 1s	N-Cu	397.60	397.79	397.80	397.80
	Pyrrolic	398.90	400.43	400.76	400.85
O 1s	C=O	531.66	531.36	531.32	531.28
	C-O	532.95	533.18	532.84	532.28
Co 2p	Co^{3+} $2p_{3/2}$	779.36	779.76	779.67	779.71
	$Co2^{+}$ $2p_{3/2}$	781.45	782.12	781.87	782.07
	Satilite	787.92	785.36	785.67	785.18
	Satilite	X	788.73	789.06	787.98
	Co^{3+} $2p_{3/2}$	794.59	795.19	795.17	795.50
	$Co2^{+}$ $2p_{3/2}$	795.38	797.33	797.56	797.45
	Satilite	803.38	801.15	801.46	800.97
	Satilite	X	803.88	803.87	803.77

From **Figure 3**, one can see the gradual increase in sp2 carbon:sp3 carbon in the CoTPP series, with a trend of and CoTPP-300 = 1.73:1 > CoTPP-200 = 1.47:1 > CoTPP-150 = 0.70:1 > CoTPP = 0.66:1, with a similar trend seen in the CuTPP samples. This indicates a relative increase in graphitization and the more electrically conductive C=C sp2 bonding and a removal of previously unreacted carbon ligands.[36]

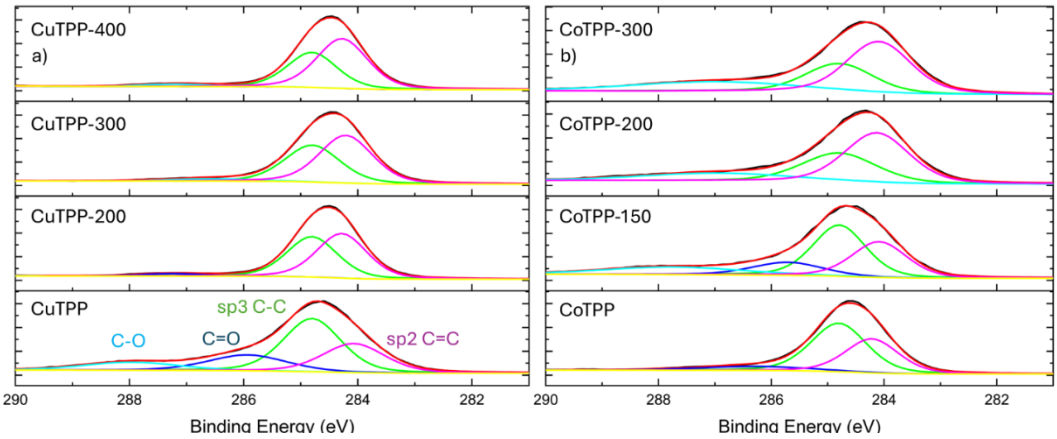

Figure 3. XPS C 1s Spectra of the (a) CuTTP and (b) CoTPP sample series.

In **Figure 4** the N-Cu and N-Pyrrolic peaks can be seen for all samples at 397.8 eV and 399.0 eV respectively, before heating, with a noticeable decrease in the pyrrolic peak after heating.

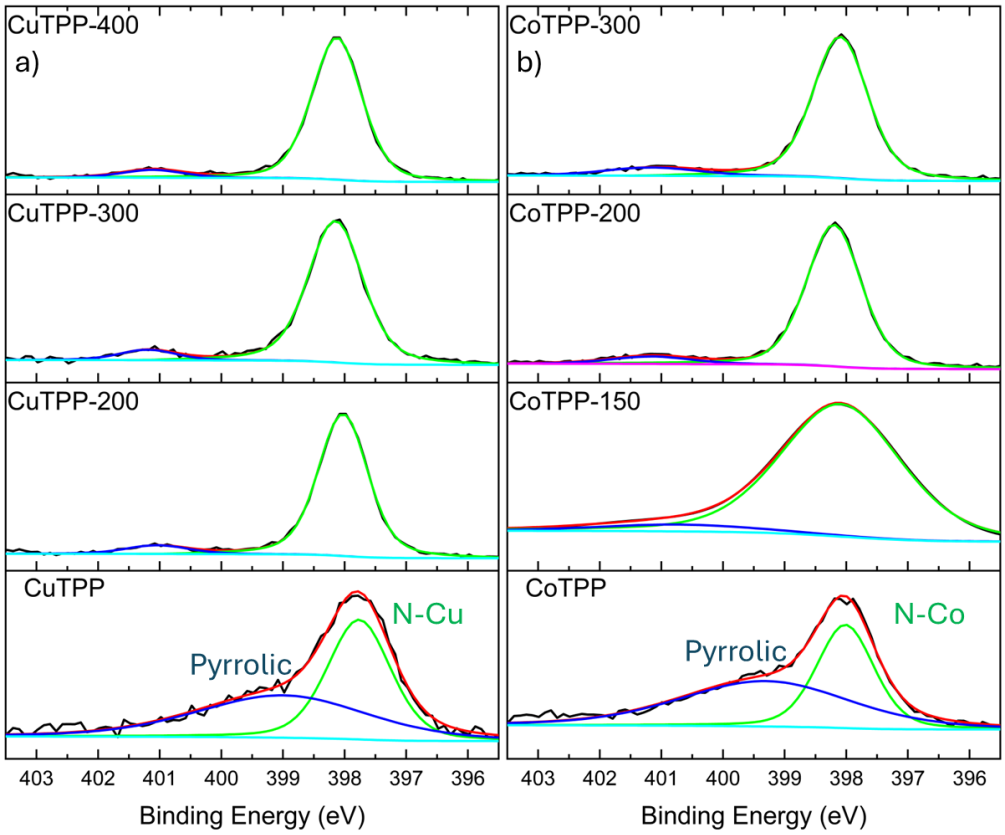

Figure 4. XPS N 1s Spectra of the (a) CuTTP and (b) CoTPP sample series.

Indicating the removal of unbound nitrogen ligands. In O1s of **Figure 5,** there is no peak at 529-530 eV confirming that there was no metal oxide formation during the heating process.[37]

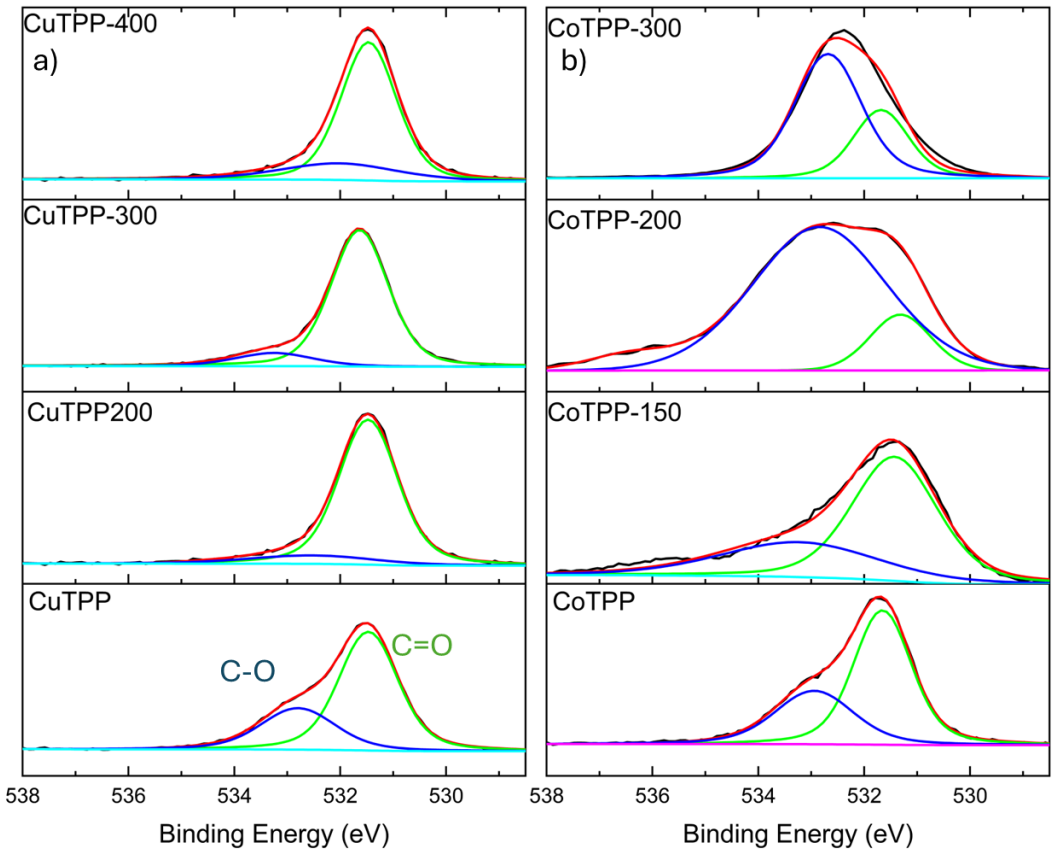

Figure 5. XPS O 1s Spectra of the (a) CuTTP and (b) CoTPP sample series.

Figure 6a shows the corresponding Co 2p spectra of the CoTPP series. The CoTPP precursor can be seen to possess a doublet at 779.4/794.2 eV due to the $2p_{3/2}/2p_{1/2}$ electrons that can be further split into Co^{3+}/Co^{2+} at 779.4/781.5 eV and 794.6/795.4 eV.[24, 38] Similar peaks can be seen in the heated samples with the noticeable increase

in the amount of Co^{2+} and their corresponding shoulders at 785.4 eV/803.8 eV.

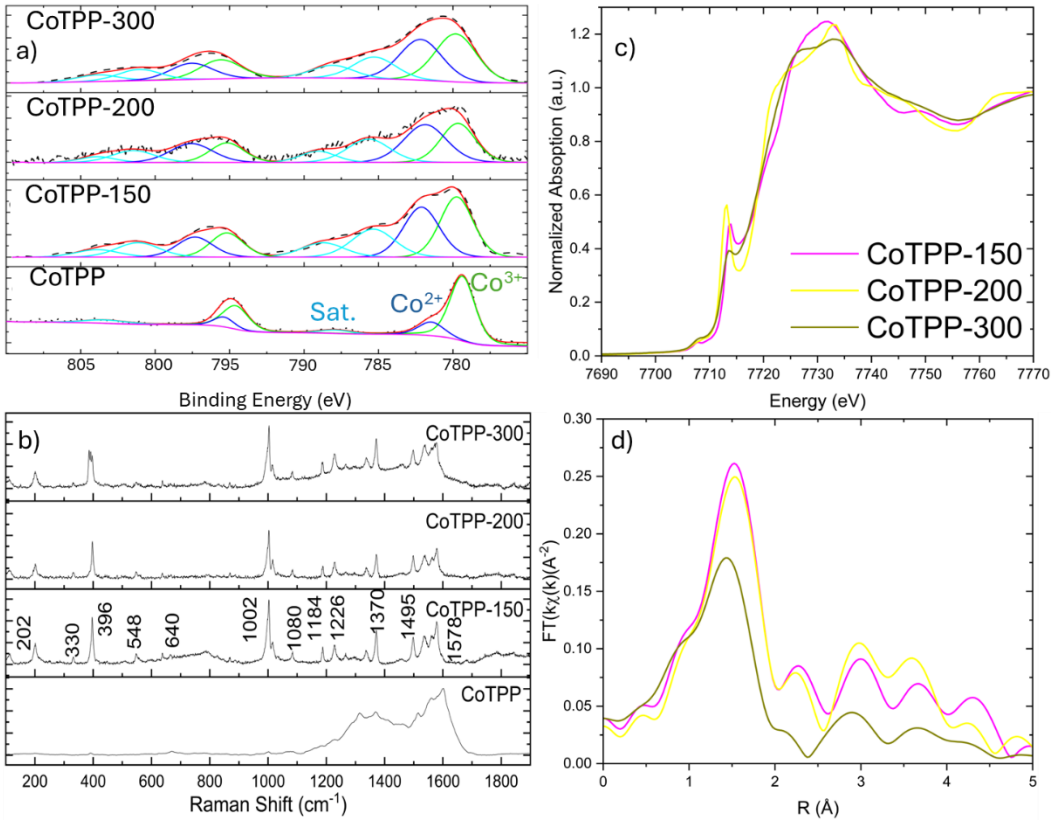

Figure 6. (a) High-resolution XPS scans of Co 2p of the CoTPP samples. Black curves are experimental data, and colored curves are deconvolution fits. (b) Raman spectra of the CoTPP samples. (c) X-ray absorption near-edge spectra (XANES) of Co K and (d) corresponding Fourier transformed extended X-ray absorption spectra (FT-EXAFS) of CoTPP samples

This increase in Co^{2+} of CoTPP-200 > CoTPP-300 > CoTPP-150 CoTPP aligns with the increase in $2e^-$ ORR activity which aligns well with previous studies which have highlighted the $Co^{2+}N_4$ is more active towards $2e^-$ while the $Co^{3+}N_4$ can be active towards $4e^-$.[39, 40] Furthermore, the most active sample of CoTPP-200 also exhibited the

N/Co ratio closest to the ideal of 4, with CoTPP = 4.28, CoTPP-150 = 4.27, CoTPP-200 = 4.02, and CoTPP-300 = 4.70. The increased coordination number in CoTPP and CoTPP-150 can be attributed to additional axial ligand binding. Unlike the CuTPP where a coordination number greater than 4 requires significant modifications, CoTPP can readily bind ligands in the axial position leading to an increased coordination number.[41] However, the CoN_4 has been highlighted as more favorable for the $2e^-$ ORR.[42] Furthermore the sharp increase in coordination number of CoTPP-300 can be attributed to the loss of total cobalt going from CoTPP-200 = 1.96% to CoTPP-300 = 1.03%, indicating that overheating begins to damage the ring and remove the metal center. **Figure 7** shows the corresponding Cu 2p spectra of the CuTPP series where a dominate doublet at 934.0/953.8 eV due to the $2p_{3/2}/2p_{1/2}$ electrons of Cu^{2+} can be seen with the corresponding Cu^{2+} satellites can be found at ca. 943.0 and 962.8 eV, however no clear Cu^0 or Cu^{1+} peak can be seen ca. 932 or 952 eV.[17] Showing the original Cu^{2+} oxidation state was maintained and confirmed the heating did not cause oxidation. Additionally, the heating improved the N/Cu ratio to be closer to 4. CuTPP = 4.85, CuTPP-200 = 3.81, CuTPP-300 = 3.94 and CuTPP-400 = 6.36. This aligns well with what was seen in the CoTPP series, where the unreacted ligands being removed after heating improving the ratio but too much heating damages the bonds. Again with the maintenance of the CuN_4 lines up with the observed ORR activity with CuTPP-300 > CuTPP-200 > CuTPP-400 > CuTPP.

Overall, both sample series XPS indicate that heating will increase the graphitization of the material leading to a more conductive sample, along with the heating helping to clear the active site for optimized ORR activity but excessive heating can lead to degradation of the MN_4 active site.

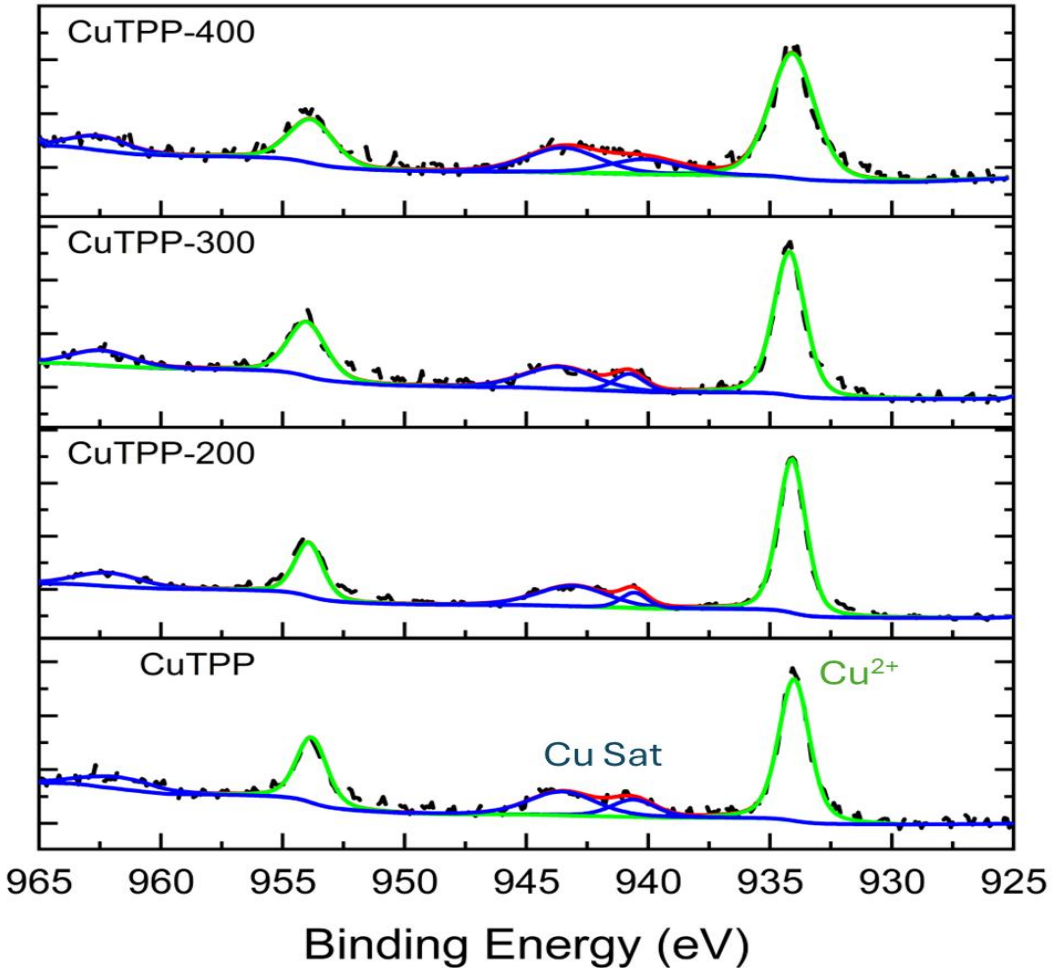

Figure 7. High-resolution XPS scans of Cu 2p of the CuTPP samples. Black curves are experimental data, and colored curves are deconvolution fits.

Further structural insights were obtained from Raman measurements. From **Figure 6b**, the CoTPP precursor can be seen to exhibit a noisy signal likely coming from leftover ligands that are removed after heating and washing as in all of the treated samples a series of organic signals seen at $\delta(C_bEt)$ and $\delta(C_aNC_a)$ at 1002 cm^{-1},[26] C-C=C aromatic 1184 cm^{-1},[43] $\delta(C_aH)$ and $\delta(C_mH)$ 1226 cm^{-1},[44] C-N-C symmetric vibration at 1370 cm^{-1},[45] and C-C=C aromatic 1578 cm^{-1}.[43] Along with Co-N signals at Co-N bending 202 cm^{-1}, 330 cm^{-1} and 396 cm^{-1} Co-N symmetric stretching and Co-N bending 640 cm^{-1}.[26, 46] With only minor shifts in peak position between spectra except for the the 330 cm^{-1} peak decreases in intensity until it almost disappears and the 396 cm^{-1} peak broadens noticeably and splinters into 3 overlapping peaks. Both of these indicate that the heating has a significant effect on the CoN_4 structure which aligns with the greater deterioration of $2e^-$ ORR activity scene in CoTPP-300 and shifts in N/Co ratio seen in the XPS.

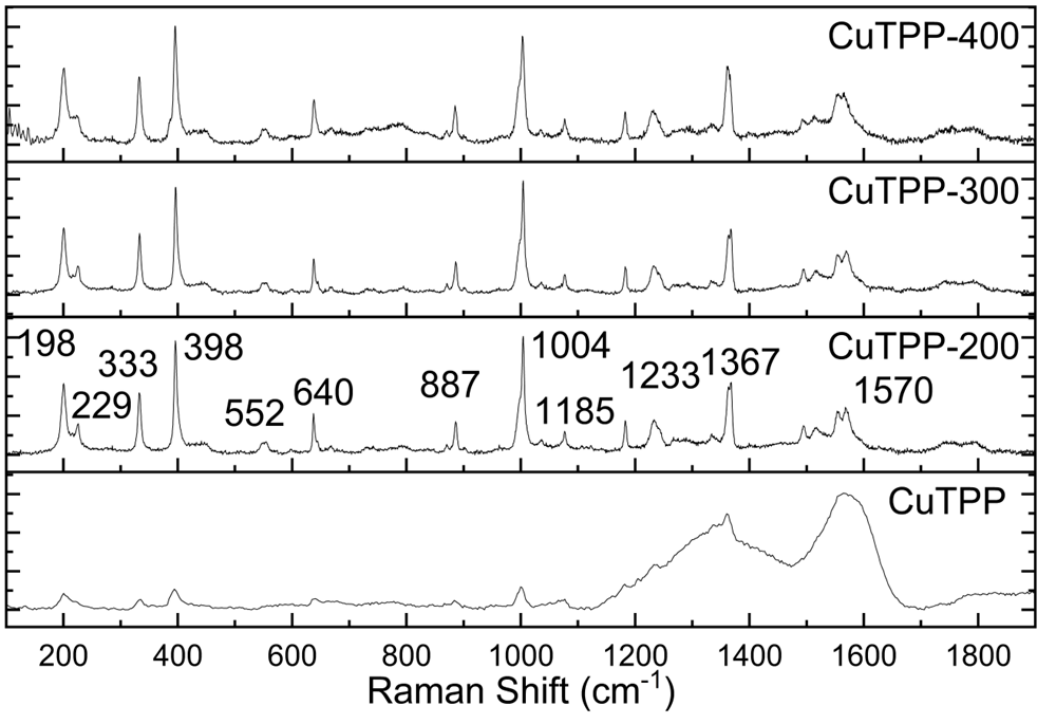

Figure 8. Raman spectra of the CuTPP samples.

The CuTPP samples (**Figure 8**) follow a similar trend with peaks becoming more defined after heating. With similar peak positions throughout shifted slightly, as would be expected with a different metal center. Further confirming the production of the CuN_4 structure. Furthermore D and G bands, and the ratio of the band intensity can be seen to increase with heating in both samples from CuTPP = 0.82 to CuTPP-200 = 1.48 to CuTPP-300 = 1.49 to CuTPP-400 = 1.52 and CoTPP = 0.66 to CuTPP-150 = 0.77 to CoTPP-200 = 0.81 to CoTPP-300 = 1.08, suggestive of the formation of an increasingly defective carbon scaffold in both samples. This was in good alignment with the N:Cu ratio obtained in XPS measurements due to partial retention of the metal-N_4 coordination moiety. Further structural insights were obtained from XAS measurements. From the Co K-edge X-ray absorption near edge structure (XANES)

In **Figure 6c** all CoTPP sample show a similar transition of 7714 eV 1s →4p indicating D_{4h} symmetry found in square planar geometry.[47] Notably this peak is greatly diminished in the CoTPP-300 sample indicating damage to the ring inhibiting the 1s →4p transition.[48] Similarly for the Cu K-edge profiles in **Figure 9a**, all CuTPP samples display a strong peak at 8985 eV that is typical of Cu^{2+} specifically of a 1s→$4p_{xy}$ electron transition indicative of square planar geometry.[49]

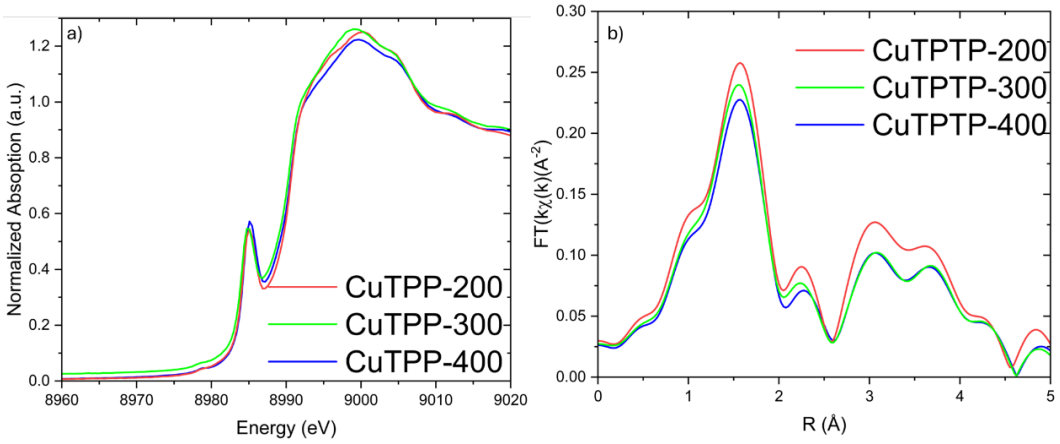

Figure 9. a) X-ray absorption near-edge spectra (XANES) of Cu K and corresponding b) Fourier transformed extended X-ray absorption spectra (FT-EXAFS) of CuTPP samples

There is comparatively little shift in this peak compared to the 7714 eV signal supporting that the CoN_4 structure is more thermally responsive than the CuN_4 structure. Notably, the Cu^+ peak that is typically seen at 8982 eV for Cu^+ chelated to nitrogen ligands is absent in all samples.[49, 50] In the corresponding Fourier-transformed extended X-ray absorption fine structures (FT-EXAFS) are shown in **Figure 6d**, all CoTPP samples can be seen to exhibit a dominate peak at 1.5 Å,

corresponding to the known length of the Co-N path.[42, 51] Furthermore, the fitting of these peaks (**Table 5, Figure 10**) series there were significant shifts with CoTPP-150 having an effective pair distance of 1.90 Å and CN of 4.3, CoTPP-200 having and effective pair distance of 1.91 Å and CN of 4.0 and CoTPP-300 having an effective pair distance of 1.88 and CN of 3.7.

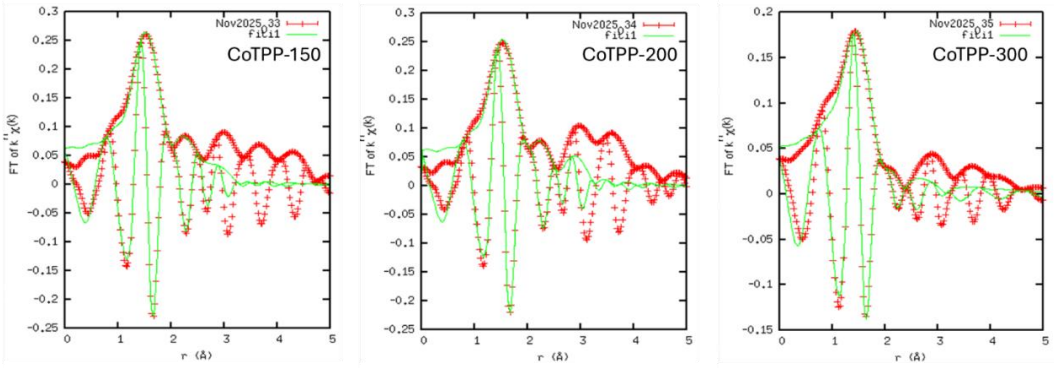

Figure 10. Fitting results of the Co K-edge EXAFS of the CoTPP sample series.

Table 5. Fitting results of the Co K edge XAS spectra of the samples series

Samples	Peak	Effective Pair Distance (Å)	σ^2	CN
CoTPP-150	Cu-N	1.901	0.004	4.343
	Co-C 2nd shell	2.689	0.011	8.274
CoTPP-200	Cu-N	1.910	0.004	4.023
	Co-C 2nd shell	2.609	0.008	18.312
CoTPP-300	Cu-N	1.880	0.004	3.730
	Co-C 2nd shell	2.624	0.008	22.232

Again, this aligns with the previous XPS and ORR activity indicating some axial ligand binding in the CoTPP-150 sample that is removed in CoTPP-200 followed by minimal damage to the ring structure in CoTPP-300. Furthermore the 2nd shell defects can be seen in the CoTPP series as well, where the coordination number went from CoTPP-150 = 8.3 very close to the ideal of 8 to CoTPP-200 = 18.3 and CoTPP-300 = 22.2. This along with the EXAFS data becoming smoother with the higher heating indicates a more disordered environment which is in good agreement with the D/G ratio from the Raman measurements. Additionally, all CuTPP (**Figure 9b**) samples can be seen to exhibit a similar though more consistent profile, with a dominant EXAFS peak at ca. 1.6 Å for the Cu-N path.[50]

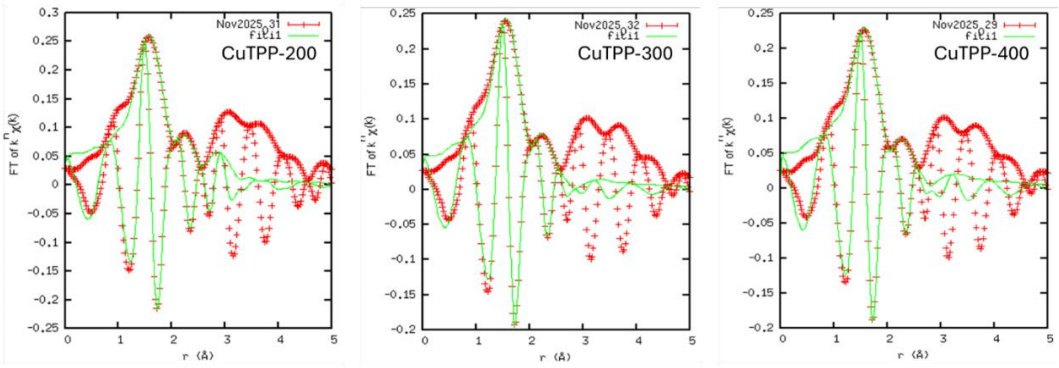

Figure 11. Fitting results of the Cu K-edge EXAFS of the CuTPP sample series

Table 6. Fitting results of the Cu K edge XAS spectra of the samples series

Samples	Peak	Effective Pair Distance (Å)	σ^2	CN
CuTPP-200	Cu-N	1.953	0.004	4.002
	Cu-C 2nd shell	2.521	0.010	9.123
CuTPP-300	Cu-N	1.952	0.003	4.001
	Cu-C 2nd shell	2.470	0.006	17.228
CuTPP-400	Cu-N	1.951	0.005	3.999
	Cu-C 2nd shell	2.624	0.007	11.431

Furthermore, fitting of these peaks (**Table 6, Figure 11**) yields a coordination number (CN) of 4 and an effective pair distance of 1.95 Å for all the CuTPP samples**,** for these first shell fittings the effective pair distance is also the bond length giving us a bond length of 1.95 Å for the primary Cu-N bond.

This further confirms that the CuN_4 structure was retained during MIH treatment thanks largely to the rapid heating. Additionally in the 2nd shell Cu-C interaction the increased graphitization can be observed, CuTPP-200 has a CN of 9.1 close to the ideal of 8, while CuTPP-300 increases to 17.2 and CuTPP-400 to 11.4. This indicates significant shifts in the outer carbon shells while maintaining the core CuN_4 structure. Overall, results from the XAS measurements further confirmed that the CoN_4 structure was enhanced by the MIH treatment, while the CuN_4 moiety was retained by it, along with the outside carbon shells became increasingly defective. Additionally, excessive heating can cause damage to the metal-N4 structure as shown by CoTPP-300. With this we can conclude it was the unique metal-N_4 SAC structure that was responsible for the remarkable $2e^-$ ORR activity (**Figure 12**) in both CuTPP-300 and CoTPP-200.

3.3.2 Electrocatalytic activity

The electrocatalytic activity of the MTPP samples were evaluated with a rotating ring-disk electrode (RRDE) in 0.1 M KOH. From the polarization curves in **Figure 12a-b**, all samples can be seen to exhibit an apparent electrocatalytic activity towards ORR, where nonzero voltametric currents started to appear as the disk potential was swept negatively. Yet the activity varied markedly among the series.

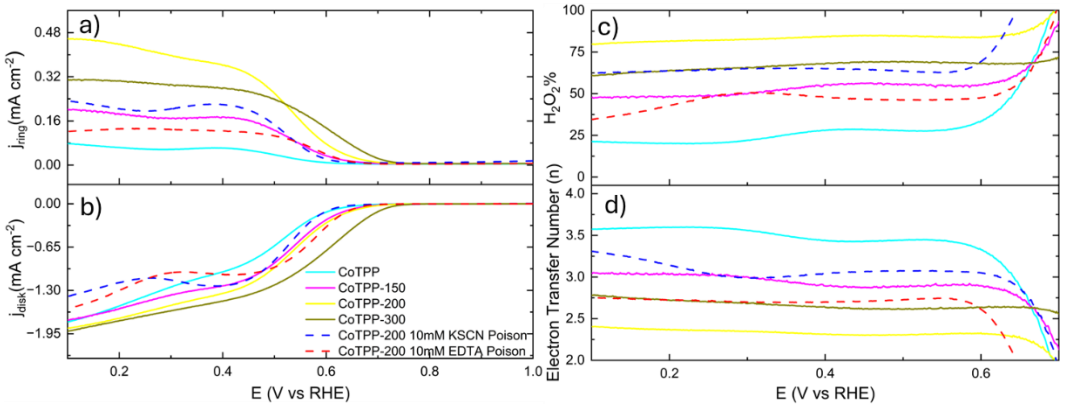

Figure 12. (a) RRDE ring and (b) disk voltammograms of CoTPP prepared at different MIH currents in oxygen-saturated 0.1 M KOH at the potential sweep rate of 10 mV s^{-1} and rotation rate of 1600 rpm. (c) The corresponding H_2O_2 yield and (d) electron transfer number (*n*) at different electrode potentials before (solid lines) and after (dashed lines) exposure to 10 mM metal poisoning agents

Specifically, the onset potential, which was defined as the potential to reach the disk current density of 0.1 mA cm^{-2}, decreased in the order of CoTPP-300 (+0.71 V) > CoTPP-200 (+0.65 V) > CoTPP-150 (+0.64 V) > CoTPP (+0.61 V), and then the CuTPP samples showed a similar trend where (**Figure 13**) CuTPP-400 (+0.64 V) > CuTPP-300 (+0.63 V) > CuTPP-200 (+0.62 V) > CuTPP (+0.60 V). These onset potentials were remarkably close to the formal potential of +0.70 V for $2e^-$ ORR.[52]

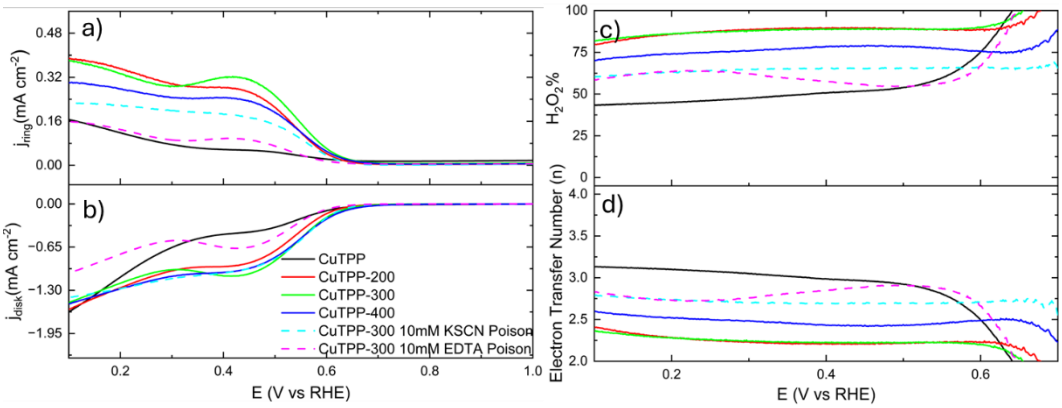

Figure 13. (a) RRDE ring and (b) disk voltammograms of CuTPP prepared at different MIH currents in oxygen-saturated 0.1 M KOH at the potential sweep rate of 10 mV s^{-1} and rotation rate of 1600 rpm. (c) The corresponding H_2O_2 yield and (d) electron transfer number (*n*) at different electrode potentials before (solid lines) and after (dashed lines) exposure to 10 mM metal poisoning agents

This trend indicates CoTPP has a higher intrinsic activity than CuTPP and the higher heating caused a greater graphitization of the material allowing for easier electron current flow. A different trend can be seen with the collection current at the ring electrode, here when comparing currents at +0.46V the trend is CoTPP-200 (0.32 mA cm^{-2}) > CuTPP-300 (0.30 mA cm^{-2}) > CoTPP-300 (0.26 mA cm^{-2}) > CuTPP-200 (0.26 mA cm^{-2}) > CuTPP-400 (0.23 mA cm^{-2}) > CoTPP-150 (0.16 mA cm^{-2}) > CuTPP (0.06 mA cm^{-2}) > CoTPP (0.05 mA cm^{-2}). The difference in these trends can be explained by the selectivity (**Figure 12c,d**) where the electron transfer number and H_2O_2 production % follow the same trend, where CuTPP-200 (2.21, 90%) > CuTPP-300 (2.22, 89%) > CoTPP-200 (2.30, 85%) > CuTPP-400 (2.42, 79%) > CoTPP-300 (2.62, 69%) > CoTPP-150 (2.87, 56%) > CuTPP (2.96, 52%) > CoTPP (3.43, 28%). Here we can see

that the higher disk current that can be seen in the higher heating of CoTPP-300 and CuTPP-400 are due to H_2O production from low selectivity, which is supported by the CoTPP-300 onset being higher than the theoretical most positive value of +0.71V. This also suggests that the optimal induction currents for sample preparation are 200A for CoTPP and 300A CuTPP. This difference in heating aligns with known features of the corresponding M-N_4 sites in their respective tetraphenyl porphyrins, where CuTPP has a consistent coordination number of 4 coming only from the nitrogen and metal oxidation state of Cu^{2+}.[53] While CoTPP can regularly have a coordination number of 4 or 5 due to increased axial binding of ligands from Co^{3+} vs Co^{2+},[54] leading to greater thermal sensitivity of the CoN_4 site vs the CuN_4 site. To unravel the catalytic active site, metal poisoning tests were conducted using KSCN and EDTA. The former is known to adsorb strongly onto metal sites whereas the latter is prone to chelation with single metal centers, where the blocking leads to apparent diminishment of the catalytic activity.[55] Experimentally, when KSCN or EDTA (10 mM) was added into the 0.1 M KOH electrolyte (**Figure 12a-b**), RRDE tests showed that the onset potential shifted negatively for CuTPP-300 to +0.59 V for EDTA and +0.63 V for KSCN, and for CoTPP-200 it shifted to +0.65 V for EDTA and +0.60 V for KSCN. This was accompanied by a decrease of the disk current for CuTPP-300 to -0.63 mA cm^{-2} for EDTA and -0.95 mA cm^{-2} for KSCN at +0.46 V and for CoTPP-200 it shifted to -1.09 mA cm^{-2} for EDTA and -1.04 for KSCN at +0.46 V. Indicating that the ORR activity was primarily due to the metal sites which could be effectively poisoned by the chelating agents. An even more significant change can be seen in the ring current at

+0.46V, which decreased for CuTPP-300 to 0.09 mA cm^{-2} for EDTA and 0.17 mA cm^{-2} KSCN and for CoTPP-200 to 0.12 mA cm^{-2} for EDTA and 0.19 mA cm^{-2} KSCN. In fact, the H_2O_2 yield (**Figure 12c**) diminished markedly to only 55% for EDTA and 66% for KSCN in CuTPP-300 and 64% for EDTA and 47% for KSCN in CoTPP-200. The fact that a similar poisoning effect was observed with KSCN and EDTA further suggests that the ORR active sites were the metal centers atomically dispersed within the carbon matrix (*vide infra*).

3.3.3 Disinfection applications

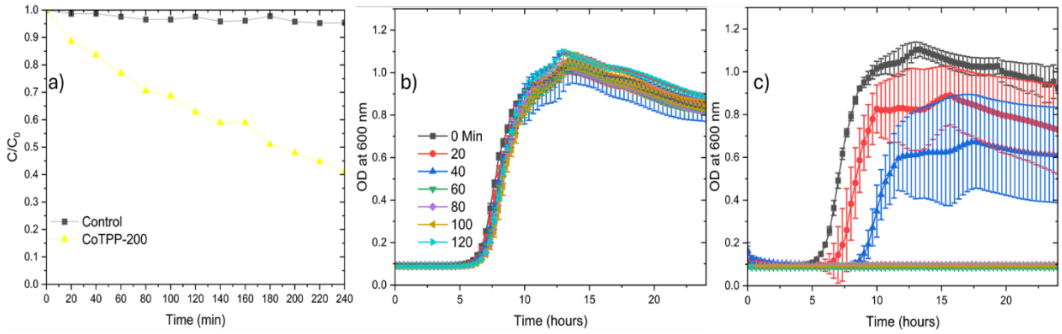

Figure 14. (a) Methylene blue degradation by CuNC-400 at +0.46 V for 240 min in 0.1 M KOH, in comparison to the blank control with a bare electrode. **(**b) *E. coli* control of electrochemical disinfection with a base electrode over 2 h (c) electrochemical disinfection using CoTPP-200 over 2 h

The selective and abundant production of H_2O_2 can be exploited for on-site applications, namely the degradation of organic dyes and disinfection of water. For the organic dye degradation, a 25 mg L^{-1} solution of MB in 0.5 M Na_2SO_4 was prepared and 75 mL was added into an electrochemical cell where the working electrode was

held at a potential of +0.46 V. From **Figure 14a**, one can see that CoTPP-200 removed 58.9% of the dye after 240 minutes of electrochemical treatment. By contrast, for a bare electrode, less than 5% of MB was removed under the same experimental conditions. While the CuTPP-300 (**Figure 15**) was able to degrade 53.7% of the dye.

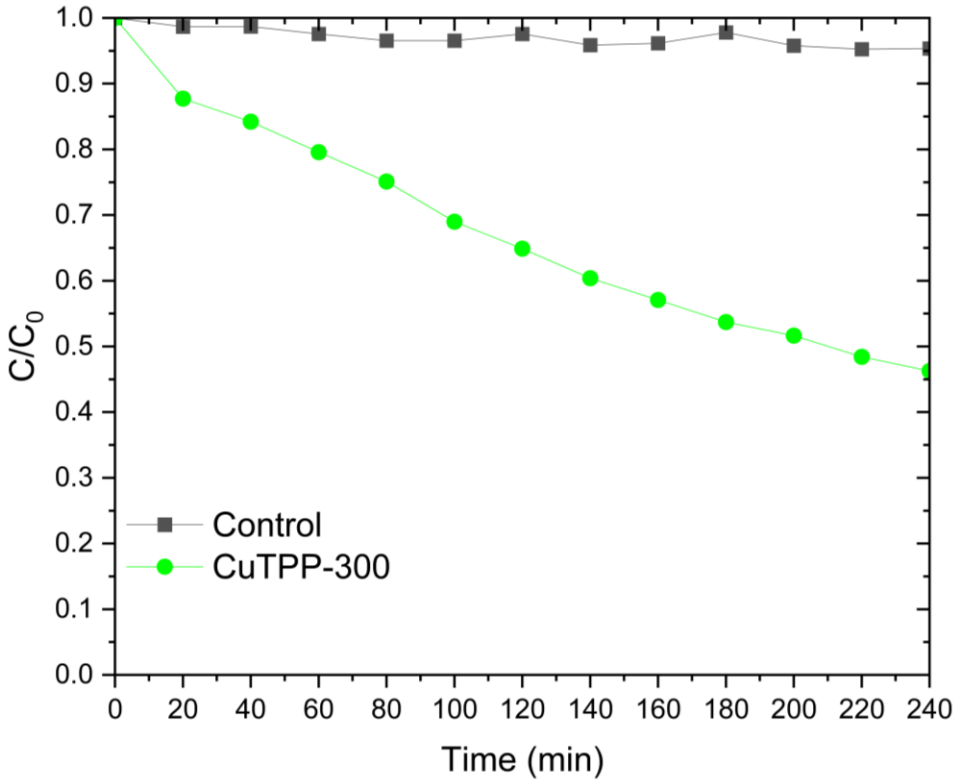

Figure 15. Methylene blue degradation by CuNC-400 at +0.46 V for 240 min in 0.1 M KOH, in comparison to the blank control with a bare electrode.

Such a unique property could also be exploited for electrochemical disinfection of water. From **Figure 14b**, for the control experiment with a bare electrode (where the potential was held at +0.46 V), the *E. coli* cells exhibited a rather consistent growth curve with a lag phase of ca. 5.7 h and a final lag phase delay of 0.7 h after 120 minutes

of exposure. Yet the bacterial growth was markedly inhibited with a CoTPP-200 modified electrode (**Figure 14c**), where the lag phase, which is the flat portion seen before the growth phase, can be seen to delay 3.4 h after 40 minutes of expose and complete inhibition after just 60 minutes of exposure.

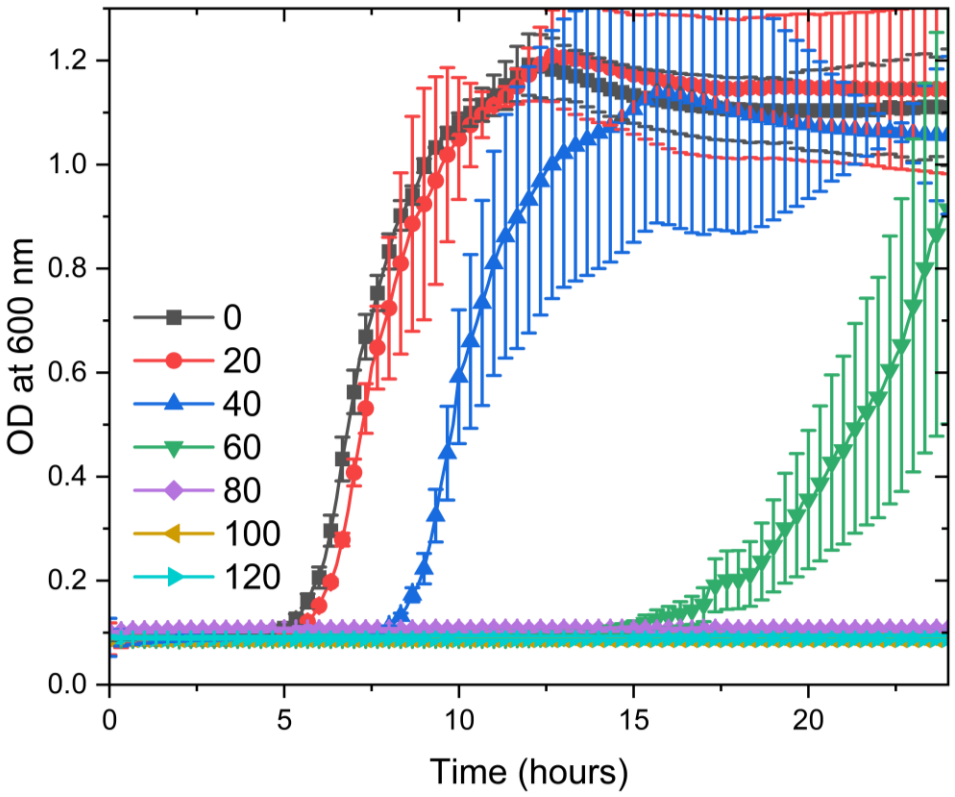

Figure 16. Electrochemical disinfection of *E. coli* using CuTPP-200 over 2 h

While the CuTPP-300 (**Figure 16**) can be seen to delay 3.1 h after 40 min of electrochemical treatment, then to 9.7 h after 60 min and full inhibition after 80 min. This slightly higher inhibitory activity seen in CoTPP-200 is in line with its greater ring potential during seen in **Figure 12**.

3.4. Experimental Section

3.4.1 Chemicals

Ethylenediaminetetraacetic acid (EDTA, ≥99.0%, Aldrich), potassium thiocyanate (KSCN, 99.0%, Aldrich), nitric acid (HNO_3, Aldrich), potassium hydroxide (KOH, Fisher Chemicals), Nafion®117 solution (5% in a mixture of lower aliphatic alcohols and water, Aldrich), and methylene blue hydrate (MB, Acros Organics) were all used as received. Water was purified with a Barnstead Nanopure Water System (resistivity 18.3 MΩ cm)

3.4.2 MTTP Synthesis

Tetraphenyl porphyrin and MCl_2 (M=Co or Cu) at a 1:1 molar ratio were dispersed into DMF, and solution was refluxed for 30 min before the addition of water to separate the products, which were collected via vacuum filtration then washed with water again. The solid produced was eluted with DCM and dried under a vacuum. MTTP product was then purified via column chromatography using hexanes and DCM and dried again.

3.4.3 MTPP-X Synthesis

The MIH setup was described previously.[32, 33] In a typical experiment, 20 mg of MTPP was mixed with 400 mg of NaCl in 1 mL of THF. The solution was sonicated for 5 min, heated under magnetic stirring at 40 C until the liquid had evaporated, and then placed in vacuum overnight to ensure solvent removal. The obtained solid was placed onto an iron sheet lined with graphitic paper in a glass tube that had been purged with Ar gas and subject to MIH treatment at controlled induction currents (X = 150-400 A) for 10 s. After heating, the samples were washed with water, ethanol, acetone and THF

until a clear supernatant was produced, and the solids were dried under a vacuum overnight. The samples were then subject to acid leaching to remove metal oxides whereby 10 mg of the sample were dispersed in 10 mL of 1.0 M HNO_3 under magnetic stirring at room temperature for 3 h, followed by rinsing with a copious amount of Nanopure water and a final drying. The resultant samples were denoted as MTPP-X.

3.4.4 Characterization

X-ray photoelectron spectroscopy (XPS) measurements were carried out with a Thermo Fisher K-alpha system, where the binding energy was calibrated against the C 1s binding energy. Raman measurements were conducted using a Horiba Jobin Yvon Lab-RAM ARAMIS automated scanning confocal Raman microscope under 532 nm excitation. XAS measurements were conducted at the temperature of 10 K using an Oxford liquid helium cryostat at beamline 4–1 of the Stanford Synchrotron Radiation Light source. The obtained XAS data were reduced, fitted, and analyzed with the RSXAP software.[34] The Fourier Transform range was 3.5–11.5 and the fit range was 1.2-2.6. The theoretical functions for the simulated structure and each path were calculated by WebAtoms.[35]

3.4.5 Electrochemistry

Electrochemical performance was examined with a CHI 710 electrochemical workstation in a three-electrode configuration using a Hg/HgO reference electrode, a graphite rod counter electrode, and a gold ring-glassy carbon disk working electrode (disk surface area 0.246 cm^2). The reference electrode was calibrated against a

reversible hydrogen electrode (RHE), and all potentials in the present study were referenced to the RHE. The catalyst inks were prepared by dispersing 2 mg of the samples prepared above into a mixed solution containing 300 μL of ethanol, 700 μL of H_2O, and 10 μL of Nafion under sonication for 30 min. Then 10 μL of the inks were dropcast onto the glassy carbon disk electrode surface and dried naturally at room temperature before being coated with 3 μL of 20 wt % Nafion. The catalyst loading was 0.204 mg cm^{-2}.

3.4.6 Methylene blue degradation

MB degradation was performed using the three-electrode setup described above, with the addition of 25 mg L^{-1} MB in the 0.1 M KOH supporting electrolyte. The electrode potential was held at +0.46 V and the absorbance of the electrolyte solution was monitored at different time points with a UV-vis spectrometer. A control experiment was conducted with the same setup but with no catalyst deposited onto the working electrode.

3.4.7 Electrochemical disinfection of water

Escherichia coli (*E. coli*) cells were grown in Luria−Bertani (LB) agar in a 37 °C incubator. A single colony was selected and used to inoculate 3 mL of LB broth and allowed to shake at 37 °C for 18 h. The resulting liquid was centrifuged at 5000 rpm for 5 min and resuspended in phosphate buffered saline (PBS) 3 times before being diluted to an optical density (OD) of 0.1 at 600 nm. Then 1 mL of the spiked PBS solution was diluted into 99 mL of sterile 0.5 M Na_2SO_4. 75 mL of this solution was

poured into the electrochemical cell, and the working electrode was held at the potential of 0.1 V for 1 h, with 10 mL aliquots removed every 20 min and pipetted into a 96-well plate along with 200 mL of sterile LB broth. The 96-well plate was placed in a Molecular Device VERSA max microplate reader, where the OD was measured at 600 nm every 10 min with intermittent shaking between each reading over a 24 h, 37 °C incubation period.

3.5. Conclusions

In this study tetraphenyl porphyrin was modified using MIH to form Cu-N-C and Co-N-C catalysts for the 2e- ORR to H_2O_2. This heating method allowed for the formation of defective carbon supporting material while maintaining the core porphyrin meatl-N_4 motif allowing for the formation of SACs. The sample with the highest activity was the CuTPP-300 and CoTPP-200 which showed high selectivity to hydrogen peroxide production, and effective in direct application ability of organic dye degradation and electrochemical disinfection of *E.* coli cells in water. The results of this study show the ability of MIH to make controlled modifications to carbon structures that can be used for further catalyst development.

3.6 References

(1) Zhao, E.; Xue, W.; Qin, S.; Guo, Y.; Xin, X.; Wang, H.; Zhang, Y.; Zuo, S. A review of H2O2 electrosynthesis by 2-electron ORR and 2-electron WOR: From catalysts to electrochemical cells. *Coordination Chemistry Reviews* **2025**, *545*, 217042.

(2) Chang, Q.; Zhang, P.; Mostaghimi, A. H. B.; Zhao, X.; Denny, S. R.; Lee, J. H.; Gao, H.; Zhang, Y.; Xin, H. L.; Siahrostami, S. Promoting H2O2 production via 2-electron oxygen reduction by coordinating partially oxidized Pd with defect carbon. *Nature communications* **2020**, *11* (1), 2178.

(3) Hu, Y.; Zhang, J.; Shen, T.; Li, Z.; Chen, K.; Lu, Y.; Zhang, J.; Wang, D. Efficient electrochemical production of H2O2 on hollow N-doped carbon nanospheres with abundant micropores. *ACS Applied Materials & Interfaces* **2021**, *13* (25), 29551-29557.

(4) Tang, J.; Zhao, T.; Solanki, D.; Miao, X.; Zhou, W.; Hu, S. Selective hydrogen peroxide conversion tailored by surface, interface, and device engineering. *Joule* **2021**, *5* (6), 1432-1461.

(5) Wen, Y.; Zhang, T.; Wang, J.; Pan, Z.; Wang, T.; Yamashita, H.; Qian, X.; Zhao, Y. Electrochemical reactors for continuous decentralized H2O2 production. *Angewandte Chemie* **2022**, *134* (35), e202205972.

(6) Perry, S. C.; Mavrikis, S.; Wang, L.; de León, C. P. Future perspectives for the advancement of electrochemical hydrogen peroxide production. *Current Opinion in Electrochemistry* **2021**, *30*, 100792.

(7) Guo, J.; Li, K.; Liang, J.; Ying, D.; Song, X.; He, Y.; Jia, J. High-quality hydrogen peroxide production through electrochemical reduction of anthraquinone in ambient environment. *Science Advances* **2026**, *12* (9), eady6378.

(8) Jing, L.; Wang, W.; Tian, Q.; Kong, Y.; Ye, X.; Yang, H.; Hu, Q.; He, C. Efficient neutral H2O2 electrosynthesis from favorable reaction microenvironments via porous carbon carrier engineering. *Angewandte Chemie* **2024**, *136* (32), e202403023.

(9) Wang, W.; Hu, Y.; Liu, Y.; Zheng, Z.; Chen, S. Self-powered and highly efficient production of H2O2 through a Zn–Air battery with oxygenated carbon electrocatalyst. *ACS applied materials & interfaces* **2018**, *10* (38), 31855-31859.

(10) Pang, Y.; Xie, H.; Sun, Y.; Titirici, M.-M.; Chai, G.-L. Electrochemical oxygen reduction for H 2 O 2 production: catalysts, pH effects and mechanisms. *Journal of Materials Chemistry A* **2020**, *8* (47), 24996-25016.

(11) Wu, M.; Zhan, X.; Yang, S.; Zheng, J.; Cui, X.; Xia, B. Y.; Sun, S.; Yang, Y. The 2e-vs. 4e-Pathways for ORR in Rechargeable Zinc-Air Batteries. *Energy & Environmental Science* **2026**.

(12) Zhang, Y.; Chen, X.; Zhang, H.; Ge, X. Screening of catalytic oxygen reduction reaction activity of 2, 9-dihalo-1, 10-phenanthroline metal complexes: The role of transition metals and halogen substitution. *Journal of Colloid and Interface Science* **2022**, *609*, 130-138.

(13) Wen, Z.; Han, N.; Li, Y. Recent progress towards the production of H2O2 by electrochemical two-electron oxygen reduction reaction. *Acta Physico-Chimica Sinica* **2024**, *40* (2), 2304001.

(14) Zhao, X.; Yang, H.; Xu, J.; Cheng, T.; Li, Y. Bimetallic PdAu nanoframes for electrochemical H2O2 production in acids. *ACS Materials Letters* **2021**, *3* (7), 996-1002.

(15) Yang, Y.; Zhang, H.; Liang, Z.; Yin, Y.; Mei, B.; Song, F.; Sun, F.; Gu, S.; Jiang, Z.; Wu, Y. Role of local coordination in bimetallic sites for oxygen reduction: A theoretical analysis. *Journal of Energy Chemistry* **2020**, *44*, 131-137.

(16) Zhu, T.; Han, Y.; Liu, S.; Yuan, B.; Liu, Y.; Ma, H. Porous materials confining single atoms for catalysis. *Frontiers in Chemistry* **2021**, *9*, 717201.

(17) Yu, B.; Diniz, J.; Lofgren, K.; Liu, Q.; Mercado, R.; Nichols, F.; Oliver, S. R. J.; Chen, S. Copper/Carbon Nanocomposites for Electrocatalytic Reduction of Oxygen to Hydrogen Peroxide. *ACS Sustainable Chemistry & Engineering* **2022**, *10* (47), 15501-15507.

(18) Wang, R.; Zhong, J.; Li, D.; Meng, J.; Huang, W.; Ma, X.; Guo, W.; Tian, F.; Li, C. Engineering d-band center of cobalt active sites via dual coordination with nitrogen-doped carbon nanotube and Ti3C2Tx MXene toward electrocatalytic oxygen reduction for H2O2 production. *Chemical Engineering Journal* **2024**, *488*, 150894.

(19) Liu, K.; Fu, J.; Lin, Y.; Luo, T.; Ni, G.; Li, H.; Lin, Z.; Liu, M. Insights into the activity of single-atom Fe-NC catalysts for oxygen reduction reaction. *Nature Communications* **2022**, *13* (1), 2075.

(20) Song, M.; Liu, W.; Zhang, J.; Zhang, C.; Huang, X.; Wang, D. Single-atom catalysts for H2O2 electrosynthesis via two-electron oxygen reduction reaction. *Advanced Functional Materials* **2023**, *33* (15), 2212087.

(21) Ye, C.; Zhou, Y.; Li, H.; Shen, Y. Single-iron, cobalt, nickel, and copper-atom catalysts for the selective reduction of oxygen to H 2 O 2. *Green Chemistry* **2023**, *25* (10), 3931-3939.

(22) Zhu, Y.; Yang, C.; Lu, T.; Gan, Y.; Zhao, H.; Chen, Y.; Cheng, Q.; Yang, H. Engineering spin state of CoN4-C single atom catalyst for acidic electrosynthesis of hydrogen peroxide. *Nano Energy* **2025**, *141*, 111142.

(23) Liu, Q.; Chen, S. W. Ultrafast synthesis of electrocatalysts. *Trends in Chemistry* **2022**.

(24) Liu, Q.; McNair, S.; Nichols, F.; Lu, B.; Yu, B.; Pan, D.; Ko, J.; Bhuller, A.; Bridges, F.; Chen, S. Ultrafast synthesis of cobalt/carbon nanocomposites by magnetic induction heating for oxygen evolution reaction. *Advanced Sensor and Energy Materials* **2023**, *2* (1), 100046.

(25) Lu, B.; Liu, Q.; Wang, C.; Masood, Z.; Morris, D. J.; Nichols, F.; Mercado, R.; Zhang, P.; Ge, Q.; Xin, H. L.; et al. Ultrafast Preparation of Nonequilibrium FeNi Spinels by Magnetic Induction Heating for Unprecedented Oxygen Evolution Electrocatalysis. *Research 2022*, 9756983. DOI: 10.34133/2022/9756983 (accessed 2023/03/03).

(26) Tressel, J.; Liu, Q.; DuBois, D.; Yu, B.; Warshana, A.; Bridges, F.; Saltikov, C.; Chen, S. Ultrafast Modification of Copper Chlorophyllin by Magnetic Induction Heating for Water Electrodisinfection by Selective Reduction of Oxygen to Hydrogen Peroxide. *The Journal of Physical Chemistry C* **2025**.

(27) Tressel, J.; Nguyen, A.; Nguyen, P.; Jones, C.; Cui, T.; Warshana, A.; Singewald, K.; Millhauser, G.; Saltikov, C.; Chen, S. Ultrafast Synthesis of Titanium Suboxide via Magnetic Induction Heating for Enhanced Photodynamic Activity. *Chemistry–A European Journal* **2026**, e03354.

(28) Yang, L.; Xu, H.; Liu, H.; Zeng, X.; Cheng, D.; Huang, Y.; Zheng, L.; Cao, R.; Cao, D. Oxygen-reconstituted active species of single-atom Cu catalysts for oxygen reduction reaction. *Research* **2020**.

(29) Wang, J.; Li, K.; Xu, R.; Li, S.; Li, Y.; Xia, M.; John, S. T.; Wu, Z. Rational design of the first and second coordination spheres for copper single-atom catalyst to boost highly efficient oxygen reduction. *Applied Surface Science* **2022**, *605*, 154832.

(30) Zhu, W.; Chen, S. Recent Progress of Single-atom Catalysts in the Electrocatalytic Reduction of Oxygen to Hydrogen Peroxide. *Electroanalysis* **2020**, *32* (12), 2591-2602.

(31) Li, H.; Zhu, B.; Cheng, B.; Luo, G.; Xu, J.; Cao, S. Single-atom Cu anchored on N-doped graphene/carbon nitride heterojunction for enhanced photocatalytic H2O2 production. *Journal of Materials Science & Technology* **2023**, *161*, 192-200.

(32) Yu, B. Z.; Liu, Q. M.; Pan, D. J.; Singewald, K.; Dubois, D.; Tressel, J.; Hou, B. Y.; Millhauser, G. L.; Bridges, F.; Chen, S. W. Ultrafast preparation of ruthenium nanoparticle/molybdenum oxide/nitrogen-doped carbon nanocomposites by magnetic induction heating for efficient hydrogen evolution reaction. *J Mater Chem A* **2024**, *12* (26), 16087-16097. DOI: 10.1039/d4ta00884g.

(33) Pan, D. J.; Liu, Q. M.; Yu, B. Z.; DuBois, D. B.; Tressel, J.; Yu, S.; Kaleekal, N.; Trabanino, S.; Jeon, Y.; Bridges, F.; et al. Rapid Synthesis of Ruthenium-Copper

Nanocomposites as High-Performance Bifunctional Electrocatalysts for Electrochemical Water Splitting. *Small* **2024**, 2404729. DOI: 10.1002/smll.202404729.

(34) Booth, C. H.; Bridges, F. Real-Space X-ray Absorption Package (RSXAP). **2021**.

(35) Ravel, B.; Newville, M. ATHENA, ARTEMIS, HEPHAESTUS: data analysis for X-ray absorption spectroscopy using IFEFFIT. *Journal of synchrotron radiation* **2005**, *12* (4), 537-541.

(36) Chen, X.; Wang, X.; Fang, D. A review on C1s XPS-spectra for some kinds of carbon materials. *Fullerenes, Nanotubes and Carbon Nanostructures* **2020**, *28* (12), 1048-1058.

(37) Khan, M. A.; Nayan, N.; Ahmad, M. K.; Soon, C. F. Surface study of CuO nanopetals by advanced nanocharacterization techniques with enhanced optical and catalytic properties. *Nanomaterials* **2020**, *10* (7), 1298.

(38) Jones, C.; Pizano, J.; Tressel, J.; Chen, S. Rapid Fabrication of Cobalt/Cobalt Oxide Heterostructured Catalysts for Efficient Electrochemical Water Splitting. *Chemistry–An Asian Journal* **2026**, *21* (4), e70647.

(39) Xue, S.; Ryan Osterloh, W.; Lv, X.; Liu, N.; Gao, Y.; Lei, H.; Fang, Y.; Sun, Z.; Mei, P.; Kuzuhara, D. Enhanced Four-Electron Oxygen Reduction Selectivity of Clamp-Shaped Cobalt (II) Porphyrin (2.1. 2.1) Complexes. *Angewandte Chemie International Edition* **2023**, *62* (17), e202218567.

(40) Zhang, J.; Zeng, H.; He, B.; Liu, Y.; Xu, J.; Niu, T.; Pan, C.; Zhang, Y.; Lou, Y.; Wang, Y. Suppressing the hydrogen bonding interaction with* OOH toward efficient

H2O2 electrosynthesis via remote electronic tuning of Co-N4. *Applied Catalysis B: Environment and Energy* **2024**, *358*, 124448.

(41) Zhai, L.; Yang, S.; Lu, C.; Cui, C. X.; Xu, Q.; Liu, J.; Yang, X.; Meng, X.; Lu, S.; Zhuang, X. CoN5 sites constructed by anchoring co porphyrins on vinylene-linked covalent organic frameworks for electroreduction of carbon dioxide. *Small* **2022**, *18* (32), 2200736.

(42) Yang, J.; Chen, L.; Zhu, X.; Shi, W.; Huang, M.; Liu, C.; Ding, R.; Gan, L.; Yin, X. Structure–activity relationship in Co–N–C catalysts for multiple H 2 O 2-related electrochemical reactions. *EES Catalysis* **2026**, *4* (1), 201-212.

(43) Lee, J.; Crampton, K. T.; Tallarida, N.; Apkarian, V. A. Visualizing vibrational normal modes of a single molecule with atomically confined light. *Nature* **2019**, *568* (7750), 78-82.

(44) El-Mahalawy, A. M.; Nawar, A. M.; Wassel, A. R. Efficacy assessment of metalloporphyrins as functional materials for photodetection applications: role of central tetrapyrrole metal ions. *Journal of Materials Science* **2022**, *57* (32), 15413-15439.

(45) Ying, Y.; Fang, M.; Wang, C.; Yan, Z.; Xie, H.; Wu, W.; Tang, Z.; Liu, Y. Large-Area Ultrathin Covalent-Organic Framework Membranes for Surface-Enhanced Raman Scattering: Optimal Performance Through Thickness Control. *Small* **2025**, *21* (20), 2501846.

(46) Kazmierczak, N. P.; Lopez, N. E.; Luedecke, K. M.; Hadt, R. G. Determining the key vibrations for spin relaxation in ruffled Cu (II) porphyrins via resonance Raman spectroscopy. *Chemical Science* **2024**, *15* (7), 2380-2390.

(47) Wei, Z.; Su, Y.; Pan, W.; Shen, J.; Fan, R.; Yang, W.; Deng, Z.; Shen, M.; Peng, Y. Covalently grafting graphene onto Si photocathode to expedite aqueous photoelectrochemical CO2 reduction. *Angewandte Chemie International Edition* **2023**, *62* (28), e202305558.

(48) Lyu, F.; Ma, B.; Xie, X.; Song, D.; Lian, Y.; Yang, H.; Hua, W.; Sun, H.; Zhong, J.; Deng, Z. Pre-Activation of CO2 at Cobalt Phthalocyanine-Mg (OH) 2 Interface for Enhanced Turnover Rate. *Advanced Functional Materials* **2023**, *33* (26), 2214609.

(49) Geoghegan, B. L.; Liu, Y.; Peredkov, S.; Dechert, S.; Meyer, F.; DeBeer, S.; Cutsail Iii, G. E. Combining valence-to-core x-ray emission and Cu k-edge x-ray absorption spectroscopies to experimentally assess oxidation state in organometallic Cu (I)/(II)/(III) complexes. *Journal of the American Chemical Society* **2022**, *144* (6), 2520-2534.

(50) Sokol, H. J.; Ebrahim, A. M.; Caratzoulas, S.; Frenkel, A. I.; Valla, J. A. In Situ XAFS, XRD, and DFT characterization of the sulfur adsorption sites on Cu and Ce exchanged Y zeolites. *The Journal of Physical Chemistry C* **2022**, *126* (3), 1496-1512.

(51) Chen, S.; Luo, T.; Li, X.; Chen, K.; Fu, J.; Liu, K.; Cai, C.; Wang, Q.; Li, H.; Chen, Y. Identification of the highly active Co–N4 coordination motif for selective oxygen reduction to hydrogen peroxide. *Journal of the American Chemical Society* **2022**, *144* (32), 14505-14516.

(52) Li, N.; Huang, C.; Wang, X.; Feng, Y.; An, J. Electrosynthesis of hydrogen peroxide via two-electron oxygen reduction reaction: A critical review focus on hydrophilicity/hydrophobicity of carbonaceous electrode. *Chemical Engineering Journal* **2022**, *450*, 138246.

(53) Jiang, H.; Zhao, P.; Shen, H.; Yang, S.; Gao, R.; Guo, Y.; Cao, Y.; Zhang, Q.; Zhang, H. New insight into the electronic effect for Cu porphyrin catalysts in electrocatalytic of CO2 into CH4. *Small* **2024**, *20* (2), 2304998.

(54) Jiang, B.; Gil-Sepulcre, M.; Garrido-Barros, P.; Gimbert-Suriñach, C.; Wang, J. W.; Garcia-Anton, J.; Nolis, P.; Benet-Buchholz, J.; Romero, N.; Sala, X. Unravelling the mechanistic pathway of the hydrogen evolution reaction driven by a cobalt catalyst. *Angewandte Chemie International Edition* **2022**, *61* (40), e202209075.

(55) Mercado, R.; Wahl, C.; En Lu, J.; Zhang, T.; Lu, B.; Zhang, P.; Lu, J. Q.; Allen, A. L.; Zhang, J. Z.; Chen, S. Nitrogen-doped porous carbon cages for electrocatalytic reduction of oxygen: enhanced performance with iron and cobalt dual metal centers. *ChemCatChem* **2020**, *12* (12), 3230-3239.

Chapter 4 Ultrafast Synthesis of Titanium Suboxide via Magnetic Induction Heating for Enhanced Photodynamic Activity

Reproduced with permission from (John Tressel, Alex Nguyen, Phat Nguyen, Colton Jones, Tianchen Cui, Abdelrahman Warshana, Kevin Singewald, Glenn Millhauser, Chad Saltikov, Shaowei Chen, “Ultrafast Synthesis of Titanium Suboxide via Magnetic Induction Heating for Enhanced Photodynamic Activity” Chemistry–A European Journal, 2025 p.e03354.)

4.1. Abstract

Magnéli-phase titanium suboxides (Ti_nO_{2n-1}) have become a focal point of photocatalytic research due to a reduced band gap and enhanced visible light absorption, as compared to the traditional TiO_2. Herein, P25 TiO_2 is converted to mixed-phase Ti_nO_{2n-1} via ultrafast chemical reduction with sodium borohydride using magnetic induction heating (MIH) at controlled currents for 12 s. The obtained samples exhibit an increasing fraction of Ti_2O_3 with the MIH current, from 26% at 200 A to 69% at 600 A. Among the series, the sample prepared at 600 A shows the best photocatalytic activity for water purification as manifested in the degradation of organic dyes (methylene blue) and removal of waterborne pathogens (*Escherichia coli*), due to the photocatalytic reduction of oxygen to hydroxyl radicals. Results from this study highlight the unique potential of MIH in the ultrafast reduction of metal oxides into multiphase heterostructures and their application as high-performance catalysts.

4.2. Introduction

Titanium dioxide (TiO_2) has been one of the most researched photocatalysts due to its low cost, excellent biocompatibility, and good photocatalytic activity.[1, 2] However, one of the core attributes holding back the greater adoption of TiO_2 is the dependency on ultraviolet (UV) light due to a large bandgap over 3 eV.[3, 4] This greatly reduces its real-world applications, as the solar spectrum consists only of about 5% ultraviolet light and applications would require a dedicated light source. As such there has been a

tremendous effort to enhance the visible light absorption of TiO_2 via structural engineering.[5-7] This is vital for photocatalytic water purification, as water borne pathogens kill an estimated 1.7 million people per year globally, and this is predicted to rise as antibiotic resistance increases in common diseases.[8, 9] Towards this end, nanomaterials such as titanium suboxides (TSOs) offer a new pathway for efficient water treatment without increasing the risk of antibiotic resistance buildup.[10-13] TSOs are commonly prepared by chemical reduction of TiO_2 from Ti^{4+} to Ti^{3+} producing a mixed oxidation state.[14-16] In the resultant substoichiometric TiO_{2-x}, the structural defects (e.g., oxygen vacancies) can lower the bandgap and increase visible light absorption, leading to enhanced photocatalytic performance.[17] Nevertheless, Ti^{3+} species are prone to oxidation when exposed to air, and need to be stabilized by appropriate structural engineering, such as formation of heterojunctions and heteroatom doping. For instance, Zhao et al.[18] prepared core@shell carbon-coated Ti_4O_7 and graphitic carbon nitride composites (Ti_4O_7@C/g-C_3N_4) by thermal annealing of TiO_2 in a H_2/Ar reducing atmosphere followed by controlled pyrolysis in the presence of melamine. The samples were found to degrade over 90% of rhodamine B, methylene blue and methyl orange under visible light irradiation for 3.5 h. This activity was ascribed to the formation of oxygen vacancies and Z-scheme heterojunctions that enhanced the separation of photogenerated electron-hole pairs. In another study, Fang et al.[19] prepared Ti^{3+} self-doped TiO_2 via thermal treatment of a titania sol prepared in the presence of $NaBH_4$. They observed enhanced photocatalytic performance towards the degradation of organic dyes with the increasing content of the Ti^{3+} species. Han et

al.[20] prepared boron-doped TiO_2 nanodiamonds via a hydrothermal process, where 10% boron doping was found to be highly beneficial in the photocatalytic degradation of antibiotics, as boron dopants helped stabilize the structure during photocatalysis and assisted in the efficient generation of hydroxyl radicals. This identification of such a moderate dopant concentration was in good alignment with previous studies that found excessive doping might induce structural disordering and compromise the catalytic activity.[21] More recently the TiO_2/Ti_2O_3 phase interaction was explored when, Hu et al.[22] prepared Ti_2O_3@TiO_2 core@shell particles by thermal annealing of commercial Ti_2O_3 in air. Where the TiO_2 content increased by increasing the heating temperature from 100 to 700 ºC, and the sample prepared at 550 ºC exhibited the best photocatalytic activity under visible light irradiation towards the degradation of tetracycline (70% removal after 80 min), due to the formation of mixed-phase heterojunctions. Huang et al.[23] produced Ag/Ti^{3+} /TiO_2 composites via a two-step procedure where Ti^{3+} /TiO_2 nanoparticles were first prepared by calcination treatment of P25 TiO_2 in the presence of $NaBH_4$, followed by the deposition of Ag nanoparticles by chemical reduction of Ag^+ with ascorbic acid. The materials were found to feature a low band gap of 1.14 eV, and Ti^3 + served as the key active sites for hydroxyl radical production. This led to much enhanced photocatalytic activity, with 90% of carbamazepine removed within 10 min and more than 90% inactivation of *Escherichia coli* (*E. coli*) after 5 h‘s visible light irradiation, a performance almost twice that of the Ti^{3+}-free control. Bletsa et al.[24] prepared TSO/polymer composites where the high biocompatibility of TSO was exploited for the effective removal of biofilms from medical devices, as demonstrated

in the effective eradication of biofilms of *E. coli* , *Pseudomonas aeruginosa* (*P. aeruginosa*) and *Staphylococcus aureus* (*S. aureus*) after only 90 min's visible light exposure. This was ascribed to the Ti^{3+} sites for their vital role in band gap reduction, visible light absorption and production of reactive oxygen species (ROS).

TSOs can also be utilized for other (photo)chemical applications. For instance, Han et al.[25] synthesized carbon-doped TiO_x via a thermal oxidation of Ti_3SC_2. The resulting materials exhibited a concentration of Ti^{3+} as high as 73% of titanium and excellent photocatalytic efficiency towards nitrogen fixation to NH_3 at a rate of 109.3 mmol g^{-1} h^{-1} under visible light irradiation. Yu et al.[26] reported the synthesis of Magnéli-phase TSOs by flash spark plasma sintering, which exhibited enhanced ambient electrical conductivity and thermoelectric properties as compared to those by conventional spark plasma sintering. Notably, Magnéli-phase TSOs with a minimal band gap of under 0.2 eV can also be utilized in electrochemistry and battery technologies due to their high electrical conductivity. For instance, Liu et al.[27] prepared a sulfur-doped Ti_4O_7 cathode via thermal reduction of TiO_2 followed by sonication and condensation of carbon disulfide and observed an ultralow degradation of only 0.09% per battery cycle in a lithium-sulfur battery.

In these earlier studies, TSOs were mostly prepared by conventional thermal procedures that are energy- and time-consuming, with limited transformation of Ti^{4+} to Ti^{3+} . In this work, Magnéli- phase TSOs were prepared by ultrafast synthesis based on magnetic induction heating (MIH) of P25 TiO_2 in the presence of $NaBH_4$. This was to take advantage of the instant generation of an eddy current when a conductor was

immersed into a magnetic field that could heat up the substrate to a temperature over 1000 ºC within seconds allowing for the production of nonequilibrium/defective structures.[28-35] Indeed, the obtained samples contained mixed phases of TiO_2, Ti_4O_7 and Ti_2O_3, due to partial reduction of Ti^{4+} to Ti^{3+}. The structural modification led to a diminishment of the material's bandgap and enhanced visible light absorption, allowing for white light photocatalysis. Among the series, the sample prepared at 600 A for 12 s exhibited the best performance towards water disinfection, as exemplified by the degradation of methylene blue and eradication of *Escherichia coli* (*E. coli*), due to unique band structures that facilitated the production of hydroxyl (•OH) radicals under visible light irradiation and the formation of a multiphase structure that was conducive to vectorial charge separation.

4.3. Results and Discussion

4.3.1 Structural characterization

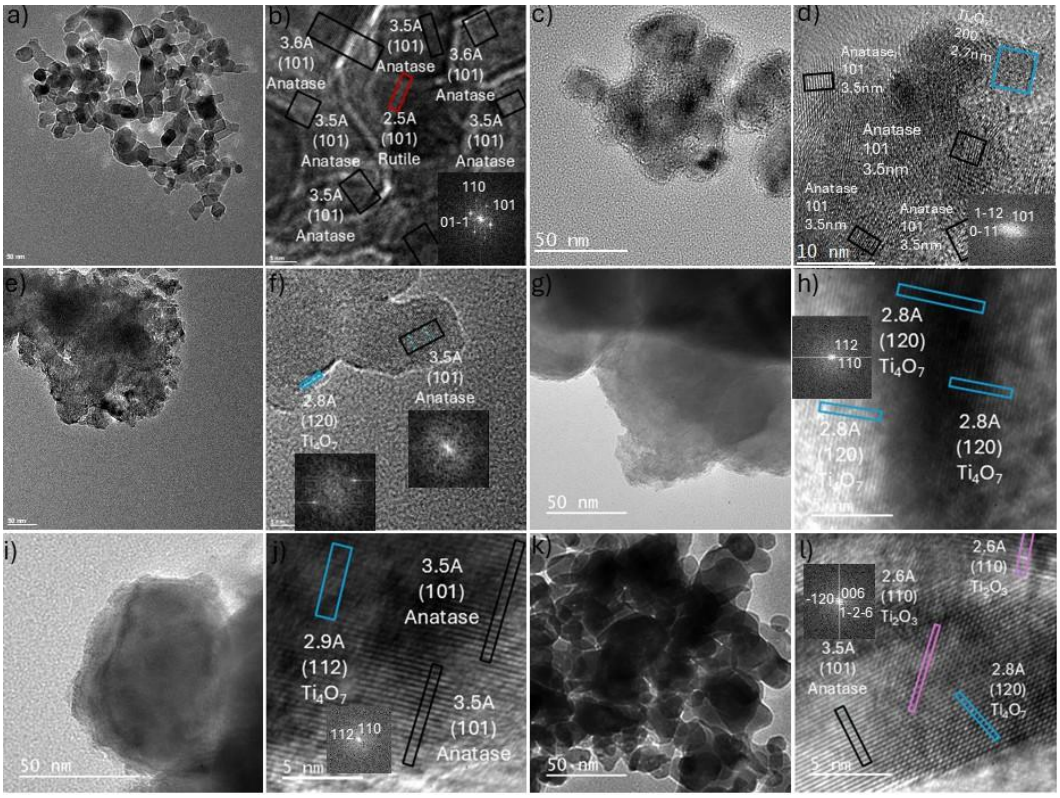

Figure 1. TEM images of (a,b) P25 TiO_2, (c,d) TiO_2-TF, (e,f) TiO_2-300, (g,h) TiO_2-400, (i,j) TiO_2-500 and (k,l) TiO_2-600. Insets to (b), (d), (f), (h), (j) and (l) are the corresponding FFT patterns.

The samples were prepared by MIH treatment of P25 TiO_2 at select induction currents (X = 200 – 600 A) for 12 s and denoted as TiO_2-X. A control sample was prepared by conventional heating with a tube furnace at the heating rate of 10 °C min^{-1} in a flowing nitrogen atmosphere 450 °C for 2 h and referred to as TiO_2-TF. Details are included in

the Experimental Section. The sample structures were first examined by transmission electron microscopy (TEM) measurements. For pristine P25 TiO_2 (**Figure 1a-b**) the sample can be seen to feature a particle size of 20-25 nm and well-defined lattice fringes arising from a mix of the anatase and rutile phases, as manifested by the interplanar spacings of 1.9, 2.5 and 3.6 Å that can be ascribed to the anatase (200), rutile (101) and anatase (101) crystalline planes, respectively. High crystalinity and clear anatase planes are identifiable in the fast Fourier transform (FFT) patterns (inset to **Figure 1b**).[36] Such crystalline domains can also be clearly resolved with TiO_2-TF (**Figure 1c-d**). By contrast, after MIH treatment in the presence of $NaBH_4$, the particles became markedly agglomerated and displayed new sets of lattice fringes. For instance, TiO_2-300 (**Figure 1e-f**), TiO_2-400 **(Figure 1g-h**), and TiO_2-500 (**Figure 1i-j**), now possesse a mix of anatase TiO_2 and Ti_4O_7 with two different interplanar spacings of 2.7 and 3.6 Å, due to Ti_4O_7 (200) and anatase (101) planes; additioanlly, the FFTs show a decrease in clear crystal strucutres with fewer identifiable planes.[37, 38] For TiO_2-600 that was prepared at an even higher induction current (temperature) (**Figure 1k-l**), corundum Ti_2O_3 crystalline domains became the dominant component. Along with this is an increase in the clairity of the FFTs having three identiable planes of Ti_2O_3 (006), ($\bar{1}$20), and ($1\bar{2}\bar{6}$) incidating a more complete formation of the Ti_2O_3 strucutre as the heating progressed. These observations suggest effective transformation of P25 TiO_2 into Ti_2O_3 by MIH thermal reduction with $NaBH_4$, with Ti_4O_7 being a key intermediate.[39] The fact that the rutile phase vanished whereas the anatase phase remained visible might be

ascribed to the vastly different contents of anatase (ca. 80%) and rutile phases (ca. 20%) in pristine P25 TiO_2.[36]

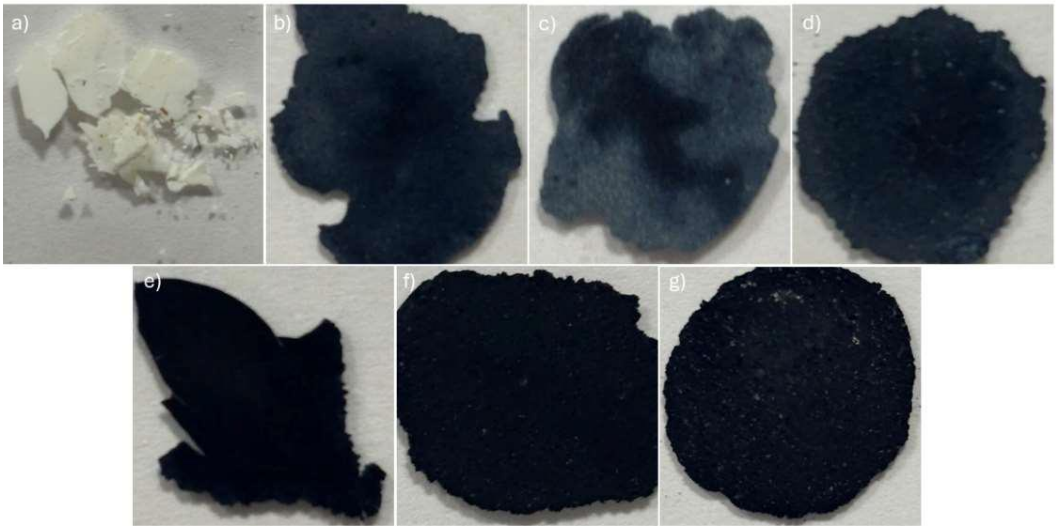

Figure 2. Photographs of the sample series: (a) P25, (b) TiO_2-TF, (c) TiO_2-200, (d) TiO_2-300, (e) TiO_2-400, (f) TiO_2-500, and (g) TiO_2-600.

Notably, the sample color appearance exhibited a drastic change from a light sandy color of pristine P25 TiO_2 to dark blue after thermal reduction by $NaNH_4$; and the blue color became intensified with increasing MIH current (**Figure 2**). This signifies increasing reduction of Ti^{4+} to Ti^{3+} and the formation of TSOs.

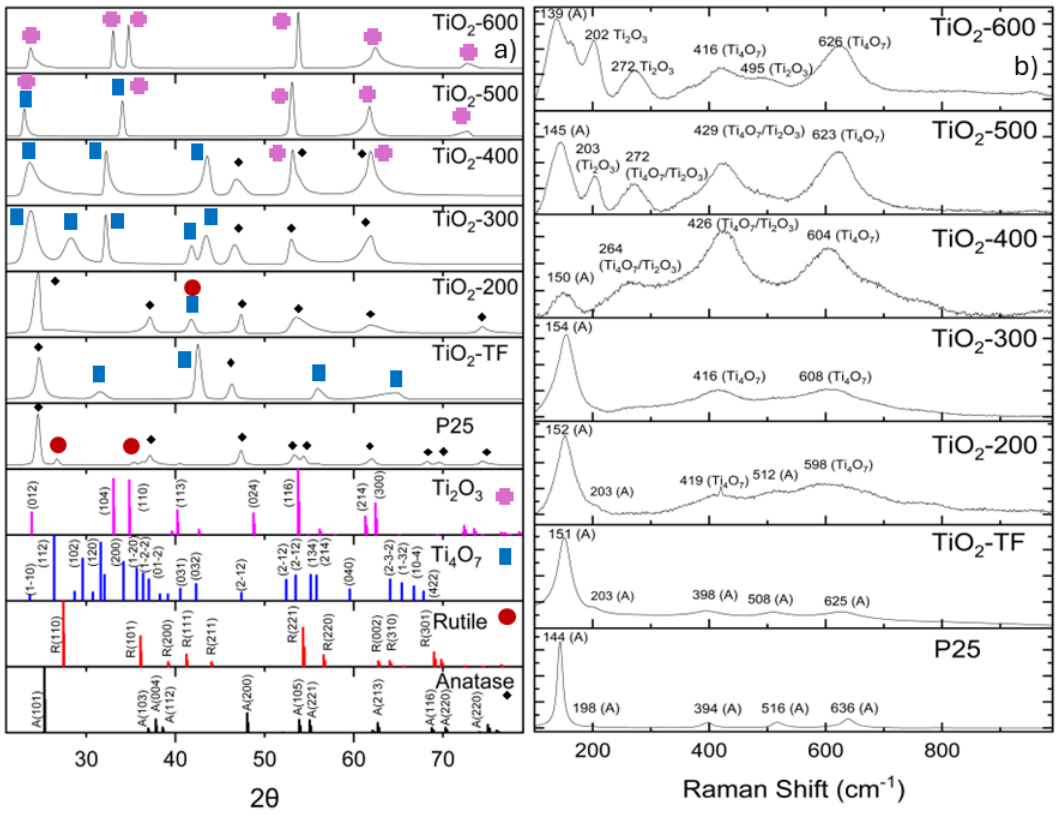

Figure 3. (a) XRD patterns with standard references and (b) Raman spectra of the sample series.

Consistent results were obtained from X-ray diffraction (XRD) measurements. **Figure 3a** depicts the diffraction patterns of the sample series. One can see that P25 TiO_2 indeed consisted a mix of the anatase (A, JCPDS #21-1272) and rutile (R, JCPDS #74-1984), with A(101) at 2q = 24.5º being the primary peak and R(110) at 26.7º being the clearest rutile peak. Upon MIH treatment, the peaks were markedly broadened, and discerning speacific peaks became less clear. For TiO_2-200, the anatase phase remained the dominant component with A(101) at 24.6º, A(004) at 37.1º, and A(105) at 53.6º, along with the emergence of a combined Ti_4O_7(032) (JCPDS #50-0787) and rutile (111)

peak at 41.8º, suggesting minimal impacts on the TiO_2 structure at this temperature. For TiO_2-300 that was prepared at a higher induction temperature, in addition to the anatase patterns, the Ti_4O_7 phase became intensified with diffraction peaks at 23.8º, 28.3º, 32.2º, and 43.5º due to the (112), (102), (120), and (032) planes, respectively.[27] TiO_2-400 exhibited similar patterns, whereas for TiO_2-500, the diffraction patterns now resembled those of corundum Ti_2O_3 (JCPDS #44-1294) with the characteristic peaks at 23.1º, 34.0º, 53.1º, and 61.8º due to the (012), (104)/(110), (116) and (300) planes and shrinking intesnity of the Ti_4O_7(120) and Ti_4O_7(112) peaks. Finally, TiO_2-600 shows the strongest Ti_2O_3 signals with the (104)/(110) doublet and the (116) peak being the dominate peaks, a telltale sign of a corundum Ti_2O_3 strucuture. These results suggest effective structural transformation of TiO_2 by MIH treatment to corundum Ti_2O_3 with Ti_4O_7 being the structural intermediate, as the Ti^{4+} centers were increasingly reduced to Ti^{3+}. For comparison, under conventional thermal annealing, the TiO_2-TF sample displayed a pattern that was analogous to that of the TiO_2-200 sample with anatase remaining the dominant phase, suggesting limited reduction of the P25 TiO_2. This is likely because the relatively slow heating rate produced an H_2-poor atmosphere from thermolysis of $NaBH_4$, whereas during MIH the rapid heating led to the production of a burst of H_2 and concurrently activation of TiO_2 for reduction. It should be noted that a totally different phase transition has been documented to occur in thermal annealing without the addition of $NaBH_4$ where anatase TiO_2 is transformed to rutile at elevated temperatures.[40]

Such structural dynamics were also observed in Raman measurements. From **Figure 3b**, pristine TiO_2 exhibited five vibrational bands all characteristic of the anatase phase. The dominant lattice vibration at 144 cm^{-1} (E_g, which overlaps with the B_{1g} vibration of rutile TiO_2), O-Ti-O symmetric bending of O around Ti centers at 198 cm^{-1} (E_g), O-Ti-O asymmetric bending within the TiO_6 octahedra at 394 cm^{-1} (B_{1g}), O-Ti-O symmetric and asymmetric stretching at 516 cm^{-1} (A_{1g}+B_{1g}), and Ti-O symmetric stretching at 636 cm^{-1} (E_g).[41, 42] Notably, after MIH treatment, the Raman features became markedly broadened and new bands emerged. For TiO_2-200, the anatase vibrations shifted slightly to 152, 203, and 512 cm^{-1}, with two new bands at ca. 419 (A_{1g}) and 598 cm^{-1} (B_{2g}) that most likely arose from the Ti-O stretching of Ti_4O_7.[43-45] TiO_2-300 exhibited a similar profile where only the primary anatase peak remained but has broadened significantly to 154 cm^{-1} with the 203 cm^{-1} band no longer being distinguishable. Furthermore, the Ti_4O_7 peaks continued to grow at 416 and 608 cm^{-1}. For the TiO_2-400 sample, the anatase vibration at 150 cm^{-1} diminished in intensity, whereas TSO features became prominent at 264 and 426 cm^{-1} for Ti_4O_7/Ti_2O_3 and 604 cm^{-1} for Ti_4O_7.[46] For TiO_2-500 and TiO_2-600, the Ti_2O_3 vibrations became increasingly intensified at ca. 203, 272 and 495 cm^{-1}.[47, 48] These results suggest the formation of a mixed phase structure within the samples, as observed in the above TEM and XRD measurements. The broadening of the vibrational profiles was likely caused by the loss of lattice oxygen that facilitated the formation of amorphous/defective domains and the emergence of the suboxide species. **Table 1** lists the full width at half maximum (FWHM) of three major peaks that are found in all samples. One can see that for the

E_g peak at ca. 150 cm^{-1} , the FWHM initially increased with MIH temperature reaching a maximum with the TiO_2 -500 sample and then declined somewhat with TiO_2 - 600 where suboxide species became dominant.

Table 1. Peak positions and FWHM of three primary Raman peaks that are seen in all samples

Sample	**E_g**		**Anatase B_{1g}/TSO A_{1g}**		**Anatase E_g/TSO B_{2g}**	
	Peak position (cm^{-1})	**FWHM (cm^{-1})**	**Peak position (cm^{-1})**	**FWHM (cm^{-1})**	**Peak position (cm^{-1})**	**FWHM (cm^{-1})**
P25	144	12	394	29	636	28
TiO_2-TF	151	29	398	124	625	112
TiO_2-200	152	33	419	70	598	215
TiO_2-300	154	35	416	144	608	170
TiO_2-400	150	36	426	95	604	135
TiO_2-500	145	41	429	83	623	67
TiO_2-600	139	34	416	80	626	63

This aligns well with results from previous studies where increased heating and metal reduction increased the concentrations of Ti^{3+} and oxygen vacancies, hence producing a defective structure.[19] For the anatase B_{1g} /TSO A_{1g} peak at ca. 410 cm^{-1} , an almost bell-shaped trend can be seen of the FWHM with the maximum being TiO_2-300, as the anatase structure became increasingly defective with increasing heating and concurrently the suboxide structure became progressively dominant, as observed in the above XRD and TEM measurements. This is further supported by the shift of the peak position from 394 cm^{-1} (anatase) in P25 to 429 cm^{-1} (mixed suboxides) in TiO_2 -500 and the splitting into 2 peaks at 416 cm^{-1} for Ti_4O_7 and 495 cm^{-1} for Ti_2O_3 in TiO_2 -600. The FWHM of the anatase E_g / TSO B_{2g} peak at ca. 620 cm^{-1} exhibited a similar trend. It has been observed previously that a partially defective crystal structure can be beneficial for photocatalysis, but excessive defects may actually trap charge carriers and impede charge separation compromising the photocatalytic activity (vide infra).[49, 50] The elemental composition and valence state of the samples were then examined by X-ray photoelectron spectroscopy (XPS) measurements.

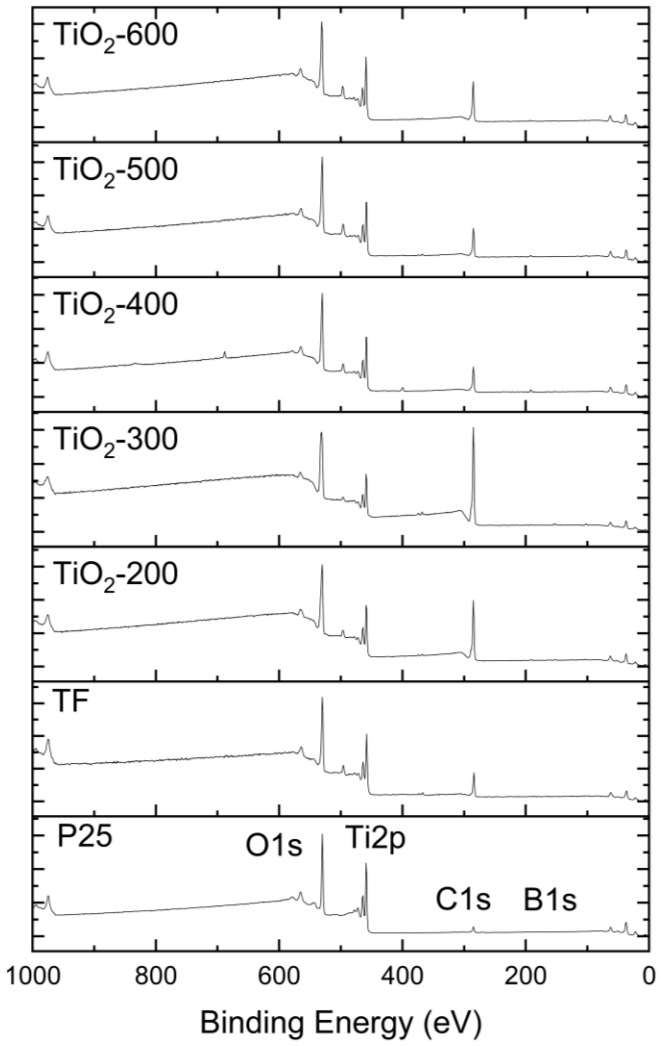

Figure 4. XPS Survey Spectra of the sample series.

From the survey spectra in **Figure 4**, the Ti 2p and O 1s electrons can be resolved at ca. 462 and 530 eV, respectively, with an additional peak at ca. 190 eV for the B 1s electrons for the thermally treated samples (the C 1s signals at ca. 285 eV likely arose from adventitious carbon, **Figure 5**).

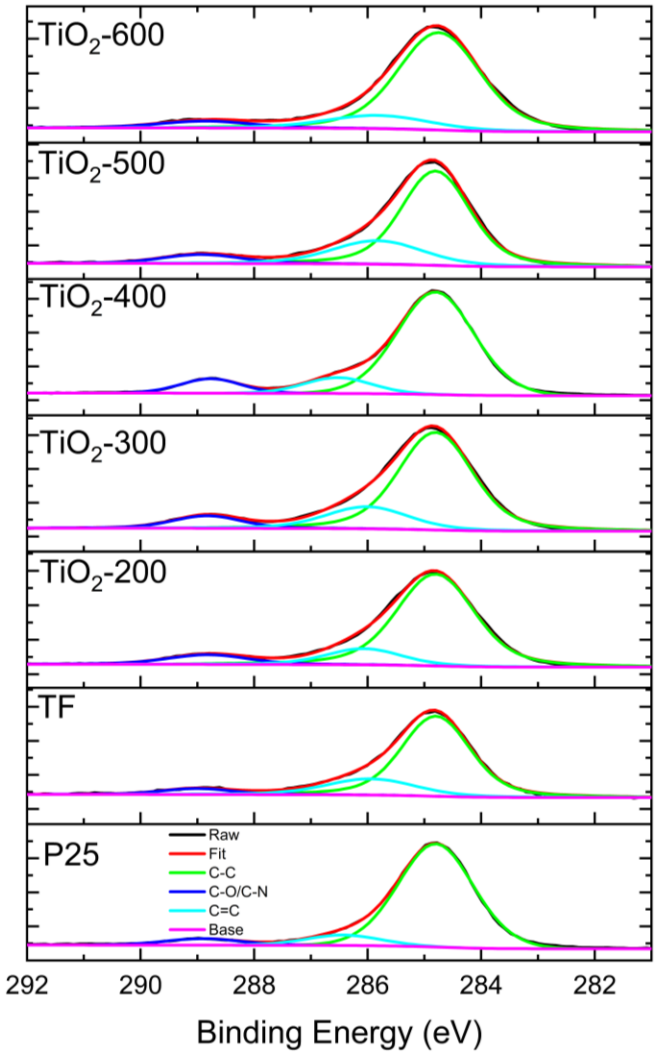

Figure 5. High-resolution scans of the C 1s electrons of the sample series.

The high-resolution scans of the Ti 2p electrons are shown in **Figure 6a**. It can be seen that the pristine P25 TiO_2 exhibited a lone doublet at 458.92/464.58 eV due to the Ti^{4+} $2p_{3/2}/2p_{1/2}$ electrons; whereas for the thermally treated samples, a second doublet can be resolved at ca. 458.60/465.10 eV, in addition to the Ti^{4+} doublet at ca. 459.00/465.00, confirming partial reduction of Ti^{4+} to Ti^{3+} in the samples (**Table 2**).[51, 52]

Table 2. Binding energies (eV) of the sample series from XPS measurements

Species		**P25**	**TiO_2-TF**	**TiO_2-200**	**TiO_2-300**	**TiO_2-400**	**TiO_2-500**	**TiO_2-600**
B 1s	Interstitial B		187.86	187.44	186.85	187.21	187.21	186.69
	B-O		192.23	192.05	192.19	192.11	192.04	191.95
C 1s	C-C	284.8	284.8	284.8	284.8	284.8	284.8	284.8
	C-N/C-O	286.48	285.94	286.07	286.01	285.96	285.83	286.46
	C=N/C=O	288.88	289.01	288.82	288.82	289.08	288.92	288.94
Ti 2p	Ti^{3+} $2p_{3/2}$		458.34	458.3	458.51	458.53	458.52	458.45
	Ti^{4+} $2p_{3/2}$	458.92	458.93	458.8	459.04	458.8	458.92	458.87
	Ti^{3+} $2p_{1/2}$		463.84	463.8	464.01	464.03	464.09	464.04
	Ti^{4+} $2p_{1/2}$	464.58	464.68	464.51	464.78	464.62	464.69	464.67
O 1s	O-Ti	529.86	530.45	529.76	529.99	530.08	530.09	529.92
	O vacancy	531.27	531.93	531.5	531.77	531.66	531.56	531.71
	adsorbed O			533.08	533.22	535.89	533.07	533.26

Furthermore, the fraction of Ti^{3+} can be seen to increase with increasing MIH temperature, 28% in TiO_2-200, 26% in TiO_2-300, 43% in TiO_2-400, 57%% in TiO_2-500, and 69% in TiO_2-600 (**Table 3**). This is in good agreement with the phase changes seen in the above XRD, TEM and Raman measurements.

Table 3. Elemental contents (at%) of the sample series from XPS measurements

Species		**P25**	**TiO_2-TF**	**TiO_2-200**	**TiO_2-300**	**TiO_2-400**	**TiO_2-500**	**TiO_2-600**
B 1s	Interstitial B		2.06	0.24	0.45	1.04	0.91	0.96
	B-O		2.57	1.19	1.1	6.21	4.3	2.47
C 1s	C-C	5.45	25.54	41.81	46.35	21.47	24.94	35.71
	C-N/C-O	1.65	6.74	7.22	11.72	8.02	8.33	2.65
	C=N/C=O	0.79	1.99	4.64	5.51	2.83	2.8	2.35
Ti 2p	Ti^{3+} $2p_{3/2}$		2.92	2.06	1.09	4.53	6.23	8.92
	Ti^{4+} $2p_{3/2}$	20.1	9.11	5.17	3.16	6.01	4.7	4.05
	Ti^{3+} $2p_{1/2}$		1.32	0.93	0.49	2.04	2.81	4.03
	Ti^{4+} $2p_{1/2}$	9.31	4.12	2.33	1.43	2.72	2.13	1.83
O 1s	O-Ti	59.13	29.68	18.75	11.38	26.94	26.3	26.38
	O vacancy	3.66	13.96	9.52	10.06	17.95	12.57	7.55
	adsorbed O			6.14	7.26	0.24	3.98	3.1

The associated O 1s spectra are shown in **Figure 6b**, where the lattice O-Ti peak can be resolved at ca. 530.0 for all samples, along with oxygen vacancy at ca. 531.50 eV and surface-adsorbed oxygen species at ca. 533.22 eV.[53, 54] Notably, for P25 TiO_2, the Ti:lattice O ratio can be estimated to be 1:2.02, in excellent match with the expected stoichiometry of TiO_2. Yet the ratio increased to 1:1.79 for TiO_2-200, 1.84 for TiO_2-300, 1.76 for TiO_2-400, 1.66 for TiO_2-500, and 1.40 for TiO_2-600 (**Table 3**), closely

matching what would be expected for the ratio to shift going from TiO_2 to Ti_4O_7 then Ti_2O_3.

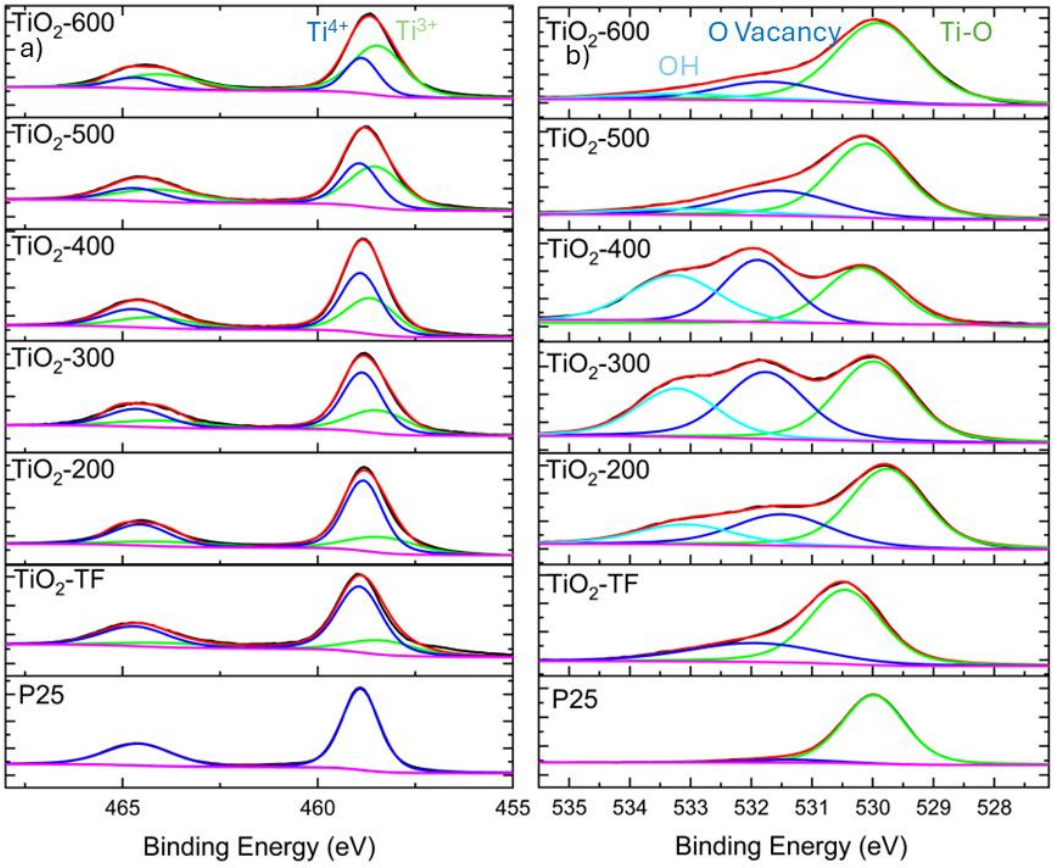

Figure 6. XPS spectra of the (a) Ti 2p and (b) O1s electrons of the sample series.

Meanwhile, the content of oxygen vacancy increased from ca. 3.66 at% in P25 TiO_2 to 9.52 at% in TiO_2-200, 10.06 at% in TiO_2-300, 17.95 at% in TiO_2-400, 12.57 at% in TiO_2-500, and 7.55 at% in TiO_2-600.

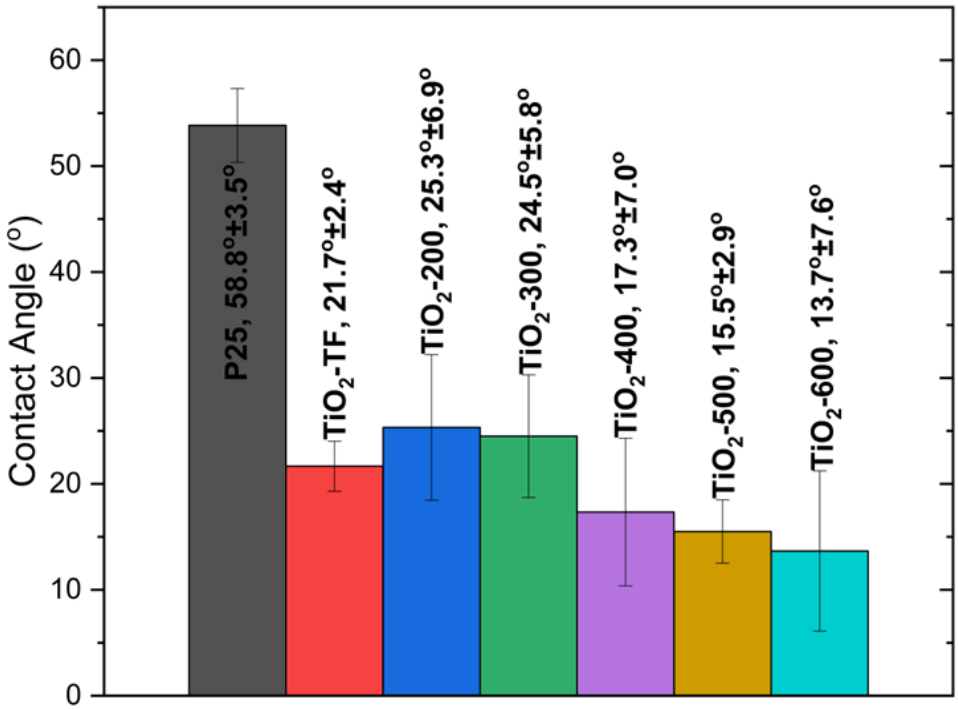

Figure 7. Contact angles of 10 mL water droplets measured on the TiO_2 sample series.

This led to significant enhancement of the materials hydrophilicity, as evidenced in contact angle measurements. From **Figure 7**, P25 TiO_2 can be seen to exhibit a contact angle of 58.8º ± 3.5º, which decreased markedly after thermal reduction to 25.3º ± 6.9º for TiO_2-200 and further to 13.7º ± 7.6º for TiO_2-600.

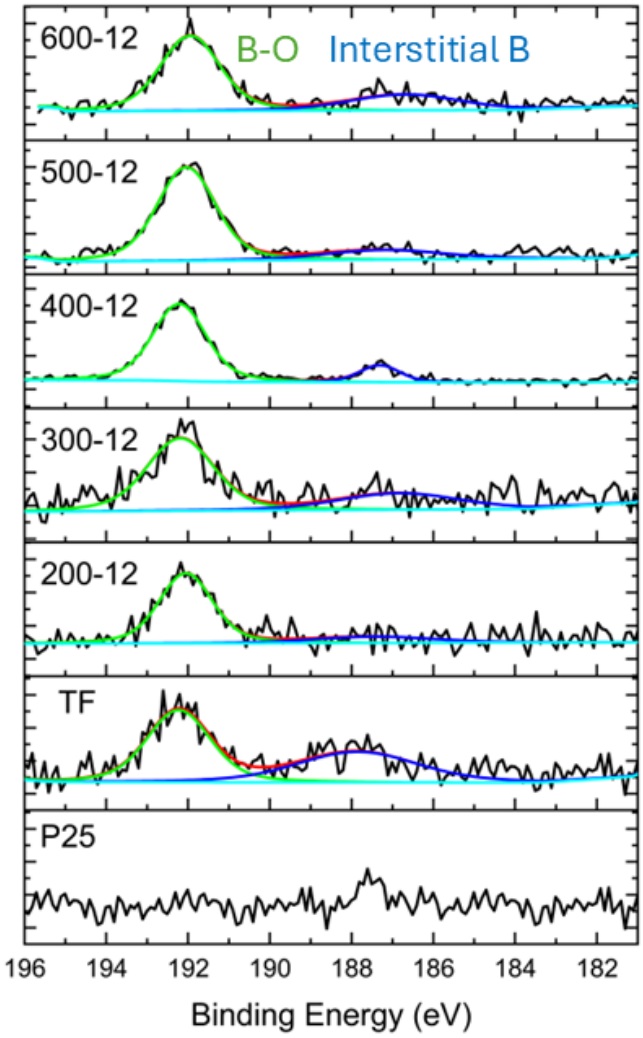

Figure 8. High-resolution scans of the B 1s electrons of the sample series.

Figure 8 shows the B 1s scans. In contrast to the featureless profile of the P25 TiO_2, all thermally treated samples possessed two species, interstitial B (B-Ti) at ca. 187.8 eV and oxidized B (B-O) at ca. 192.5 eV (**Table 2**).[55] This suggests that MIH treatment in the presence of $NaBH_4$ led to the doping of B into the sample matrix, at a low doping level mostly under 1 at% (**Table 3**).[56, 57] It has been shown previously that slight boron

doping could stabilize Ti^{3+} where the Ti-O-B bonding interactions helped maintain the materials structure during catalysis and facilitate hydroxyl radical production.[58]

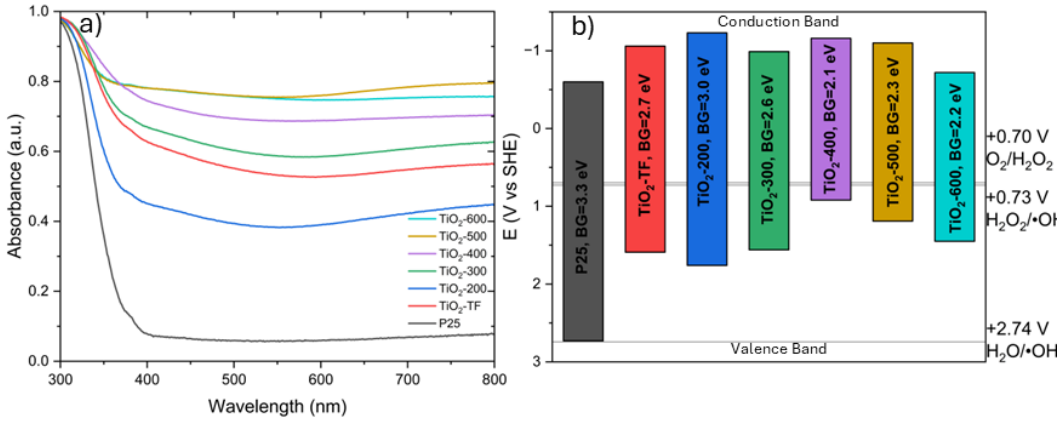

Figure 9. (a) UV-vis diffuse reflectance spectra and (b) band structures with possible radicals produced by photocatalysis of the sample series.

Results from the above measurements confirmed the successful formation of mixed-phase TSOs with low B doping by MIH treatment in the presence of $NaBH_4$. This structural transition was also evidenced in UV-vis diffuse reflectance spectroscopy (DRS) measurements. **Figure 9a** depicts the UV-vis diffuse reflectance spectra for the various samples. One can see that MIH treatment led to a significant increase of absorbance in the visible range, and the absorbance became intensified with increasing induction current, as compared to pristine P25 TiO_2. In fact, from the Tauc plot in **Figure 10**, P25 TiO_2 can be seen to exhibit a band gap of ca. 3.33 eV, which diminished drastically to 2.65 eV for TiO_2-TF, 2.99 eV for TiO_2-200, 2.55 eV for TiO_2-300, 2.08 eV for TiO_2-400, 2.29 eV for TiO_2-500, and 2.17 eV for TiO_2-600.[59, 60]

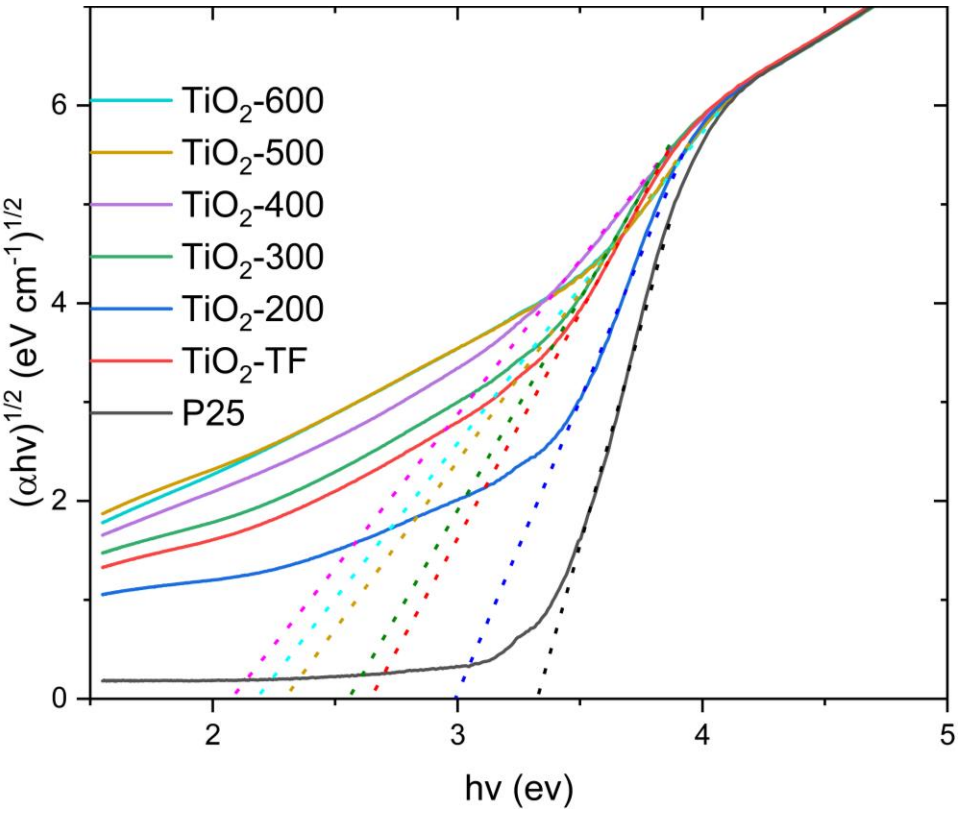

Figure 10. Tauc plots of the samples derived from the UV-vis absorption profiles. Dashed lines represent linear extrapolations to the x axis.

This is in good agreement with the emergence of TSOs (e.g., Ti_4O_7 and Ti_2O_3) after MIH treatment in the presence of $NaBH_4$ and enhanced photodynamic activity towards *E. coli*, as detailed below.

4.3.2 Photodynamic activity

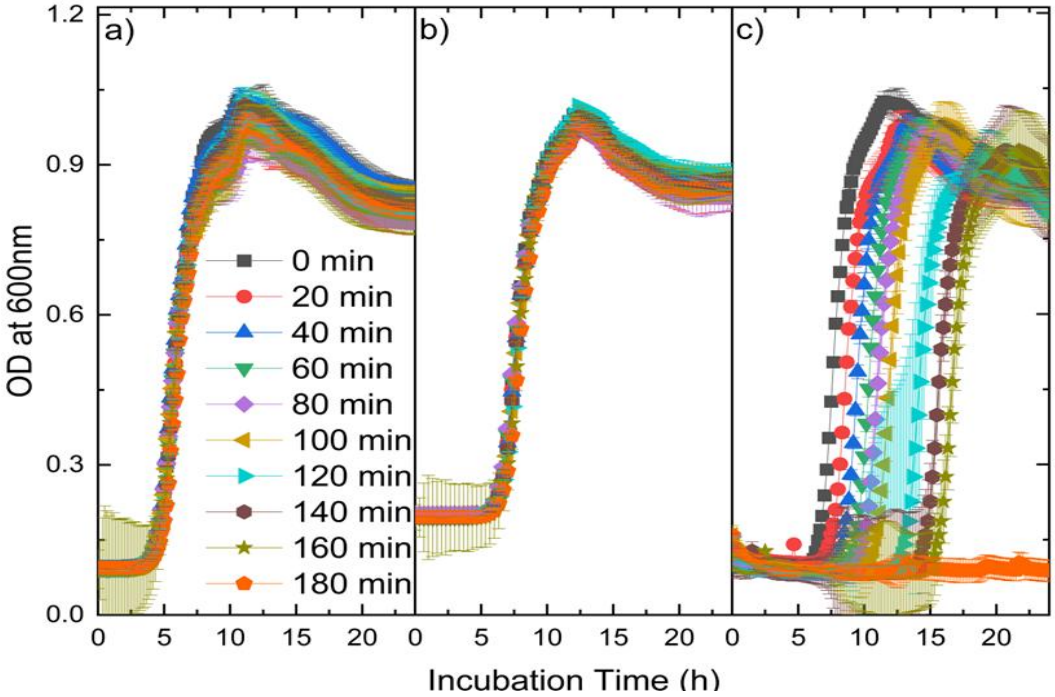

Figure 11. Growth curves of *E. coli* (a) in the absence of catalysts under visible light irradiation for up to 3 h and (b,c) in the presence of TiO_2-600 but (b) in the dark and (c) under visible light irradiation for up to 3 h.

The photocatalytic activity of the samples towards eradication of water-borne pathogenic bacteria was then evaluated and compared. **Figure 11a** depicts the growth curves of E. coli under white light irradiation for up to three hours without the addition of any catalyst sample. It can be seen that photoirradiation alone did not impact the bacterial cell growth. Similarly, no variation of the bacteria growth was observed with the addition of TiO_2-600 after 3 hours in the dark (**Figure 11b**), indicating the material is not active without light. Yet, upon photoirradiation for up to three hours, a clear

inhibition was observed in the presence of TiO_2-600 with the growth phase being delayed from 6.3 h of incubation without light exposure to 15.3 h after 160 min of light exposure, and an almost complete lack of growth after 180 min (**Figure 11c**). In fact, with a generation time of ca. 41 min, the number of *E. coli* cells in the solution was reduced to less than 1.5% after irradiation. For comparison, P25 TiO_2 exhibited only a minimal impact, with virtually no inhibition of the bacterial growth, most likely due to the large bandgap and low absorbance in the visible range.

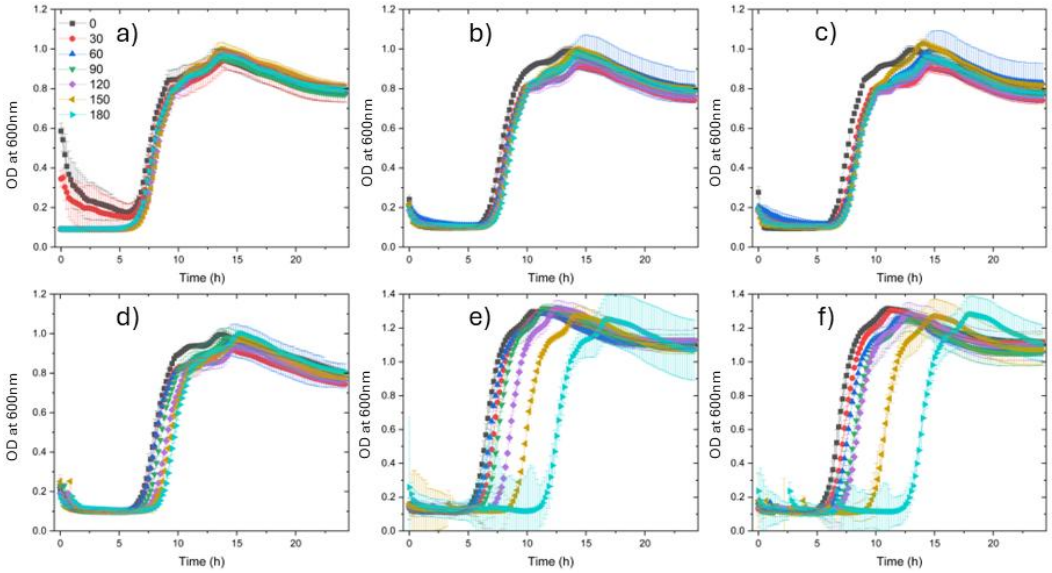

Figure 12. White light *E. coli* growth curves under white light irradiation in the presence of (a) P25, (b) TiO_2-TF, (c) TiO_2-200, (d) TiO_2-300, (e) TiO_2-400, and (f) TiO_2-500.

Yet the photodynamic activity was markedly enhanced with the samples thermally treated in the presence of $NaBH_4$ (**Figure 12**), with the lag phase increasing in the order

of P25 TiO_2 < TiO_2 -TF ≈ TiO_2 - 200 < TiO_2 -300 < TiO_2 -400 < TiO_2 -500 < TiO_2 -600 (**Figure 13**).

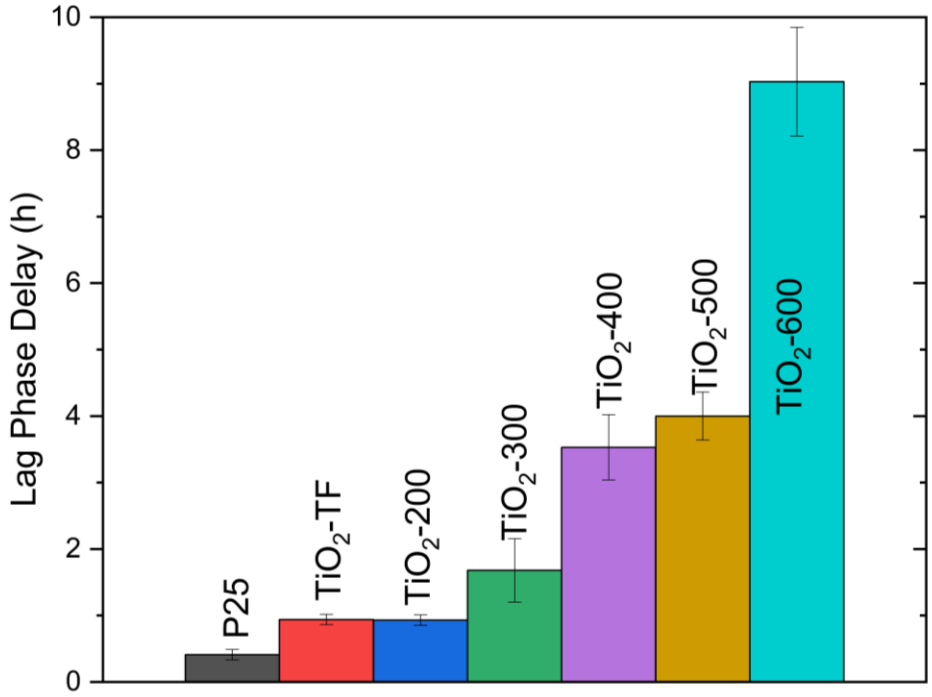

Figure 13. Lag phase delays for all samples after 150 minutes of white light irradiation calculated from White *E. coli* growth curves.

These observations suggest that TiO_2-600 stood out as the best photodynamic agent among the series, most due to the extensive reduction of Ti^{4+} to Ti^{3+} . A similar trend was observed in the photocatalytic degradation of methylene blue (**Figure 14**).

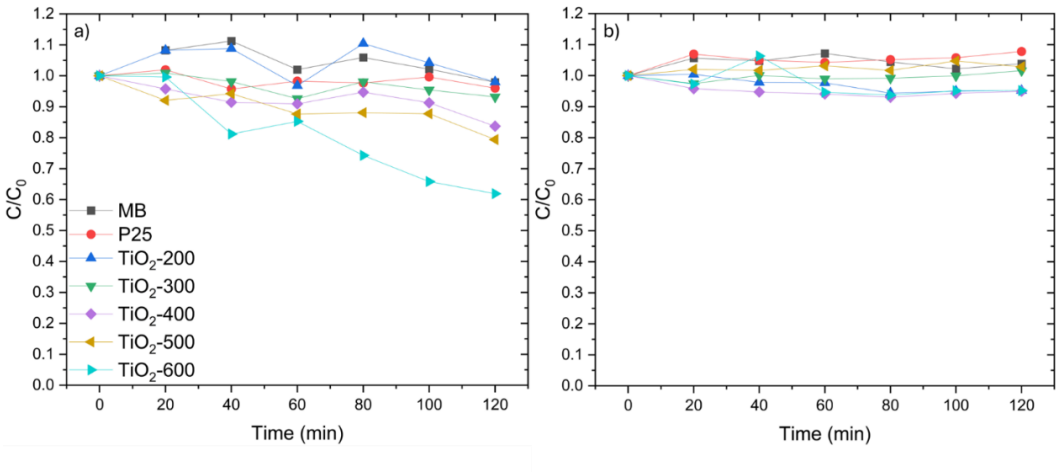

Figure 14. Photocatalytic degradation of methylene blue dye degradation in the absence and presence of varied samples under (a) white light irradiation and (b) as a dark control for 120 minutes.

Consistent results were obtained in scanning electron microscopy (SEM) measurements.

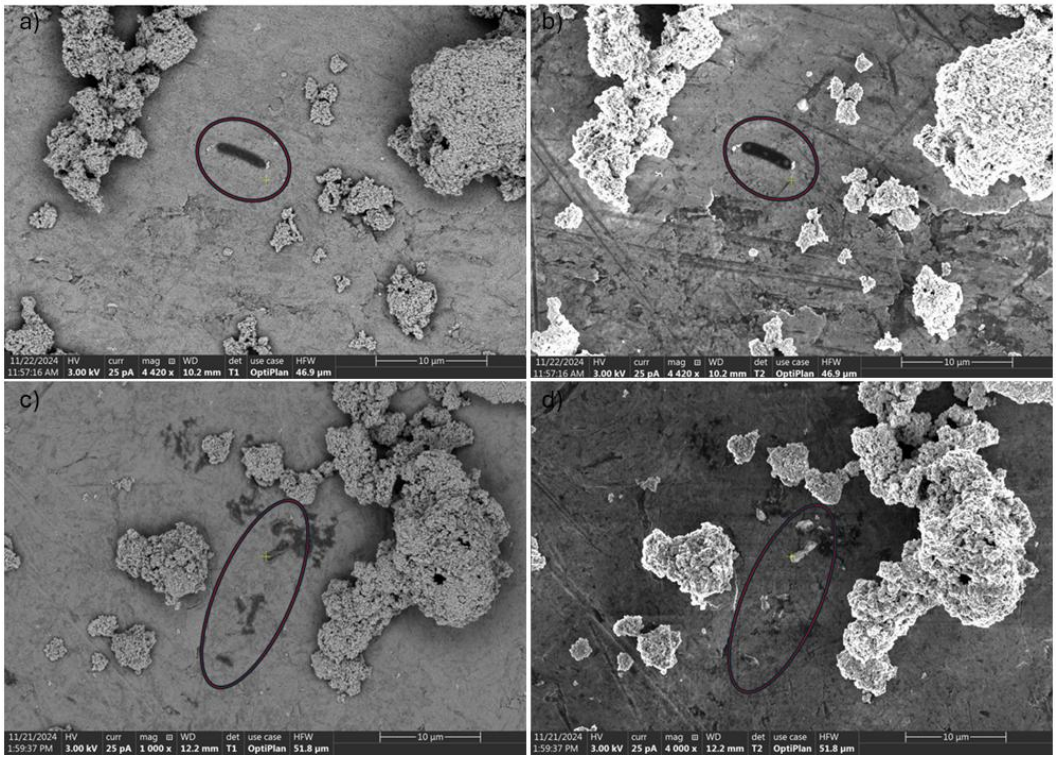

Figure 15. SEM images of *E. coli* in the presence of TiO_2-600 (a,b) after 3 h in the dark and (c,d) after 3 h of visible light irradiation. Panels (a, c) are the secondary electron images and (b, d) are the backscattered electron image.

As seen in **Figure 15a-b**, the bacterial cell morphology remained largely intact in the presence of TiO_2-600 after 3 hours in the dark; yet upon white light irradiation for 3 h (**Figure 15c-d**), apparent annihilation of the bacterial cells can be seen, where the cell membranes were shredded leaving behind pieces with no complete bacterial cells. This further confirms the effectiveness of TiO_2-600 in eliminating *E. coli* in water via photocatalytic activity and not physical interactions.

4.3.3 Mechanistic study

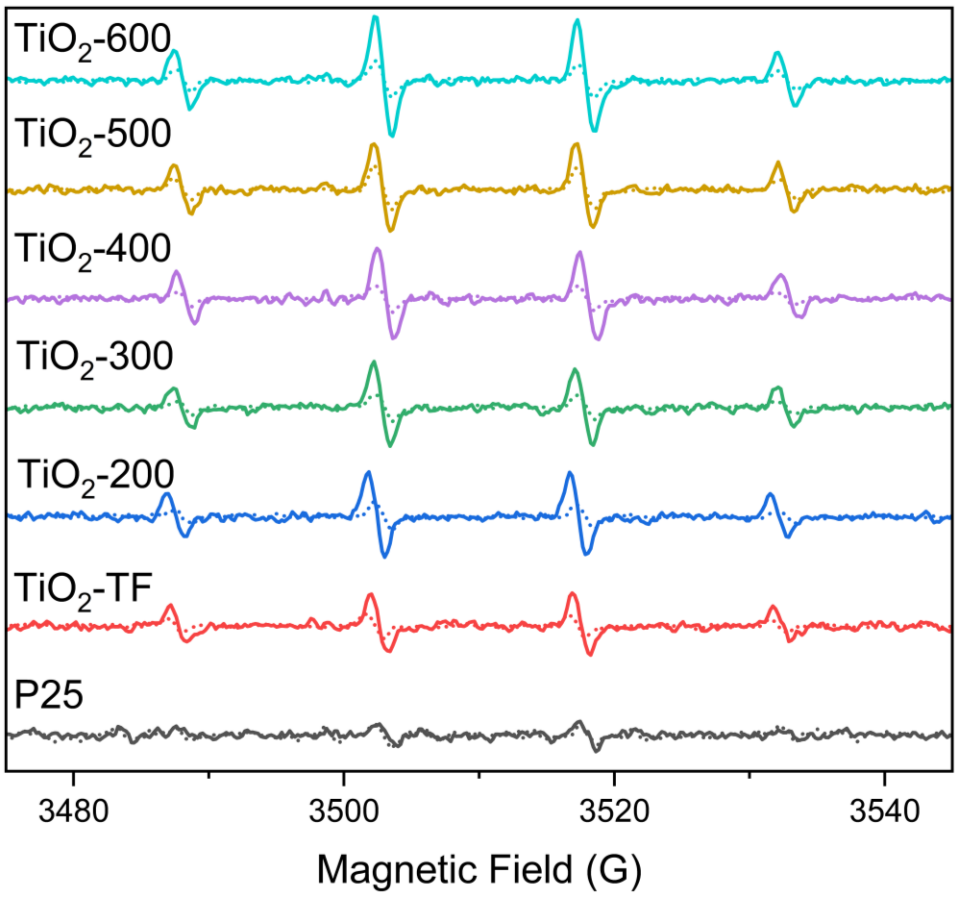

Figure 16. EPR spectra of the sample series with DMPO as the spin trap before (dotted curves) and after (solid curves) visible light irradiation for 3 h.

Electron paramagnetic resonance (EPR) measurements were then carried out to unravel the mechanistic origin of the photodynamic activity. From the spectra in **Figure 16** one can see that P25 TiO_2 exhibited only a minimal intensity even after photoirradiation, whereas all thermally treated samples exhibited a much enhanced quartet after white light irradiation for 3 h within the magnetic field range of 3480 to

3540 G, in contrast to the profiles collected in the dark. The peak intensity ratio of 1:2:2:1 and a g value of 2.005 suggest the formation of hyrodxyl radicals (•OH),[61] and the •OH signals became intensified in the order of P25 TiO_2 < TiO_2-TF < TiO_2-200 ≈ TiO_2-300 < TiO_2-400 ≈ TiO_2-500 < TiO_2-600. This correlates well with the observed photodynamic activity, indcating that that hyrodxyl radicals (•OH) were indeed responsible for the antimcirobial activity. In Mott-Schottky analysis (**Figure 17**), all samples can be seen to exhibit a positive slope at various frequencies, indicating n-type semiconductor characteristics.[62] From linear regressions of the profiles, the flat-band potential (E_{fb}) can be estimated to be -0.60 V (vs. SHE) for P25 TiO_2, -1.06 V for TiO_2-TF, -1.23V for TiO_2-200, -0.99 V for TiO_2-300, -1.16 V for TiO_2-400, -1.10 V for TiO_2-500, and -0.72 V for TiO_2-600.[63]

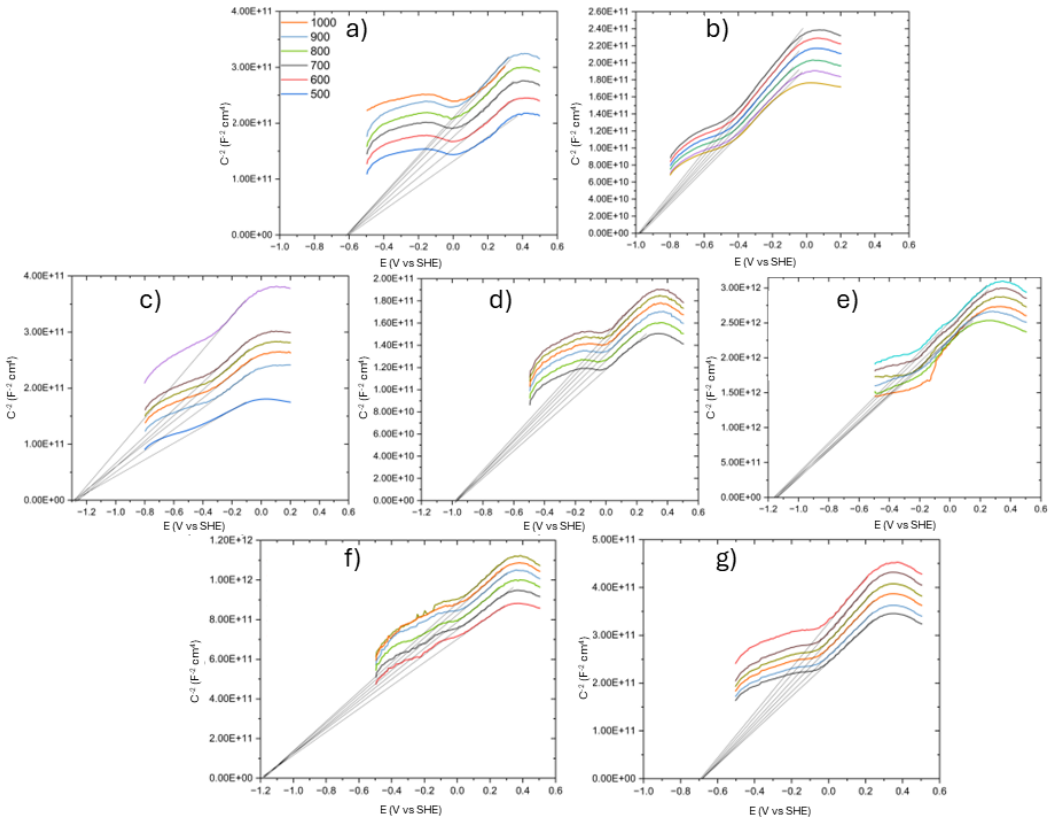

Figure 17. Mott Schottkey plots of the various samples at different frequencies: (a) P25, (b) TiO_2-TF, (c) TiO_2-200, (d) TiO_2-300, (e) TiO_2-400, (f) TiO_2-500, and (g) TiO_2-600.

In conjunction with the bandgaps estimated from the UV-vis measurements, the conduction band (CB)/valance band (VB) can be determined to be at -0.60/+2.73 V for P25 TiO_2, -1.06/+1.59 V for TiO_2-TF, -1.23/+1.76 V for TiO_2-200, -0.99/+1.58 V for TiO_2-300, -1.16/+0.92 V for TiO_2-400, -1.10/+1.19 V for TiO_2-500 and -0.72/+1.45 V for TiO_2-600, as illustrated in **Figure 9b** and listed in **Table 4**. Note that the VBs of the samples are all located at a less positive potential than the formal potential of water oxidation to •OH (E° = +2.74 V), suggesting that •OH would be unlikely to be produced

via water oxidation under photoirradiation; by contrast, the CBs are more negative than the formal potential of oxygen reduction to H_2O_2 ($E° = +0.70$ V) and H_2O_2 progression to •OH ($E° = +0.73$ V), suggesting that it is energetically favorable to produce such reactive oxygen species via oxygen reduction.[64-67]

Table 4. Calculated band energies of the sample series

Sample	**Band Gap (eV)**	**Conduction Band/Flat Band (V vs SHE)**	**Valance Band (V vs SHE)**
P25	3.33	-0.60	+2.73
TiO_2-TF	2.65	-1.06	+1.59
TiO_2-200	2.99	-1.23	+1.76
TiO_2-300	2.55	-0.99	+1.56
TiO_2-400	2.08	-1.16	+0.92
TiO_2-500	2.29	-1.10	+1.19
TiO_2-600	2.17	-0.72	+1.45

This is indeed supported by results from scavenger experiments with tert-butyl alcohol (TBA), thiourea, and nitro blue tetrazolium (NBT) that are known to effectively quench hydroxyl radicals,[68] hydroxyl radicals and hydrogen peroxide, and superoxide anions,[61] respectively. Specifically, in the absence of any scavenger, 39% of methyl blue was degraded by TiO2 -600 under visible light irradiation for 2 h. Yet, the degradation rate diminished drastically to ca. 19% upon the addition of TBA and 11% with thiourea,

whereas it only slightly to 34% with NBT (**Figure 18**). This indicates that hydroxyl radicals were likely the primary ROS produced via photocatalysis, with negligible contributions from superoxide anions.

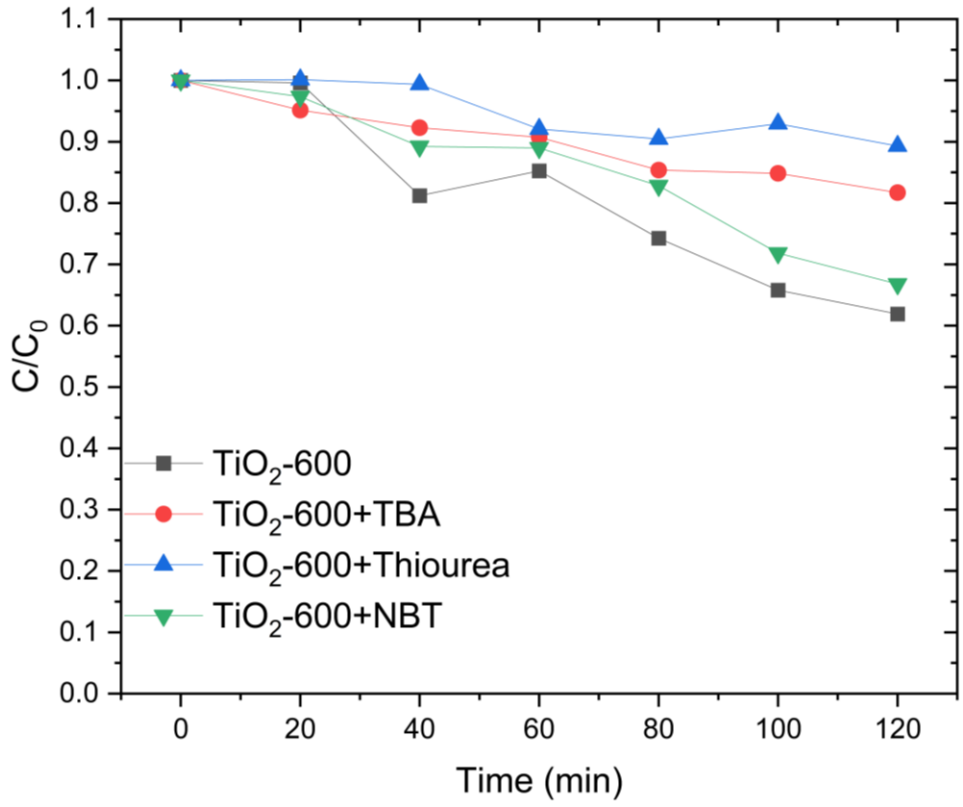

Figure 18. ROS scavenger testing in MB where 10mM of each scavenger was added to the 25ppm MB solution

In addition, the charge carrier density (N_d) can be calculated from the slope of the Mott-Schottky plots, where the TiO_2-600 sample can be found to possess the highest value of 9.5×10^{18} cm^{-3}, as compared to TiO_2-500 at 1.7×10^{18} cm^{-3}, TiO_2-400 at 7.9×10^{18} cm^{-3}, TiO_2-300 at 5.0×10^{18} cm^{-3}, TiO_2-200 at 1.3×10^{18} cm^{-3}, and P25 TiO_2 at 2.4×10^{18} cm^{-3}. It is likely that this discrepancy accounted for the different photodynamic

activities of the sample series, where a higher charge carrier density led to the formation of a higher concentration of •OH radicals.

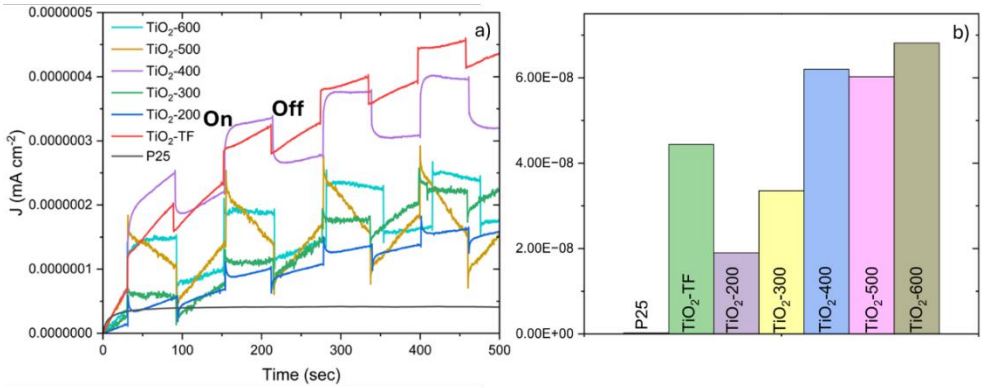

Figure 19. a) Transient photocurrents of the sample series under white light irradiation and b) extrapolated bar chart displaying the average of the induced photocurrents, measuring the difference in the currents 2 seconds before and 2 seconds after light exposure.

In fact, in transient photocurrent measurements (**Figure 19**), TiO_2-600 also displayed the greatest current response among the series. Additional contributions may arise from the enhanced hydrophicity of the samples,[69-71] which was conducive to sample dispersion in water and production of reactive oxygen species, as well as B doping that was shown to stabilize the Ti^{3+} species.[72]

4.4. Experimental Section

4.4.1 Chemicals

P25 titanium dioxide (TiO_2, Acros Organics), sodium borohydride ($NaBH_4$, 99%, Sigma-Aldrich), 5,5-dimethyl-1-pyrroline N-oxide (DMPO, Millipore Sigma), and methylene blue hydrate (MB, Acros Organics) were all used as received. Water was purified with a Barnstead Nanopure Water System (resistivity 18.3 MΩ cm).

4.4.2 Sample synthesis

In a typical synthesis, 200 mg of P25 TiO_2 was mixed with 75 mg of $NaBH_4$ in a mortar and pestle until the mixture was a uniform fine white powder. 50 mg of the mixture was placed on an iron sheet lined with graphitic paper, which was placed on a fire brick in a quartz tube. The assembly was purged with ultrahigh-purity argon for 10 min before MIH treatment at controlled induction currents (X = 200 to 600 A) for 12 s.[28-35] After heating, the samples were washed with water, ethanol, and acetone, until a clear supernatant was produced with no bubbles, and denoted as TiO_2-X. A control sample was also produced in a tube furnace, where the P25/$NaBH_4$ mixture was loaded onto a ceramic boat and heated in a tube furnace at a heating rate of 10 ºC min^{-1} in a nitrogen atmosphere at 450 °C for 2 h. The obtained sample, after being washed as outlined above, was referred to as TiO_2-TF.

4.4.3 Characterization

TEM images were acquired with a Tecni G2 operated at 200 kV. Raman measurements were conducted using a Horiba Jobin Yvon Lab-RAM ARAMIS automated scanning

confocal Raman microscope under 532 nm excitation. UV-vis absorption measurements were conducted with a Perkin-Elmer Lambda 35 spectrometer. XRD patterns were acquired with a Rigaku Smartlab diffractometer (Cu K_a radiation, l = 0.154 nm). XPS measurements were carried out with a Thermo Fisher K-alpha system, where the binding energy was calibrated against the C 1s peak. Contact angles were measured with a Tantec CAM-PLUS contact angle meter. Electron paramagnetic resonance (EPR) measurements were conducted at room temperature with a Bruker ElexSys E500 spectrometer operating at the X-band frequency (~9.8 GHz) using an ER 4122SHQE resonator. Experimentally, the TiO_2 samples obtained above were dispersed in water at a concentration of 1 mg mL^{-1}; and 63 mL of the dispersion was mixed with 7 mL of 1 M DMPO in water for a total volume of 70 mL, which was either wrapped in an aluminum foil to be left in the dark as controls or exposed to white light irradiation (100 W, 1000−1500 lumen with a peak emission of 365 nm, Dongguan Hongke Lighting Co., China) for 3 h before 10 mL of the dispersion was loaded into a 1.5 mm O.D. borosilicate capillary tube (Friedrich & Dimmock Borosilicate Capillary). The capillary tube was then positioned at the center of the cavity within the resonator for data collection, where spectra were collected at the microwave power of 20.03 mW, modulation amplitude of 1 G, modulation frequency of 100 kHz, and conversion time of 20.48 ms, and background-subtracted using a blank capillary tube containing only water.

4.4.4 Electrochemistry

Electrochemical measurements were carried out with a Gamry Reference 600 instrument in a three-electrode setup. The working electrode was a glassy carbon disk electrode with a surface area of 0.196 cm^2, a graphite rod was used as the counter electrode, Ag/AgCl as the reference electrode, and 0.5 M Na_2SO_4 as the supporting electrolyte. Mott-Schottky analysis was performed within the frequency range of 500 to 1000 Hz. Transient photocurrent measurements were performed at a constant potential of -0.25 V vs Ag/AgCl with and without white light photoirradiation.

4.4.5 Methylene blue degradation

In a typical experiment, 10 mg of the samples prepared above was added into 10 mL of a 25 ppm MB solution in water under magnetic stirring in the dark for 1 h to reach an adsorption-desorption equilibrium before the solution was exposed to white light photoirradiation. A series of aliquots (1 mL) was taken every 20 min, and the absorption spectra were acquired with a UV-vis spectrometer after centrifugation for 5 min to remove solid materials. The degradation activity was determined by normalizing the absorbance to that prior to photoirradiation.

4.4.6 Photochemical disinfection of water

E. coli cells were grown in Luria-Bertani (LB) agar in a 37 °C incubator. A single colony was selected and used to inoculate 3 mL of LB broth and allowed to shake at 37 °C for 18 h. The resulting liquid was centrifuged at 5000 rpm for 5 min and resuspended in phosphate buffered saline (PBS) 3 times before being diluted to an

optical density (OD) of 0.1 at 600 nm. Then 1 mL of the spiked PBS solution was diluted into 99 mL of sterile PBS, and 100 mL of this solution was added to 9.9 mL of PBS with 100 mg of the samples prepared above for a final concentration of 10 mg mL^{-1}. The vials containing the bacteria were then irradiated with white light for 3 h with 10 μL aliquots removed every 20 min and pipetted into a 96-well plate along with 200 μL of sterile LB broth. The 96-well plate was placed in a Molecular Device VERSA max microplate reader, where the OD was measured at 600 nm every 10 min with intermittent shaking between each reading over a 24 h incubation period at 37 °C. Growth curves seen in Figure 11 and Figure 12 are the averages of 3 tests with the standard deviations displayed as error bars.

4.4.7 Scanning electron microscopy

The change of E. coli morphology under photodynamic treatment was analyzed by scanning electron microscopy (SEM) measurements. Instead of being pipetted into the wells after 3 h of photoirradiation, the bacteria culture (5 μL) was dropcast onto an aluminum disk for imaging with a Thermo Scientific Apreo SEM instrument.

4.5. Conclusion

In this study, mixed-valance titanium (sub)oxides were produced by MIH-based ultrafast thermal treatment of P25 TiO_2 in the presence of $NaBH_4$. The resulting samples were found to consist of a mixed phase of TiO_2, Ti_4O_7 and Ti_2O_3 and exhibit a reduced band gap and enhanced visible light absorption, as compared to the pristine

P25 TiO_2. This allowed for effective white light photocatalysis. Notably as the TSO components increased with increasing induction currents (temperature), the photodynamic activity towards the inhibition of E. coli growth under visible light irradiation increased accordingly, due to the effective production of hyrodxyl radicals (•OH) from photocatalytic oxygen reduction. Results from this study showcase the capabilities of MIH in the ultrafast production of reduced metal oxides for high-performance catalysis.

4.6 References

(1) Fujishima, A.; Honda, K. Electrochemical Photolysis of Water at a Semiconductor Electrode. *Nature* **1972**, *238* (5358), 37-+.

(2) Aldosari, O. F. Photocatalytic water-splitting for hydrogen production using TiO2-based catalysts: Advances, current challenges, and future perspectives. *Catalysis Reviews* **2025**, 1-38.

(3) Bhom, F.; Isa, Y. M. Photocatalytic hydrogen production using TiO2-based catalysts: a review. *Global Challenges* **2024**, *8* (11), 2400134.

(4) Jung, H.; Cha, G.; Kim, H.; Will, J.; Zhou, X.; Spiecker, E.; Breu, J.; Schmuki, P. Ultrathin Ti-Deficient TiO2 Nanosheets with Pt Single Atoms Enable Efficient Photocatalytic Nitrate Reduction to Ammonia. *Journal of the American Chemical Society* **2025**, *147* (11), 9049-9055.

(5) Zhang, W.; He, H.; Li, H.; Duan, L.; Zu, L.; Zhai, Y.; Li, W.; Wang, L.; Fu, H.; Zhao, D. Visible-light responsive TiO2-based materials for efficient solar energy utilization. *Advanced Energy Materials* **2021**, *11* (15), 2003303.

(6) Rashid, R.; Shafiq, I.; Gilani, M. R. H. S.; Maaz, M.; Akhter, P.; Hussain, M.; Jeong, K.-E.; Kwon, E. E.; Bae, S.; Park, Y.-K. Advancements in TiO2-based photocatalysis for environmental remediation: Strategies for enhancing visible-light-driven activity. *Chemosphere* **2024**, *349*, 140703.

(7) Chen, S.; Hu, Y. H. Color TiO2 materials as emerging catalysts for visible-NIR light photocatalysis, a review. *Catalysis Reviews* **2024**, *66* (5), 1951-1991.

(8) Zhu, C.; Diao, Z.; Yang, Y.; Liao, J.; Wang, C.; Li, Y.; Liang, Z.; Xu, P.; Liu, X.; Zhang, Q. Recent advances and challenges in metal-based antimicrobial materials: a review of strategies to combat antibiotic resistance. *Journal of Nanobiotechnology* **2025**, *23* (1), 193.

(9) Zeng, H.; Gan, H.; Liu, Y.; Sun, B. The global disease burden attributable to unsafe water, sanitation, and handwashing with unqualified facilities from 1990 to 2019. *Journal of Global Health* **2024**, *14*, 04162.

(10) Andronic, L.; Enesca, A. Black TiO2 synthesis by chemical reduction methods for photocatalysis applications. *Frontiers in chemistry* **2020**, *8*, 565489.

(11) Kibar, M. E. Preparation of black-titanium dioxide nanotubes by thermal decomposition of sodium borohydride. *Journal of Advanced Research in Natural and Applied Sciences* **2021**, *7* (1), 71-81.

(12) Luo, M. Q.; Liu, H. J.; Yang, L. X.; Wang, W. J.; Zeng, C. L. Precisely dominating oxygen vacancy of Magneli phase titanium suboxides to efficiently remove quinolone antibiotics under visible light. *Separation and Purification Technology* **2024**, *341*, 126626.

(13) Fan, L.; Dong, Y.; Ismail, B. B.; Zhang, L.; Shi, Y.; Wu, D.; Wu, Y.; Li, G. The antimicrobial activity and resistance evolution of nanomaterials: A review. *ACS Materials Letters* **2025**, *7* (3), 1085-1111.

(14) Feizpoor, S.; Pouran, S. R.; Habibi-Yangjeh, A. Recent progress on photocatalytic evolution of hydrogen gas over TiO2-x-based emerging nanostructures. *Materials Science in Semiconductor Processing* **2023**, *162*, 107444.

(15) Khorashadizade, E.; Rahimi, K.; Mohajernia, S.; Hejazi, S.; Naseri, N.; Moradlou, O.; Moshfegh, A.; Schmuki, P. Comparing plasma reduction and thermal hydrogenation in oxygen deficient TiO2-x nanotubes for photoelectrochemical H2 production. *International Journal of Hydrogen Energy* **2024**, *74*, 434-446.

(16) Ekanayake, S. A.; Seeber, A.; Olorunyomi, J. F.; Mai, H.; Mahasivam, S.; Shah, D.; Lu, J.; Wen, X.; Sampath, N.; Schumann, S. L. Activated charcoal-mediated non-contact carbothermal reduction of TiO 2 for controlled synthesis of Magnéli phase titanium suboxides. *Journal of Materials Chemistry A* **2024**, *12* (24), 14734-14743.

(17) Kumar, A.; Barbhuiya, N. H.; Singh, S. P. Magneli phase titanium sub-oxides synthesis, fabrication and its application for environmental remediation: Current status and prospect. *Chemosphere* **2022**, *307*, 135878. DOI: ARTN 135878

10.1016/j.chemosphere.2022.135878.

(18) Zhao, X.; Zhang, X.; Zhao, B.; Jia, F.; Han, D.; Fan, Y.; Niu, L.; Ivaska, A. A direct oxygen vacancy essential Z-scheme C@ Ti4O7/g-C3N4 heterojunctions for visible-light degradation towards environmental dye pollutants. *Applied Surface Science* **2020**, *525*, 146486.

(19) Fang, W. Z.; Xing, M. Y.; Zhang, J. L. A new approach to prepare Ti3+ self-doped TiO2 via NaBH4 reduction and hydrochloric acid treatment. *Applied Catalysis B-Environmental* **2014**, *160*, 240-246. DOI: 10.1016/j.apcatb.2014.05.031.

(20) Han, Q.; Wang, L. J.; Li, J.; Dong, Y. X.; Ma, Y. B.; Zhang, J.; Yu, S. L. Built-in field-driven S-scheme boron-doped nanodiamond/TiO2(101)/ MXene photocatalyst for efficient antibiotic elimination: Mechanisms and DFT validation. *Chemical Engineering Journal* **2025**, *519*, 165290. DOI: ARTN 165290

10.1016/j.cej.2025.165290.

(21) Wang, Y.; Wang, X.; Li, L.; Wu, Y.; Yu, Q. An experimental and theoretical study on the photocatalytic antibacterial activity of boron-doped TiO2 nanoparticles. *Ceramics International* **2022**, *48* (1), 604-614.

(22) Hu, T.; Feng, P.; Guo, L.; Chu, H.; Liu, F. Construction of Built-In Electric Field in TiO2@ Ti2O3 Core-Shell Heterojunctions toward Optimized Photocatalytic Performance. *Nanomaterials* **2023**, *13* (14), 2125.

(23) Huang, J.; Huang, G.; Yin, J.; Yao, Y.; Zhang, P.; Li, M.; Feng, R.; Chen, N. Development of Ag/Ti3+/TiO2-Coated ceramic water filter for removing bacteria and organic pollutants. *Separation and Purification Technology* **2025**, *366*, 132677.

(24) Bletsa, E.; Merkl, P.; Thersleff, T.; Normark, S.; Henriques-Normark, B.; Sotiriou, G. A. Highly durable photocatalytic titanium suboxide–polymer nanocomposite films with visible light-triggered antibiofilm activity. *Chemical Engineering Journal* **2023**, *454*, 139971.

(25) Han, Q.; Wu, C.; Jiao, H.; Xu, R.; Wang, Y.; Xie, J.; Guo, Q.; Tang, J. Rational design of high-concentration Ti3+ in porous carbon-doped TiO2 nanosheets for efficient photocatalytic ammonia synthesis. *Advanced Materials* **2021**, *33* (9), 2008180.

(26) Yu, M.; Saunders, T.; Grasso, S.; Mahajan, A.; Zhang, H. F.; Reece, M. J. Magneli phase titanium suboxides by Flash Spark Plasma Sintering. *Scripta Materialia* **2018**, *146*, 241-245. DOI: 10.1016/j.scriptamat.2017.11.044.

(27) Liu, M.; Jhulki, S.; Sun, Z.; Magasinski, A.; Hendrix, C.; Yushin, G. Atom-economic synthesis of Magnéli phase Ti4O7 microspheres for improved sulfur cathodes for Li–S batteries. *Nano Energy* **2021**, *79*, 105428.

(28) Liu, Q. M.; Chen, S. W. Ultrafast synthesis of electrocatalysts. *Trends Chem* **2022**, *4* (10), 918-934. DOI: 10.1016/j.trechm.2022.07.004.

(29) Lu, B. Z.; Liu, Q. M.; Wang, C. Y.; Masood, Z.; Morris, D. J.; Nichols, F.; Mercado, R.; Zhang, P.; Ge, Q. F.; Xin, H. L. L.; et al. Ultrafast Preparation of Nonequilibrium FeNi Spinels by Magnetic Induction Heating for Unprecedented Oxygen Evolution Electrocatalysis. *Research* **2022**, *2022*, 9756983. DOI: 10.34133/2022/9756983.

(30) Liu, Q. M.; Lu, B. Z.; Nichols, F.; Ko, J.; Mercado, R.; Bridges, F.; Chen, S. W. Rapid preparation of carbon-supported ruthenium nanoparticles by magnetic induction

heating for efficient hydrogen evolution reaction in both acidic and alkaline media. *SusMat* **2022**, *2*, 335-346. DOI: https://doi.org/10.1002/sus2.66.

(31) Liu, Q. M.; McNair, S.; Nichols, F.; Lu, B. Z.; Yu, B. Z.; Pan, D. J.; Ko, J. B., A.; Bridges, F.; Chen, S. W. Ultrafast synthesis of cobalt/carbon nanocomposites by magnetic induction heating for oxygen evolution reaction. *Advanced Sensor and Energy Materials* **2023**, *2*, 100046. DOI: 10.1016/j.asems.2023.100046.

(32) Liu, Q. M.; Nichols, F.; Bhuller, A.; Singewald, K.; Kuo, H. L.; Lu, J. Q.; Millhauser, G. L.; Bridges, F.; Ge, Q. F.; Chen, S. W. Ultrafast synthesis of amorphous molybdenum sulfide by magnetic induction heating for hydrogen evolution reaction. *Applied Catalysis B-Environment and Energy* **2024**, *342*, 123399. DOI: 10.1016/j.apcatb.2023.123399.

(33) Yu, B. Z.; Liu, Q. M.; Pan, D. J.; Singewald, K.; Dubois, D.; Tressel, J.; Hou, B. Y.; Millhauser, G. L.; Bridges, F.; Chen, S. W. Ultrafast preparation of ruthenium nanoparticle/molybdenum oxide/nitrogen-doped carbon nanocomposites by magnetic induction heating for efficient hydrogen evolution reaction. *J Mater Chem A* **2024**, *12* (26), 16087-16097. DOI: 10.1039/d4ta00884g.

(34) Pan, D. J.; Liu, Q. M.; Yu, B. Z.; DuBois, D. B.; Tressel, J.; Yu, S.; Kaleekal, N.; Trabanino, S.; Jeon, Y.; Bridges, F.; et al. Rapid Synthesis of Ruthenium-Copper Nanocomposites as High-Performance Bifunctional Electrocatalysts for Electrochemical Water Splitting. *Small* **2024**, 2404729. DOI: 10.1002/smll.202404729.

(35) Pan, D. J.; Yu, B. Z.; Tressel, J.; Yu, S. R.; Saravanan, P.; Sangoram, N.; Ornelas-Perez, A.; Bridges, F.; Chen, S. W. Rapid Synthesis of Carbon-Supported Ru-RuO2

Heterostructures for Efficient Electrochemical Water Splitting. *Advanced Science* **2025**, *12*, 2414534. DOI: 10.1002/advs.202414534.

(36) Ohno, T.; Sarukawa, K.; Tokieda, K.; Matsumura, M. Morphology of a TiO2 photocatalyst (Degussa, P-25) consisting of anatase and rutile crystalline phases. *Journal of Catalysis* **2001**, *203* (1), 82-86. DOI: 10.1006/jcat.2001.3316.

(37) Wang, G. R.; Liu, Y.; Ye, J. W.; Yang, X. J.; Lin, Z. F. Formation mechanism of Ti4O7 phase prepared by carbothermal reduction reaction. *Journal of the American Ceramic Society* **2020**, *103* (6), 3871-3879. DOI: 10.1111/jace.17045.

(38) Badr, H. O.; Lagunas, F.; Autrey, D. E.; Cope, J.; Kono, T.; Torita, T.; Klie, R. F.; Hu, Y.-J.; Barsoum, M. W. On the structure of one-dimensional TiO2 lepidocrocite. *Matter* **2023**, *6* (1), 128-141.

(39) Huang, H. L.; Wang, C.; Li, Q.; Wang, R. Q.; Yang, Y. Y.; Muhetaer, A.; Huang, F. Q.; Han, B.; Xu, D. S. Efficient and Full-Spectrum Photothermal Dehydrogenation of Ammonia Borane for Low-Temperature Release of Hydrogen. *Advanced Functional Materials* **2021**, *31* (8), 2007591. DOI: ARTN 2007591

10.1002/adfm.202007591.

(40) Kang, X. W.; Chen, S. W. Photocatalytic reduction of methylene blue by TiO2 nanotube arrays: effects of TiO2 crystalline phase. *Journal of Materials Science* **2010**, *45* (10), 2696-2702.

(41) Aswathappa, S.; Dai, L.; Sathiyadhas, S. J. D.; Kumar, R. S.; Almansour, A. I.; Freire, P. T. C.; Athiruban, S.; Kang, G. Quantitative analysis of anatase-rutile mixtures of TiO2 employing X-ray diffractometry and visible-Raman spectroscopy at normal

heating and superheating conditions-Implications and limitations of the Spurr-Mayers equation. *Ceramics International* **2025**.

(42) Aswathappa, S.; Dai, L.; Dhas, S. S. J.; Kumar, R. S.; Palaniyasan, E. Size-dependent anatase to rutile phase transition under acoustic shocked conditions–A case study of TiO2 bulk and nanoparticles. *Applied Surface Science* **2025**, *681*, 161501.

(43) Yao, S.; Xue, S.; Zhang, Y.; Shen, X.; Qian, X.; Li, T.; Xiao, K.; Qin, S.; Xiang, J. Synthesis, characterization, and electrochemical performance of spherical nanostructure of Magnéli phase Ti4O7. *Journal of Materials Science: Materials in Electronics* **2017**, *28* (10), 7264-7270.

(44) Lin, H.; Xiao, R.; Xie, R.; Yang, L.; Tang, C.; Wang, R.; Chen, J.; Lv, S.; Huang, Q. Defect engineering on a Ti4O7 electrode by Ce3+ doping for the efficient electrooxidation of perfluorooctanesulfonate. *Environmental Science & Technology* **2021**, *55* (4), 2597-2607.

(45) Yuan, T.; Wei, W.; Wang, Y.; Jin, N.; Ye, J. Effect of V-doping on structure and electrical conductivity of Magnéli phase Ti4O7. *Journal of Alloys and Compounds* **2024**, *978*, 173492.

(46) Verma, R.; Gangwar, J.; Srivastava, A. K. Multiphase TiO 2 nanostructures: A review of efficient synthesis, growth mechanism, probing capabilities, and applications in bio-safety and health. *RSC advances* **2017**, *7* (70), 44199-44224.

(47) Wang, J.; Li, Y.; Deng, L.; Wei, N.; Weng, Y.; Dong, S.; Qi, D.; Qiu, J.; Chen, X.; Wu, T. High-performance photothermal conversion of narrow-bandgap Ti2O3 nanoparticles. *Advanced Materials* **2017**, *29* (3), 1603730.

(48) Li, Y.; Weng, Y.; Yin, X.; Yu, X.; Kumar, S. R. S.; Wehbe, N.; Wu, H.; Alshareef, H. N.; Pennycook, S. J.; Breese, M. B. H. Orthorhombic Ti2O3: a polymorph-dependent narrow-bandgap ferromagnetic oxide. *Advanced Functional Materials* **2018**, *28* (7), 1705657.

(49) Azer, B. B.; Gulsaran, A.; Pennings, J. R.; Karimi, R.; Belgabad, A. A.; Xu, A. H.; Zaidan, L.; Kocer, S.; Sanderson, J.; Bajcsy, M. Core–shell defective TiO 2 nanoparticles by femtosecond laser irradiation with enhanced photocatalytic performance. *Materials Advances* **2023**, *4* (5), 1297-1305.

(50) Pan, X.; Yang, M.-Q.; Fu, X.; Zhang, N.; Xu, Y.-J. Defective TiO 2 with oxygen vacancies: synthesis, properties and photocatalytic applications. *Nanoscale* **2013**, *5* (9), 3601-3614.

(51) Varnagiris, S.; Medvids, A.; Lelis, M.; Milcius, D.; Antuzevics, A. Black carbon-doped TiO2 films: Synthesis, characterization and photocatalysis. *Journal of Photochemistry and Photobiology A: Chemistry* **2019**, *382*, 111941.

(52) Katal, R.; Salehi, M.; Davood Abadi Farahani, M. H.; Masudy-Panah, S.; Ong, S. L.; Hu, J. Preparation of a new type of black TiO2 under a vacuum atmosphere for sunlight photocatalysis. *ACS applied materials & interfaces* **2018**, *10* (41), 35316-35326.

(53) Guo, X.; Li, C.; Zhou, Y.; Chen, Y.; Deng, W.; Li, R. Ti2O3 (H2PO4) 2· 2H2O as a Novel Intercalated Anode for Ultralong Lifespan “Rocking-Chair” Aqueous Zinc-Ion Batteries. *Angewandte Chemie International Edition* **2025**, *64* (22), e202502446.

(54) Salcedo-Abraira, P.; Babaryk, A. A.; Montero-Lanzuela, E.; Contreras-Almengor, O. R.; Cabrero-Antonino, M.; Grape, E. S.; Willhammar, T.; Navalón, S.; Elkäim, E.; García, H. A novel porous Ti-squarate as efficient photocatalyst in the overall water splitting reaction under simulated Sunlight irradiation. *Advanced Materials* **2021**, *33* (52), 2106627.

(55) Quesada-González, M.; Boscher, N. D.; Carmalt, C. J.; Parkin, I. P. Interstitial boron-doped TiO2 thin films: the significant effect of boron on TiO2 coatings grown by atmospheric pressure chemical vapor deposition. *ACS applied materials & interfaces* **2016**, *8* (38), 25024-25029.

(56) Feng, N.; Liu, F.; Huang, M.; Zheng, A.; Wang, Q.; Chen, T.; Cao, G.; Xu, J.; Fan, J.; Deng, F. Unravelling the efficient photocatalytic activity of boron-induced Ti3+ species in the surface layer of TiO2. *Scientific reports* **2016**, *6* (1), 34765.

(57) Niu, P.; Wu, G.; Chen, P.; Zheng, H.; Cao, Q.; Jiang, H. Optimization of boron doped TiO2 as an efficient visible light-driven photocatalyst for organic dye degradation with high reusability. *Frontiers in Chemistry* **2020**, *8*, 172.

(58) Jia, H.; Shang, H.; He, Y.; Gu, S.; Li, S.; Wang, Q.; Wang, S.; Peng, J.; Feng, X.; Li, P. Engineering the defect distribution via boron doping in amorphous TiO2 for robust photocatalytic NO removal. *Applied Catalysis B: Environment and Energy* **2024**, *356*, 124239.

(59) Tauc, J.; Grigorovici, R.; Vancu, A. Optical Properties and Electronic Structure of Amorphous Germanium. *Phys Status Solidi* **1966**, *15* (2), 627-+. DOI: DOI 10.1002/pssb.19660150224.

(60) Makula, P.; Pacia, M.; Macyk, W. How To Correctly Determine the Band Gap Energy of Modified Semiconductor Photocatalysts Based on UV-Vis Spectra. *Journal of Physical Chemistry Letters* **2018**, *9* (23), 6814-6817. DOI: 10.1021/acs.jpclett.8b02892.

(61) Dubois, D. B.; Tressel, J.; Hergenroeder, D.; Jones, C.; Yu, B. Z.; Singewald, K.; Millhauser, G. L.; Saltikov, C.; Chen, S. W. Antibacterial activity of bismuth tungstate against Escherichia coli: Enhanced piezocatalysis by morphological engineering. *J Environ Chem Eng* **2025**, *13* (5), 118871. DOI: ARTN 118871

10.1016/j.jece.2025.118871.

(62) Wu, R. J.; Gao, S.; Jones, C.; Sun, M. M.; Guo, M.; Tai, R.; Chen, S. W.; Wang, Q. Bi/BSO Heterojunctions via Vacancy Engineering for Efficient Photocatalytic Nitrogen Fixation. *Advanced Functional Materials* **2024**, *34* (24), 2314051. DOI: ARTN 2314051

10.1002/adfm.202314051.

(63) Koshevoy, E.; Gribov, E.; Lyulyukin, M.; Selishchev, D.; Kozlov, D. Photoelectrochemical study of M/TiO2 (M = Pt, Pd, Au) supported catalysts: flat-band potentials and photoelectrocatalytic properties in glycerol oxidation reaction. *Journal of Photochemistry and Photobiology a-Chemistry* **2026**, *471*, 116678. DOI: ARTN 116678

10.1016/j.jphotochem.2025.116678.

(64) Koppenol, W. H.; Butler, J. Energetics of interconversion reactions of oxyradicals. *Advances in Free Radical Biology & Medicine* **1985**, *1* (1), 91-131.

(65) Nosaka, Y.; Nosaka, A. Understanding hydroxyl radical (• OH) generation processes in photocatalysis. *ACS Energy Letters* **2016**, *1* (2), 356-359.

(66) Cheng, K.; Li, H.; Laszakovits, J. R.; Sharpless, C. M.; Rosario-Ortiz, F.; McKay, G. Probing the photochemical formation of hydroxyl radical from dissolved organic matter: insights into the H2O2-dependent pathway. *Environmental Science & Technology* **2025**, *59* (4), 2245-2256.

(67) Chata, G.; Nichols, F.; Mercado, R.; Assafa, T.; Millhauser, G. L.; Saltikov, C.; Chen, S. W. Photodynamic Activity of Graphene Oxide/Polyaniline/Manganese Oxide Ternary Composites toward Both Gram-Positive and Gram-Negative Bacteria. *Acs Appl Bio Mater* **2021**, *4* (9), 7025-7033. DOI: 10.1021/acsabm.1c00677.

(68) Liu, Q.; Peng, Y.; Masood, Z.; DuBois, D.; Tressel, J.; Nichols, F.; Ashby, P.; Mercado, R.; Assafa, T.; Pan, D. Stable Cuprous Hydroxide Nanostructures by Organic Ligand Functionalization. *Advanced Materials* **2023**, *35* (8), 2208665.

(69) Wang, R.; Hashimoto, K.; Fujishima, A.; Chikuni, M.; Kojima, E.; Kitamura, A.; Shimohigoshi, M.; Watanabe, T. Light-induced amphiphilic surfaces. *Nature* **1997**, *388* (6641), 431-432.

(70) Yu, Y.; Cui, W.; Song, L.; Liao, Q.; Ma, K.; Zhong, S.; Yue, H.; Liang, B. Design of organic-free superhydrophobic TiO2 with ultraviolet stability or ultraviolet-induced switchable wettability. *ACS Applied Materials & Interfaces* **2022**, *14* (7), 9864-9872.

(71) Deshpande, R. A.; Navne, J.; Adelmark, M. V.; Shkondin, E.; Crovetto, A.; Hansen, O.; Bachmann, J.; Taboryski, R. Understanding the light induced hydrophilicity of metal-oxide thin films. *Nature Communications* **2024**, *15* (1), 124.

(72) Han, Q.; Wang, L.; Li, J.; Dong, Y.; Ma, Y.; Zhang, J.; Yu, S. Built-in field-driven S-scheme boron-doped nanodiamond/TiO2 (101)/MXene photocatalyst for efficient antibiotic elimination: Mechanisms and DFT validation. *Chemical Engineering Journal* **2025**, 165290.

Chapter 5 Ultrafast Synthesis of Copper doped Titanium Suboxide via Magnetic Induction Heating for Enhanced Piezocatalytic Activity

5.1 Abstract

Increasing environmental concerns about industrial wastewater demand new water treatment technologies. A viable solution to this is the development of potent piezocatalytic materials, capable of utilizing the ubiquitous mechanical energy to achieve high antibacterial and water disinfection activity. In this study, Cu-doped titanium dioxide (CuTiO) nanoparticles are first prepared by hydrothermal treatment of titanium butoxides in the presence of a calculated amount of cupric nitrate followed by thermal annealing in ambient condition. Subsequent treatment by magnetic induction heating in the presence of sodium borohydride leads to the production of copper oxide/titanium suboxides (CubTiO), which exhibit markedly enhanced piezoelectric properties, and the sample prepared at a Cu:Ti feed ratio of 4% (4%CubTiO) stands out with the highest piezoelectric coefficient (d_{33}) of 92 pC N^{-1}, due to the formation of CuO/TiO_{2-x} heterojunctions. Under ultrasonic stimulation, the 4%CubTiO sample effectively produces reactive oxygen species, such as superoxide anions and hydroxyl radicals, as confirmed by electron paramagnetic resonance measurements. This property can be exploited for the eradication of waterborne pathogenic bacteria like *Escherichia coli*, where the growth of bacterial cells is inhibited completely by 4%CubTiO in under 60 min of sonication. Such a performance is drastically higher than those with various other metal precursors. Results from this work highlight the unique significance of structural engineering in enhancing the piezocatalytic activity of titanium suboxide nanostructures for antimicrobial applications.

5.2. Introduction

With the explosion of industrial growth over the last century a corresponding wave of industrial water contamination has followed. With the traditional water treatment options being effective but costly, it is imperative to develop next-generation water treatment agents where multiple actions can work collectively to inhibit bacterial growth and remove harmful chemical byproducts.[1, 2] Towards this end, piezoelectric catalysis (piezocatalysis), which is based on materials with non-centrosymmetric crystal structures that can convert mechanical energy into piezoelectricity, has emerged as a viable technology for water disinfection. This works by utilizing the generated piezoelectric charge to drive a cascade of chemical reactions, such as the formation of reactive oxygen species (ROS),[3, 4] which are well-known potent agents that can compromise the structural integrity of bacterial cell membranes, disrupt bacterial replication, and readily result in total bacterial inhibition.[4-6] Towards this end, a wide range of piezoelectric oxide materials have been used for antimicrobial applications. Among these, whereas titanium dioxide (TiO_2) is generally not known as a piezoelectric material due to a centrosymmetric crystal structure, the introduction of structural defects can break the centrosymmetry, leading to a markedly enhanced piezoelectric activity. For instance, Xia et al.[7] prepared defective rutile TiO_2 nanoparticles by etching away the [MgO_6] octahedra from $MgTiO_3$ using NH_4Cl molten salt. The sample exhibited a lattice distortion and a piezoelectric coefficient (d_{33}) of 41.6 pm V^{-1} and was capable of degrading 96% of tetracycline hydrochloride after sonication for 1 h due to the generation of superoxide radicals. Titanium suboxides

(TSOs), the less commonly formed oxide species, have also shown great promise but have had comparatively limited investigations. TSOs are commonly prepared by chemical reduction of TiO_2 producing a mixed oxidation state of Ti^{4+} and Ti^{3+}.[8-10] In the resultant substoichiometric TiO_{2-x}, the structural defects (e.g., oxygen vacancies) can lower the bandgap, increase visible light absorption, and importantly for piezoelectric applications form a non-centrosymmetric crystal structure.[11, 12] Nevertheless, Ti^{3+} species are prone to oxidation when exposed to air, and need to be stabilized by appropriate structural engineering, such as formation of heterojunctions and heteroatom doping. For instance, Han et al.[13] prepared black TiO_{2-x} via the partial reduction of TiO_2 with aluminum that featured a distorted TiO_2/TiO_{2-x} core/shell structure. Here the reduced outer layer was highlighted as vital for the formation of ROS because of its abundance of oxygen vacancies, and with the remarkable biocompatibility, the black TiO_{2-x} could be used for in vivo sonodynamic and photodynamic therapy as manifested in complete tumor eradication after just 10 min of combined piezocatalytic and photocatalytic treatment. In another study, Zhang et al.[14] synthesized Co_3O_4@TiO_{2-x} core@shell composites via solvothermal mixing and $NaBH_4$ reduction which exhibited Z-scheme heterojunctions and a mixed oxidation state of both metal species (Ti^{4+}/Ti^{3+} and Co^{3+}/Co^{2+}). This facilitated the donation of electrons from TiO_{2-x} to Co_3O_4 and the efficient generation of both hydroxyl radicals and singlet oxygen under sonodynamic activation, a unique property that was exploited for the almost complete inhibition of tumor growth after just 5 min's sonication. Wang et al.[15] employed a laser fusion technique to prepare metal-deficient TiO_2/barium

titanate ($BaTiO_3$) heterostructures for sonodynamic therapy, where the rich Ti^{3+} species helped narrow the band gap and expedite electron transfer within the sample. In fact, the surface potential was found to increase to -166.12 mV under sonication from -157.12 mV in the absence of sonication, suggesting that the acoustically excited electros were accumulated on the sample surface. In in vivo studies it was found that the heterostructure eradicated over 99% of *Staphylococcus aures* in mice under sonication for 20 min, in comparison to ca. 77% with nondefective TiO_2.

In this study, copper-doped titanium oxide nanoparticles were first prepared via a hydrothermal procedure using titanium butoxide and cupric nitrate as the precursors. Subsequent treatment with magnetic induction heating (MIH) in the presence of $NaBH_4$ led to the formation of CubTiO heterojunction composites consisting of nanocrystalline CuO and TSOs in intimate contact. This was to take advantage of the instant generation of an eddy current when a conductor was immersed into a magnetic field that could heat up the substrate to a temperature over 1000 ºC within seconds.[16-22] It was found that the formation of CuO and TSO heterojunctions dramatically increased the piezoelectric properties, and the sample prepared at 4% Cu to Ti feed ratio exhibited the highest piezoelectric coefficient (d_{33}) of 92 pC N^{-1} among the series. Under 37 kHz ultrasonic stimulation, the 4%CubTiO sample exhibited a markedly enhanced antibacterial activity towards *Escherichia coli* (*E. coli*), with complete bacterial inhibition in less than 1 h, as compared to other samples at different Cu dopant concentrations and with different metal dopants. This was ascribed to the efficient

piezocatalytic production of ROS like superoxide and hydroxyl radicals, as confirmed in EPR measurements.

5.3 Results and Discussion

5.3.1 Structural Characterization

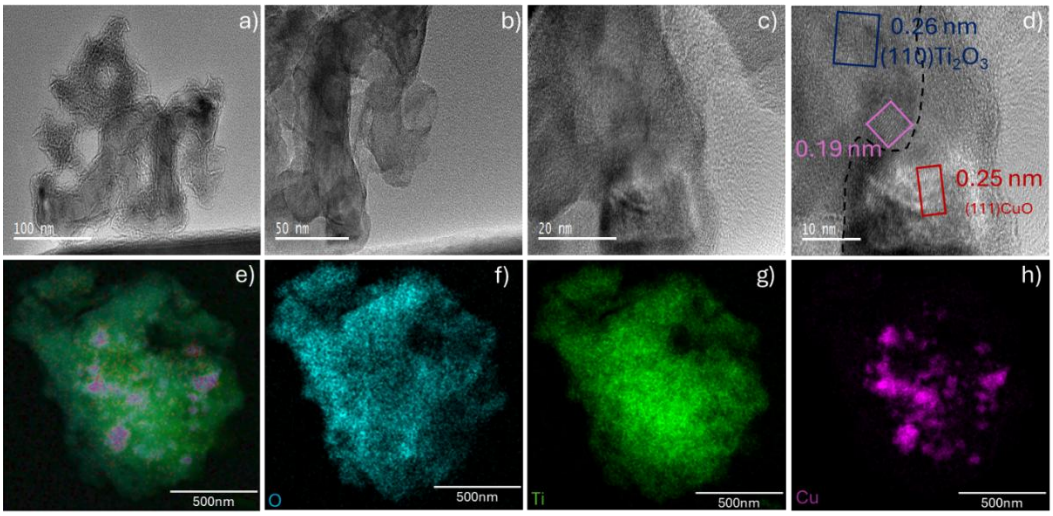

Figure 1. (a-d) Bright-field TEM images of 4%CubTiO at different magnifications. Scale bars are (a) 100 nm, (b) 50 nm, (c) 20 nm, and (d) 10 nm. STEM image and EDS-based elemental maps of (e) all elements, (f) O, (g) Ti, and (h) Cu. Scale bars are all 500 nm.

The sample structures were first examined by TEM measurements (**Figure 1a-c**). One can see that the 4%CubTiO sample consisted primarily of irregular particles about 50 nm in size that clumped together into large agglomerates of around 200 nm. In high-resolution TEM measurements (**Figure 1d**) the sample can be seen to exhibit nanocrystalline domains with clearly-defined lattice fringes featuring three interplanar

spacings of 1.9, 2.5 and 2.6 Å. The first can be attributed to the mix of the anatase TiO_2(200) and CuO(112), the second to the CuO (111) and the third to the Ti_2O_3(110) planes.[23-25] In the fast Fourier transform (FFT) patterns (**Figure 2a**), the Ti_2O_3 (006), (113), (110), and $(11\bar{6})$ planes can be readily resolved, confirming the successful formation of Ti_2O_3 by $NaBH_4$ reduction,[26] while the CuO patterns (**Figure 2b**) of (110) and (020) further confirmed the formation of a crystaline heterostructure.

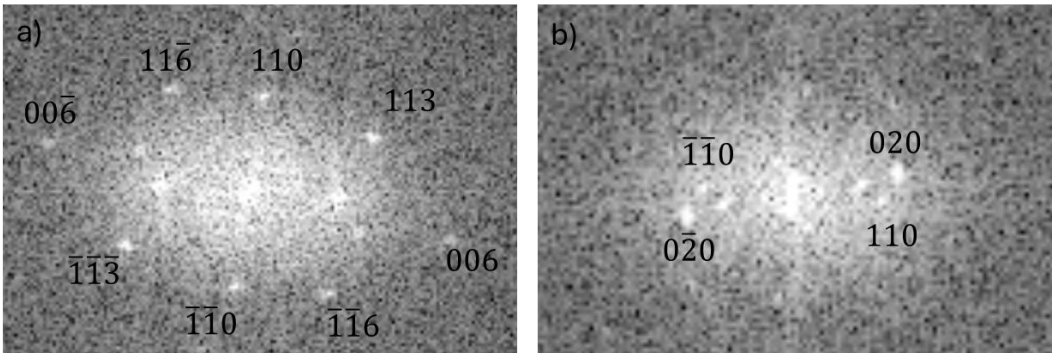

Figure 2. FFT images of corresponding highlighted areas in Figure 1d for (a) Ti_2O_3 and (b) CuO

In the elemental mapping analysis based on energy-dispersive X-ray spectroscopy (EDS) (**Figure 1e-h**), the elements of Ti and O can be seen to exhibit an even distibution across the sample, whereas the Cu signals were more discrete and largely confined within nanoparticulates, in good agreement with the formation of CuO-Ti_2O_3 heterojunctions.

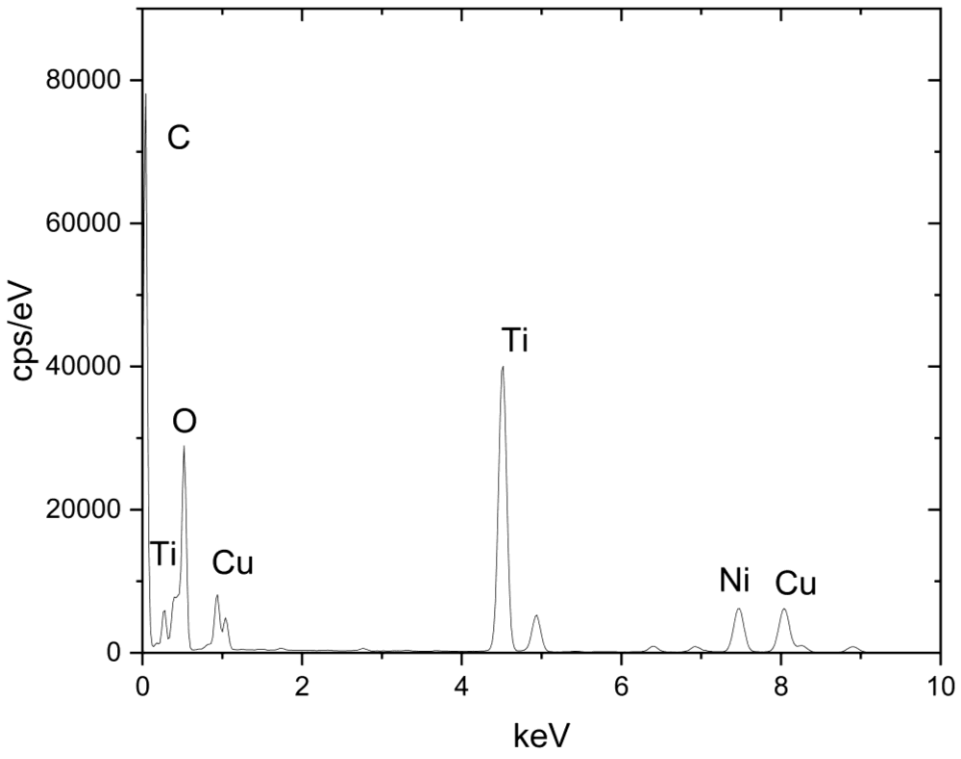

Figure 3. EDS spectrum of 4%CubTiO in Figure 1.

In addition, from the EDS profile (**Figure 3**), the elemental contents can be estimated to be ca. 64.2 at% for O, 33.7 at% for Ti, and 2.1 at% for Cu, largely in line with the initial Cu:Ti feed ratio.

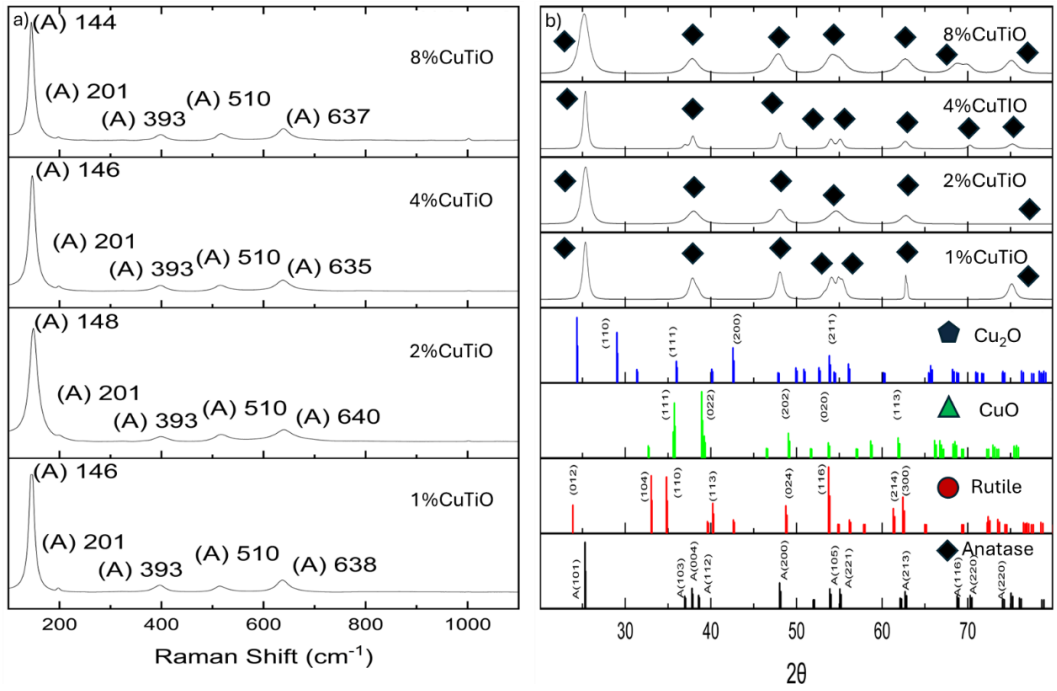

Figure 4. (a) Raman spectra and (b) XRD patterns of the sample series before $NaBH_4$ reduction.

Raman spectroscopy measurements were then carried out to further determine the structural characteristics. From **Figure 4a**, one can see that the (pre-reduced) CuTiO samples all exhibited five vibrational bands characteristic of anatase TiO_2, with the dominant lattice vibration at 144 cm^{-1} (E_g, which overlaps with the B_{1g} vibration of rutile TiO_2), O-Ti-O symmetric bending of O around Ti centers at 198 cm^{-1} (E_g), O-Ti-O asymmetric bending within the TiO_6 octahedra at 394 cm^{-1} (B_{1g}), O-Ti-O symmetric and asymmetric stretching at 516 cm^{-1} (A_{1g}+B_{1g}), and Ti-O symmetric stretching at 636 cm^{-1} (E_g).[27, 28]

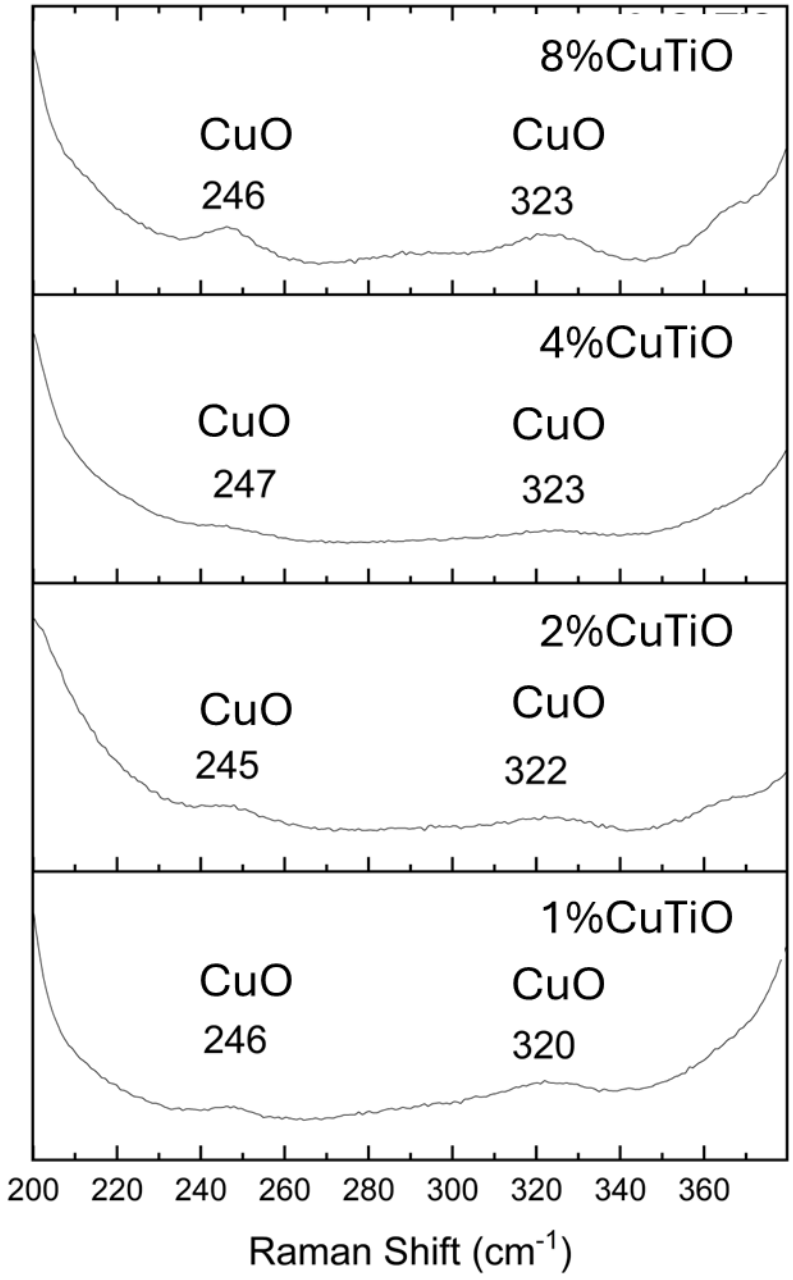

Figure 5. Zoomed-in Raman spectra of the prereduction samples to highlight the Cu oxide peaks.

In addition, two broad vibrations can be identified at ca. 245 and 322 cm^{-1} that can be attributed to the A_g and B_{g1} modes of CuO, respectively, and the peaks became increasingly intensified with increasing Cu doping (**Figure 5**),[29] indicating that the samples consisted of a mix of CuO and (anatase) TiO_2.

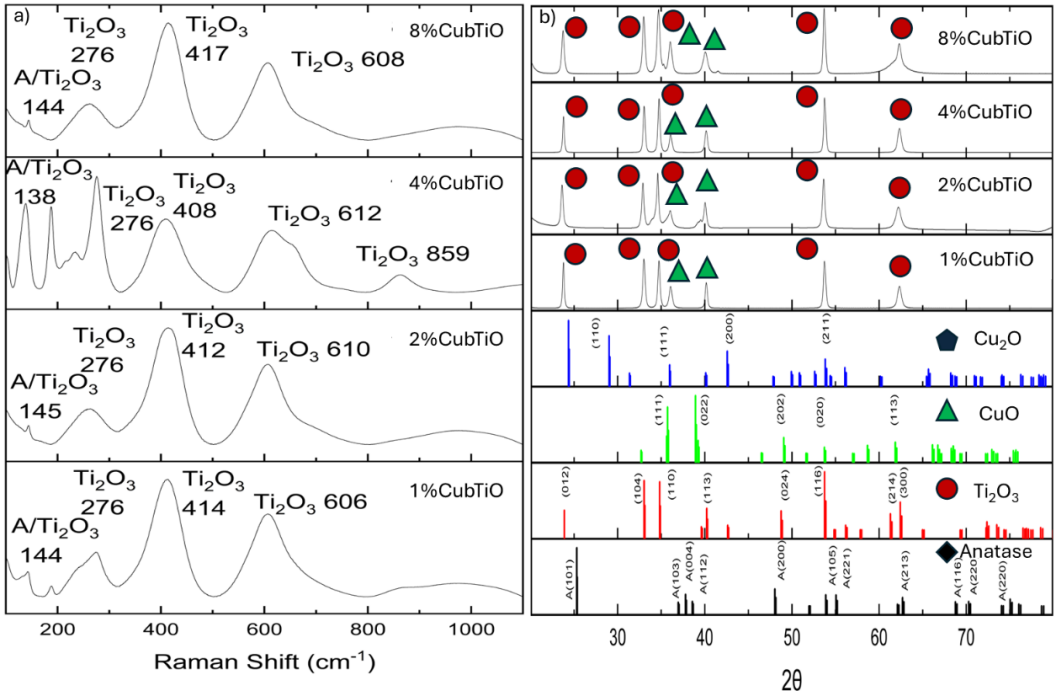

Figure 6. Raman spectra (a) and XRD (b) of the sample series after $NaBH_4$ reduction

Notably, after MIH reduction (**Figure 6a**), the CubTiO samples exhibited a dramatic shift of the Raman features, with the dominate peaks near 415 and 610 cm^{-1} that are in good alignment with the A_{1g} and E_g modes of the Ti-O stretches of corundum-type Ti_2O_3.[30-32] Additional minor suboxide peaks can be seen at ca. 203 and 272 cm^{-1}, along with the remaining small anatase peak of 145 cm^{-1}.[33, 34] However, due to the rise of these new suboxide peaks the CuO peaks now became indistinguishable. Nevertheless,

these results suggest the effective reduction of the CuTiO samples to TSOs in CubTiO.[35] Notably the copper addition and reductions could be seen visibly in the samples as well (**Figure 7)**.

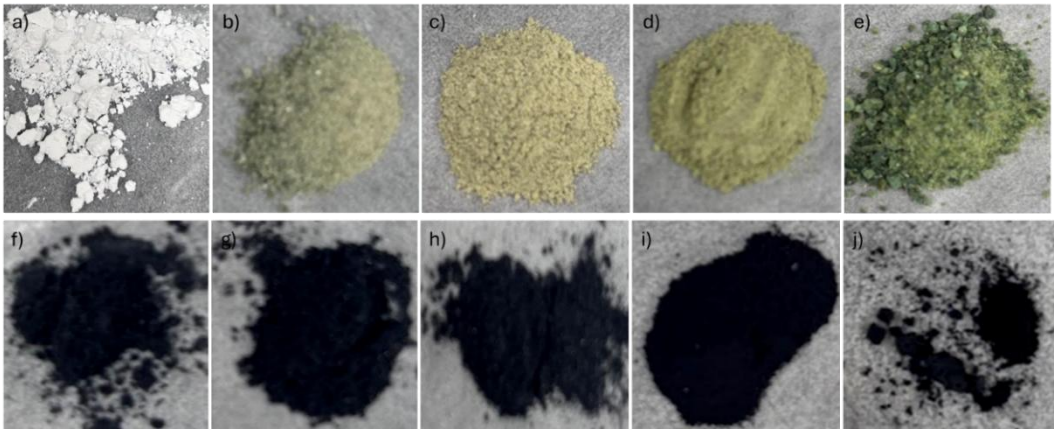

Figure 7. Photographs of sample series (a) TiO, (b) 1%CuTiO, (c) 2%CuTiO, (d) 4%CuTiO, (e) 8%CuTiO, (f) bTiO, (g) 1%CubTiO, (h) 2%CubTiO, (i) 4%CubTiO, and (j) 8%CubTiO

It can be seen that the TiO sample exhibited an ashen color, whereas the 1%CuTiO took on a faint green color and then the 2%CuTiO was darker green brown, and the 4%CuTiO and 8%CuTio became progressively darker and browner. By contrast, the reduced samples (CubTiO) all displayed a dark brown/black shade and were not clearly distinguishable from each other.

Consistent results were obtained from XRD measurements. From **Figure 4b**, one can see that the diffraction patterns of the CuTiO sample series closely match those of anatase TiO_2 (A, JCPDS #21-1272), with the primary (101) peak at 2q = 24.5º. This closely corroborates what was seen in the above Raman measurements and confirms

the successful formation of TiO_2 nanoparticles. While no Cu-related diffraction patterns can be identified, the TiO_2 peaks can be seen to exhibit increasing boradening with increasing Cu feeds, likely due to an increase of the lattice defects. Upon MIH treatment (**Figure 6b**), a clear pattern shift occurred mirroring what was seen in the Raman spectra, with the emergence of new dominant features of a doublet at 33.1º (104)/34.8º (110) and a large sinlge peak at 53.7º (116) that are in line with the strucutre of corundum-type Ti_2O_3 (JCPDS #44-1294). This backs up what was seen in the Raman measurments and confirms the successful reduction during the MIH step.[35] Additionally, a peak can still be seen at ca. 24.2º which is right in between the (012) peak of Ti_2O_3 (23.9º) and the anatase (101) peak (25.2º), indicating that some anatase remained in the sample but no longer the dominate phase. Furthermore, new diffraction patterns can be seen to emerge with the CubTiO samples at ca. 36.1º and 39.8º that clsoely match the (111) and (022) peaks of CuO (35.8º and 38.9º), and the peak intensity increased with increasing Cu doping from 1%CubTiO to 8%CuTiO. The fact that these peaks shifted appreciably from the standard Ti_2O_3 and CuO profiles indicate rich structural defects of the samples due to the rapid heating of MIH.[35]

The elemental composition and valence state of the samples were then examined by XPS measurements. From the survey spectra in **Figure 8**, the B 1s, Ti 2p, O 1s and Cu 2p electrons can be resolved at ca. 190, 462, 530 and 933 eV, respectively (the peak at ca. 285 eV likely arose from adventitious carbon).

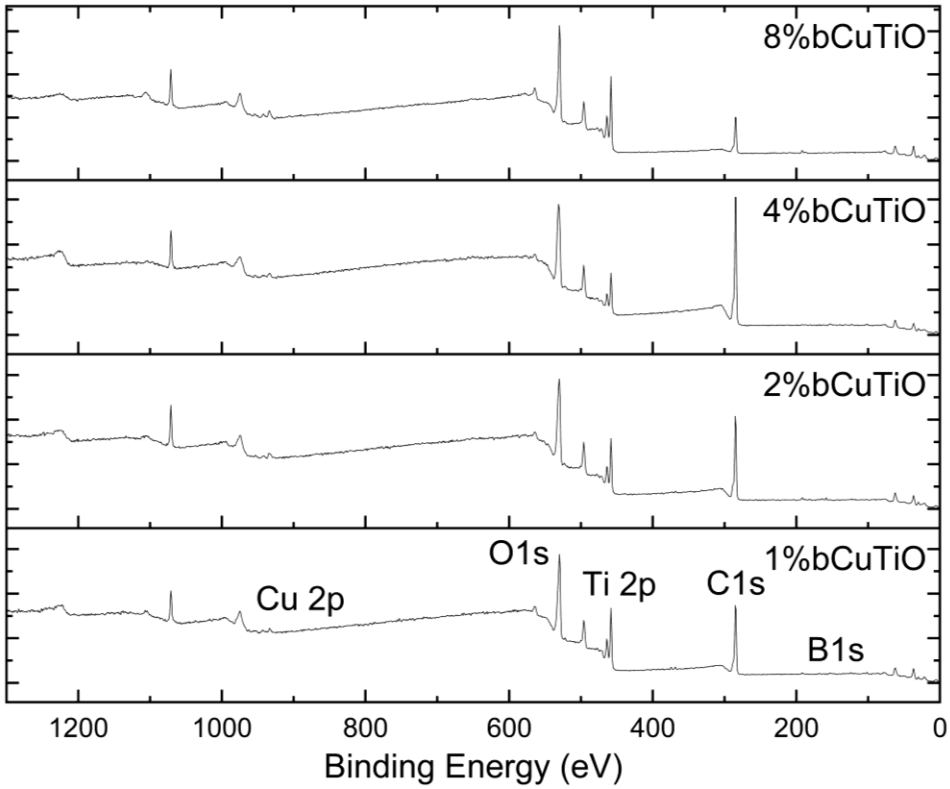

Figure 8. Survey Spectra of the sample series.

The high-resolution scans of the Ti 2p electrons are shown in **Figure 9a**. All samples can be seen to possess two doublets, one at 458.6/464.6 eV due to the Ti^{4+} $2p_{3/2}/2p_{1/2}$ electrons and the other at ca. 458.1/463.6 eV for Ti^{3+}, confirming the successful formation of TSOs in CubTiO (**Table 1**).[35-37]

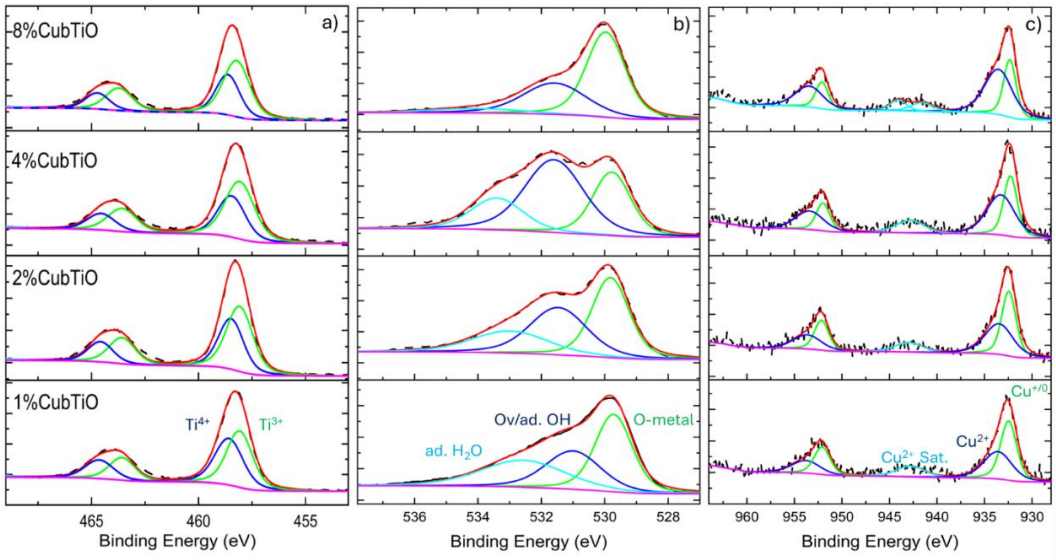

Figure 9. XPS spectra of the (a) Ti 2p, (b) O 1s and (c) Cu 2p electrons of the CubTiO sample series.

Table 1. Binding energies (eV) of the sample series from XPS measurements

Species		**1%CubTiO**	**2%CubTiO**	**4%CubTiO**	**8%CubTiO**
B 1s	Interstitial B	187.86	186.76	187.53	187.74
	B-O	191.93	191.83	191.67	191.89
C 1s	C-C	284.80	284.80	284.80	284.80
	C-N/C-O	285.90	286.11	286.05	285.99
	C=N/C=O	288.78	288.79	288.72	288.9
Ti 2p	Ti^{3+}	458.08	458.08	458.07	458.22
	Ti^{4+}	458.58	458.48	458.45	458.63
	Ti^{3+}	463.58	463.58	463.57	463.72
	Ti^{4+}	464.64	464.58	464.55	464.73
	Ti sat	471.09	471.1	471.03	471.16
O 1s	M-O	529.72	529.82	529.78	529.97
	OV/ adsorbed OH	531.00	531.47	531.60	531.58
	Adsorbed H2O	532.58	532.99	533.4	534.03
Cu 2p	Cu^{1+}	932.46	932.44	932.27	932.34
	Cu^{2+}	933.59	933.47	933.29	933.53
	Cu Sat	942.76	942.97	942.83	941.57
	Cu^{1+}	952.08	952.14	951.99	952.10
	Cu^{2+}	953.79	953.65	953.40	953.43

Furthermore, based on the integrated peak areas (**Table 2**), one can see that the Ti^{3+}/Ti^{4+} atomic ratio increased with increasing Cu doping from 1.10 for 1%CubTiO to 1.35 for 2%CubTiO, 1.47 for 4%CubTiO, and 1.55 for 8%CubTiO, suggesting that Cu doping facilitated the formation of Ti^{3+} likely due to the more labile reduction of Cu^{2+} to Cu^{0} that mediated the Ti^{4+} reduction to Ti^{3+}. Overall, this is in good alignment with results from the above TEM, Raman and XRD measurements.

Table 2. Elemental contents (at%) of the sample series from XPS measurements

Species		**1%CubTiO**	**2%CubTiO**	**4%CubTiO**	**8%CubTiO**
B 1s	Interstitial B	0.64	0.79	0.94	2.51
	B-O	2.33	3.87	1.4	4.99
C 1s	C-C	35.81	40.15	20.71	17.02
	C-N/C-O	10.71	6.95	27.8	10.18
	C=N/C=O	4.62	5.04	12.04	4.34
Ti 2p	Ti^{3+}	4.96	4.32	5.05	8.33
	Ti^{4+}	4.52	3.19	3.44	5.36
	Ti sat	0.73	0.62	0.36	1.14
O 1s	M-O	13.82	13.89	7.86	25.55
	OV/adsorbed OH	10.2	12.6	13.93	15.25
	Adsorbed H_2O	10.93	7.87	5.38	3.19
Cu 2p	Cu^{+}	0.36	0.34	0.43	0.75
	Cu^{2+}	0.29	0.32	0.59	1.28

	Cu^{2+} sat	0.08	0.07	0.06	0.13

The associated O 1s spectra are shown in **Figure 9b**, where the lattice O-Ti peak can be resolved at ca. 529.8 for all samples, along with oxygen vacancy (OV) at ca. 531.5 eV and surface-adsorbed oxygen species at ca. 533.2 eV.[38, 39] Notably, the OV to O-Ti ratio was found to increase from 0.74 for 1%CubTiO to 0.91 for 2%CubTiO, 1.77 for 4%CubTiO, and 0.60 for 8%CubTiO, again, suggestive of an increasingly defective oxide structure.[35]

The Cu 2p spectra are shown in **Figure 9c**, where deconvolution yields two doublets at 932.4/952.1 and 933.3/953.4 eV that can be ascribed to the $2p_{3/2}/2p_{1/2}$ electrons of $Cu^{+/0}$ and Cu^{2+} (the corresponding Cu^{2+} satellite can be found at ca. 942.8 eV), respectively.[40]

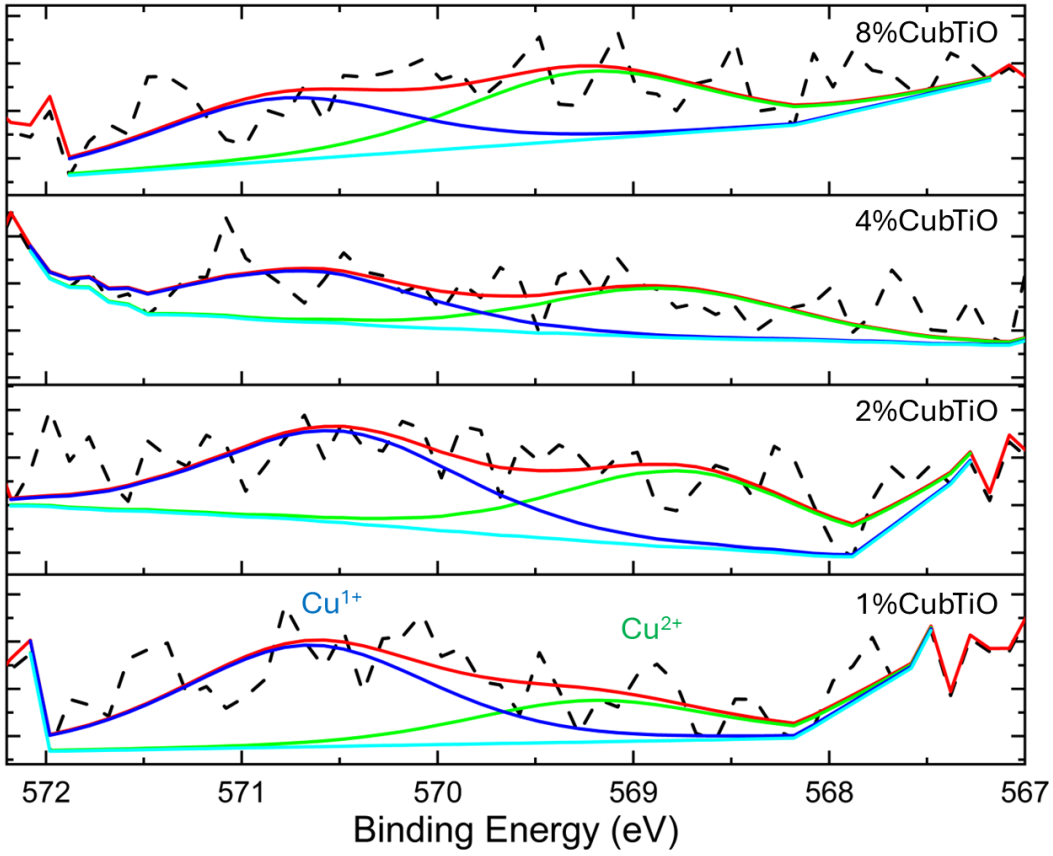

Figure 10. Cu LMM XPS spectra of the sample series.

Figure 10 shows the corresponding Cu LMM spectra, where only Cu^{+} and Cu^{2+} species can be resolved and Cu^{2+} was the dominant species, in good agreement with results from the above Raman and XRD measurements. In addition, the Cu content was estimated to be ca. 0.73 at% for 1%CubTiO and 2%CubTiO, 1.08 at% for 4%CubTiO, and 2.16 at% for 8%CubTiO, with a Cu:Ti atomic ratio of 0.07:1, , 0.09:1, 0.12:1 and 0.14:1, respectively, in qualitive agreement with the initial feed ratios. Overall, results from the XPS measurements confirm the effective reduction of the CuTiO samples to structurally defective CubTiO.

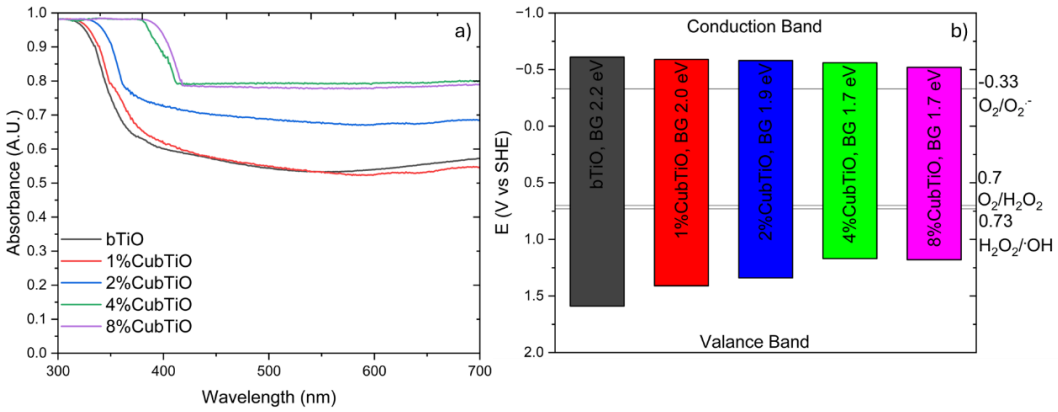

Figure 11. (a) UV-vis absorbance spectra of sample series after reduction treatment and (b) band structures with possible radicals produced by piezocatalysis of the sample series after reduction.

The electronic structures of the materials were then examined by UV-vis absorption and Mott-Schottky measurements. **Figure 11a** depicts the UV-vis diffuse reflectance spectra of the sample series, where the visible absorbance of the samples increases drastically with Cu loading in the order of bTiO < 1%CubTiO < 2%CubTiO < 4%CubTiO ≈ 8%CubTiO, suggesting diminishment of the materials bandgap. In Mott-Schottky analysis (**Figure 12**), all samples can be seen to exhibit a positive slope at various frequencies, indicating n-type semiconductor characteristics.[41]

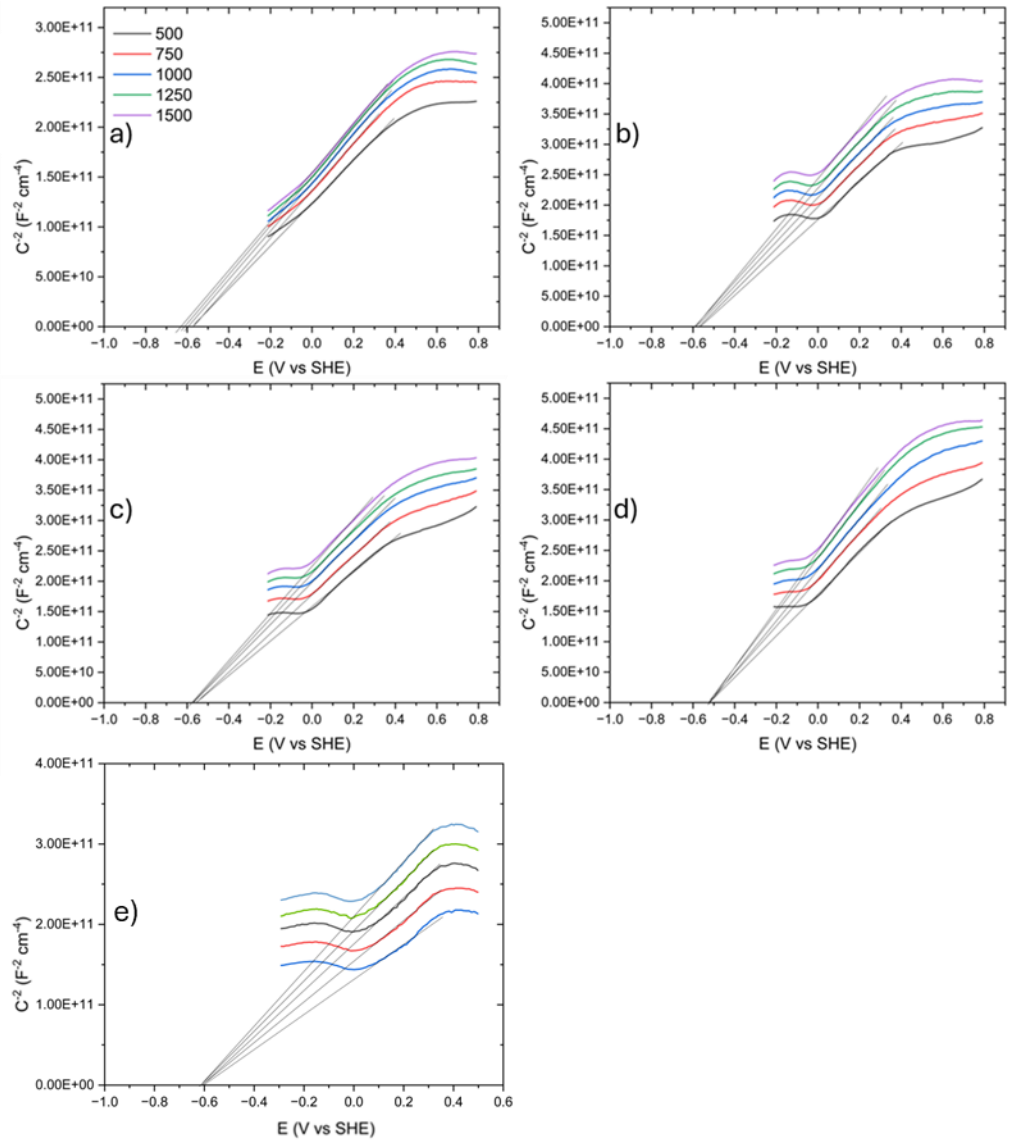

Figure 12. Mott Schottkey plots with accompanied linear regression of the sample series: (a) 1%CubTiO, (b) 2%CubTiO, (c) 4%CubTiO, (d) 8%CubTiO and (e) bTiO

From linear regressions of the profiles, the flat-band potential (E_{fb}) can be estimated to be -0.61 V (vs. SHE) for bTiO, -0.59 V for 1%CubTiO, -0.58 V for 2%CubTiO, -0.56 V for 4%CubTiO, and -0.52 V for 8%CubTiO. The positive shift of the flat band

potential with Cu dopant concentration likely arose from increasing consumption of the majority carriers (electrons) by copper ions in the sample, such that the Fermi level (E_f) dropped further from the conduction band (CB).[42] In conjunction with the bandgaps estimated from the UV-vis measurements, the CB/valance band (VB) can be determined to be at -0.61/+1.59 V for bTiO, -0.59/+1.41 V for 1%CubTiO, -0.58/+1.34 V for 2%CubTiO, -0.56/+1.17 V for 4%CubTiO, -0.52/+1.18 V for 8%CubTiO, as illustrated in **Figure 11b**. The CB is sufficiently negative for both the production of superoxide radicals (E° = -0.33 V) as well as hydrogen peroxide (E° = +0.70 V), along with its decomposition into hydroxyl radicals (E° = +0.73 V), but the VB is not positive enough to allow for direct water oxidation to hydroxyl radicals (E° = +2.74 V).[43-46]

5.3.2 Piezoelectric Activity

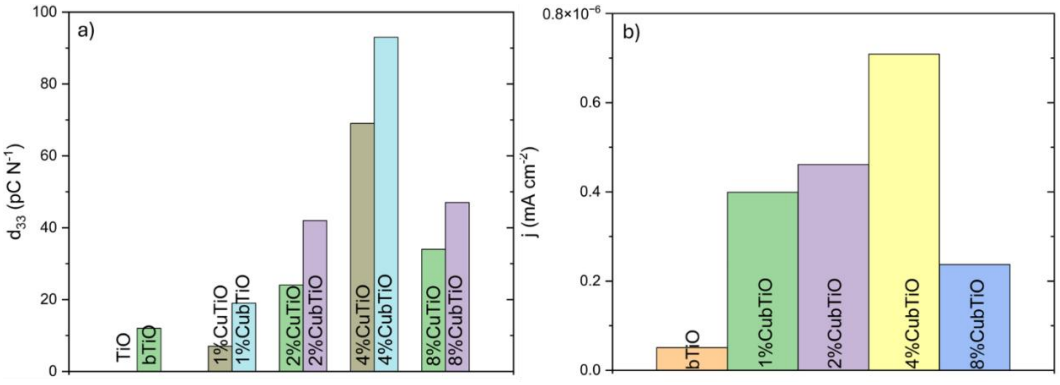

Figure 13. (a) d_{33} coefficients and (b) average induced change in transient piezocurrents of the sample series.

Remarkably, the CubTiO samples exhibited drastically enhanced piezoelectric properties**. Figure 13a** shows the d_{33} coefficients of the sample series. One can see that in contrast to the as-produced TiO sample (consisting primarily of anatase TiO_2) that was essentially piezoelectrically inactive ($d_{33} = 0$), bTiO and the Cu-doped samples all possessed a non-zero d_{33} coefficient, likely due to thermal reduction that produced structural defects and broke the crystal symmetry and the formation of heterojunctions that facilitated charge transfer under sonication. In fact, two trends can be clearly seen. Firstly, upon chemical reduction by MIH treatment in the presence of $NaBH_4$, the samples displayed a significantly greater d_{33} coefficient than the pre-reduction counterparts. Secondly, incorporation of CuO drastically enhanced the d_{33} coefficient of the samples reaching a maximum of 92 pC N^{-1} with 4%CubTiO and then decreasing with a further increase of Cu doping (e.g., 47 pC N^{-1} for 8%CubTiO). This suggests that 4%CubTiO possessed the optimal structure. Additionally, in comparison to bTiO mixed with other transition metal oxides (e.g., Mn, Fe, and Co) at the same feed ratio, 4%CubTiO also exhibited a markedly higher piezoelectric activity (**Figure 14**), where the d_{33} coefficient was significantly lower at 20 pC N^{-1} for 4%bMnTiO, 29 pC N^{-1} for 4%bFeTiO, and 32 pC N^{-1} for 4%bCoTiO.

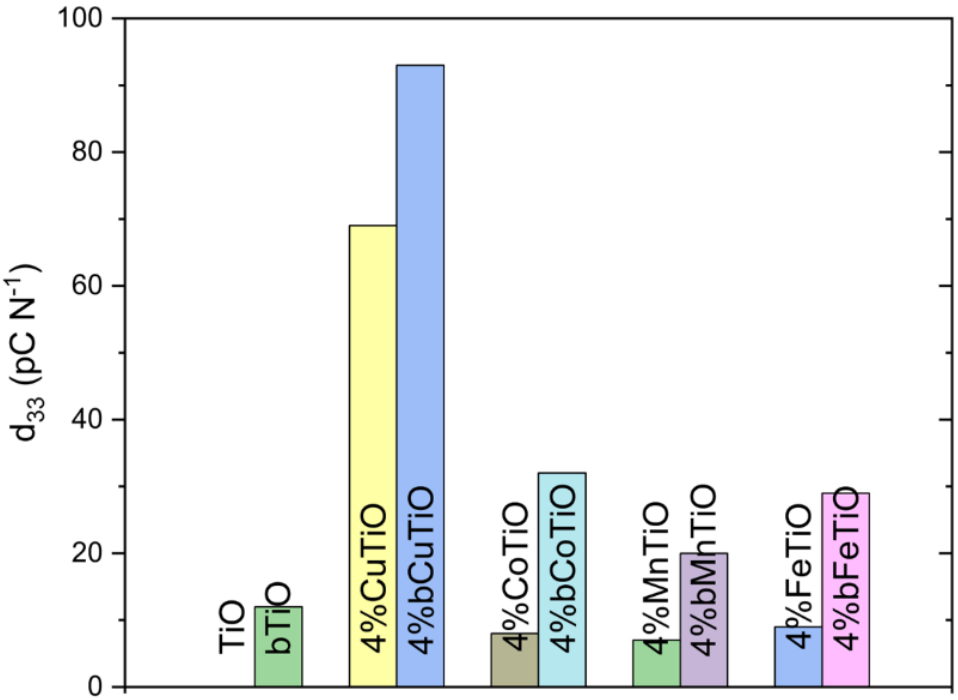

Figure 14. d_{33} coefficients of the TiO_2 and 4% doped samples before and after MIH reduction.

Consistent results were obtained in transient current measurements under ultrasonic activation. From **Figure 13b** and **Figure 15**, one can see that the average piezocurrent varied in the order of 4%CubTiO > 2%CubTiO > 8%CubTiO > 1%CubTiO > bTiO. That is, the 4%CubTiO sample stood out with the highest piezoelectric activity.

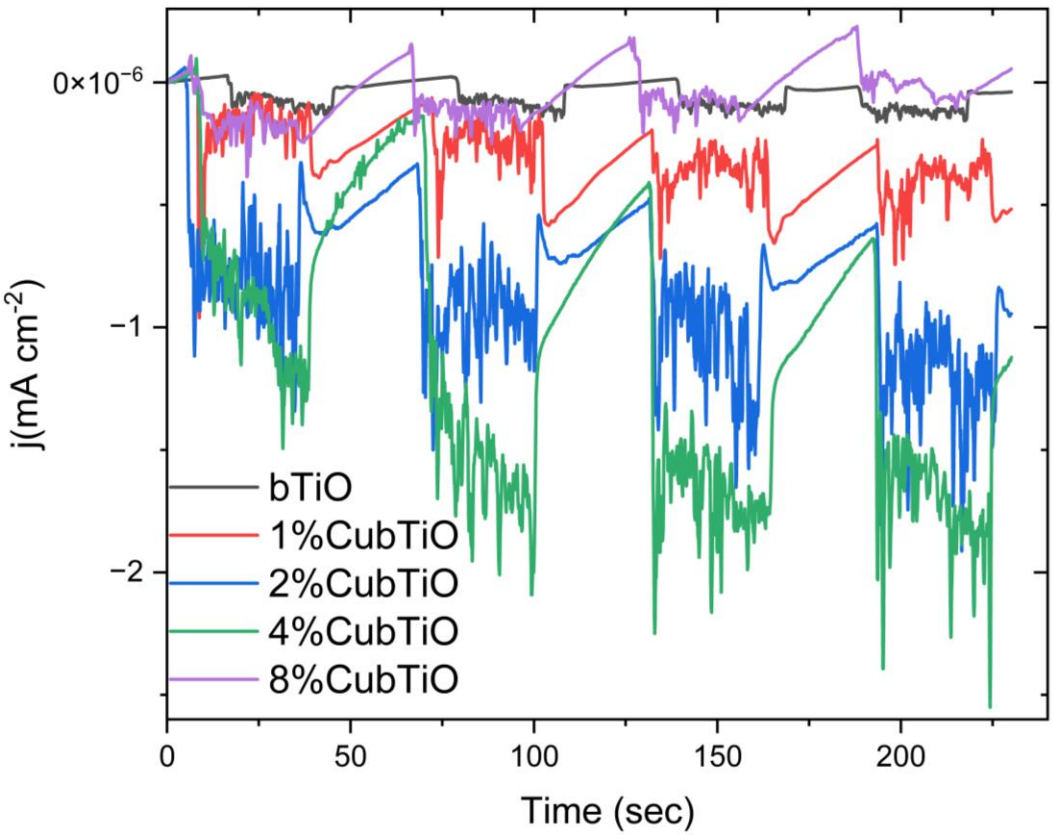

Figure 15. Transient piezocurrents of the sample series from Figure 13b.

This aligned well with the piezoelectric property observed above. TiO_2/CuO readily forms a n-p type heterojunction[47] which can readily transfer electrons and induce a strong internal magnetic field, while TiO_2/MnO_2 and TiO_2/Fe_2O_3 more readily form n-n type heterojunctions that impeded electron tranfers.[48, 49] Whereas TiO_2/CoO is a n-p type heterojunction[50] like TiO_2/CuO, the TiO_2/Co_2O_3 structure is known to be unstable leaving behind a highly defective amorphous structure which can impact charge transfer.[51]

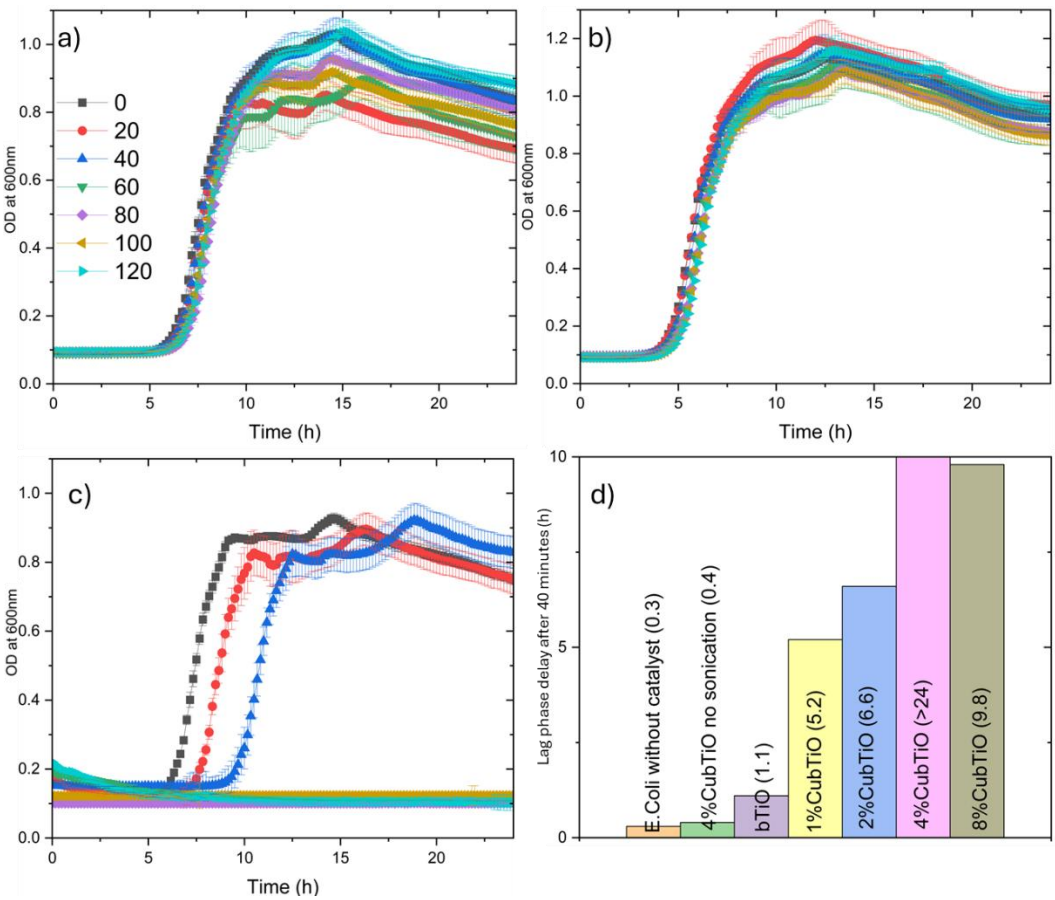

Figure 16. Growth curves of *E. coli* (a) under sonication for 2 h in the absence of catalysts, as well as in the presence of 4%CubTiO (b) without sonication as a control for 2 h and (c) under sonication for 2 h. (d) Bar chart of the lag phase delay after 40 min of sonication of the sample series.

The piezocatalytic activity of the samples towards eradication of water-borne pathogenic bacteria was then evaluated and compared. **Figure 16a** depicts the growth curves of *E. coli* under sonication for up to two hours without the addition of any catalyst sample. It can be seen that ultrasonic stimulation alone did not impact the bacterial cell growth. Similarly, no variation of the bacteria growth was observed with

the addition of 4%CubTiO on the bench top without physical stimulus (**Figure 16b**), indicating the material was not active without physical agitation. Yet, upon sonication, clear inhibition was observed in the presence of 4%CubTiO with the growth phase being delayed from 6.2 h of incubation without sonication to 9.8 h after 40 min of sonication, and an almost complete lack of growth after 60 min (**Figure 16c**). This performance was drastically better than those of the other samples in the series (**Figure 16d** and **17**), where the antibacterial activity varied in a very similar trend as their d_{33} coefficient and piezocurrent activity.

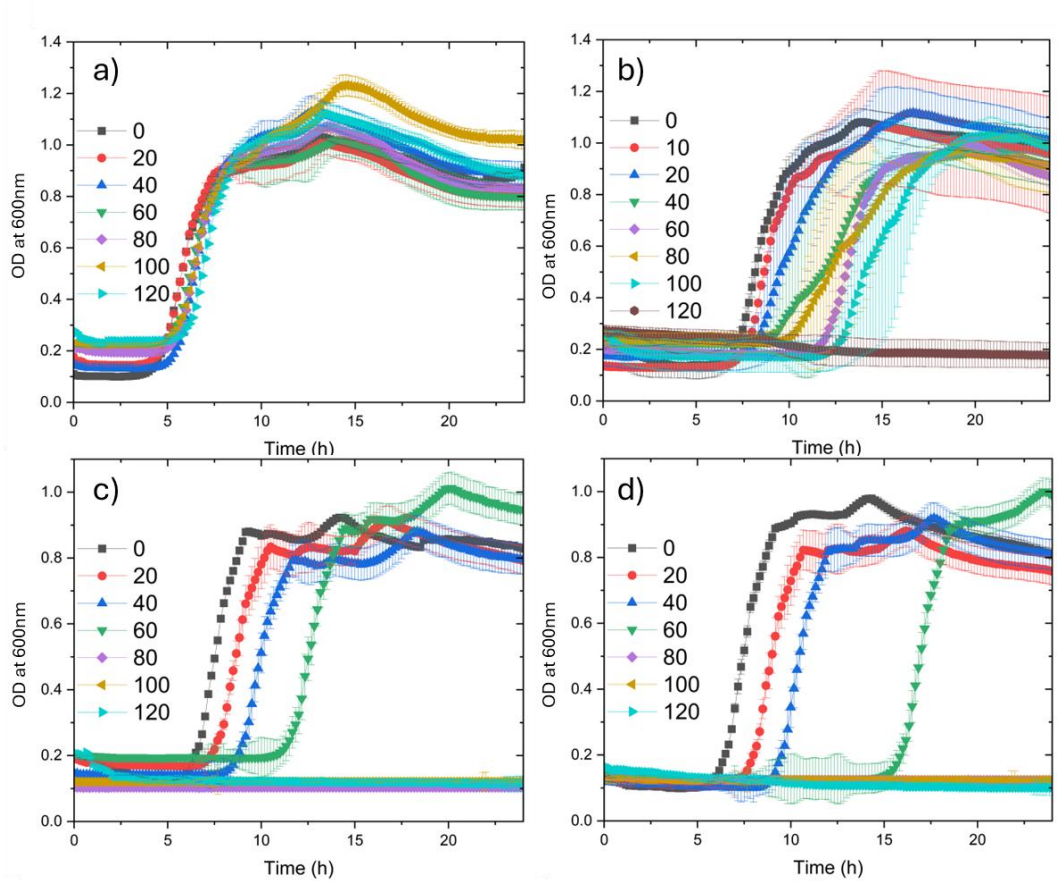

Figure 17. Growth Curves of *E. coli* in the presence of (a) bTiO, (b) 1%CubTiO, (c) 2%CubTiO, and (d) 8%CubTiO under sonication for up to 2 h.

Specifically, the 2%CubTiO (**Figure 17c**) and 8%CubTiO (**Figure 17d**) samples were both able to fully inhibit the growth of *E. coli* after prolonged sonication for 80 min, while 8%CubTiO had a more noticeable impact on the lag phase reaching a delay of 9.8 h after 60 min vs 6.6 h delay for 2%CubTiO. The 1%CubTiO was also able to fully inhibit the cell growth but required 120 min of sonication to achieve it (**Figure 17b**). In contrast, the bTiO sample exhibited only a minimal effect on the cell growth where

the lag phase increased marginally from 4.8 to 6.4 h and cell growth never reached full inhibition (**Figure 17a**).

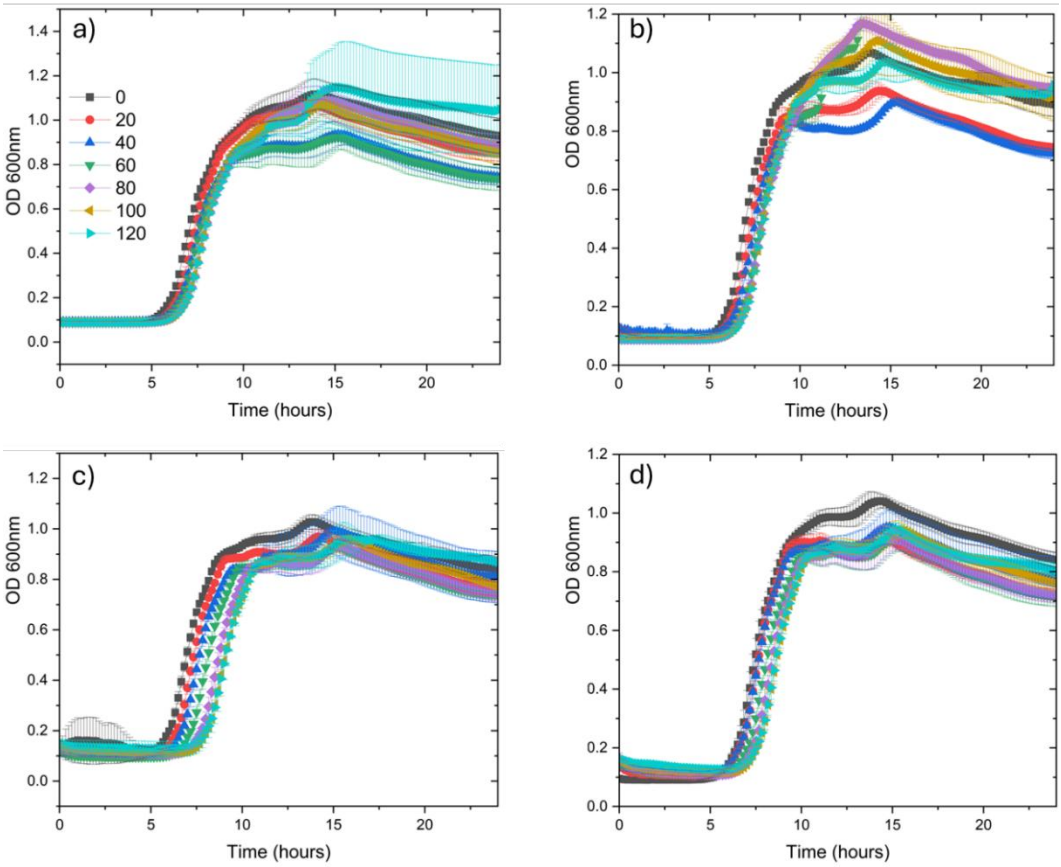

Figure 18. Growth curves of *E. coli*: (a) control, and in the presence of (b) 4%bFeTiO, (c) 4%bCoTio, and (d) 4%bMnTiO under sonication for up to 2 h.

In addition, for the Co, Mn and Fe doped samples (**Figure 18**), whereas all samples showed only a minimal impact on the lag phase, with the lag time increased by only 1.5 h for 4%bMnTiO, 1.6 h for 4%bFeTiO, and 2.4 h for 4%bCoTiO, and did not achieve complete cell growth inhibition even after 120 min of sonication. Such an activity mirrored the d_{33} depicted in **Figure 14**. This again supports the idea that Cu

is a superior dopant for this material. Taken together, these results highlight the significant impacts of Cu dopants on the piezoelectric catalytic activity as undoped titanium suboxides are known to be minimally piezoelectric.[52]

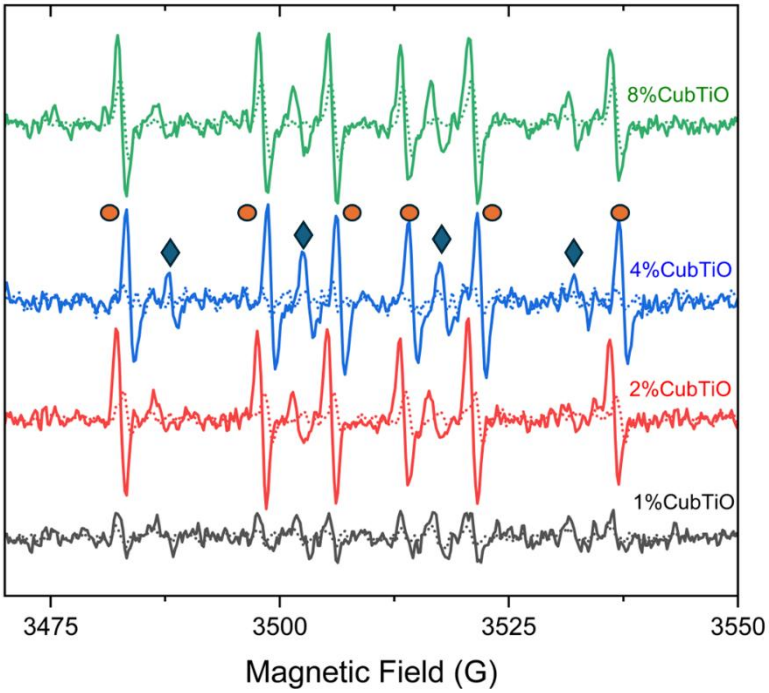

Figure 19. EPR spectra of the sample series with DMPO as the spin trap before (dotted curves) and after (solid curves) sonication for 10 min.

EPR measurements were then carried out to unravel the mechanistic origin of the piezocatalytic activity. From the EPR specrta in **Figure 19,** one can see that all samples display a similar pattern consisting of two sets of hyperfine features. The primary one is a sextet at a peak intensity ratio of 1:1:1:1:1:1 and a g value of 2.0058, characterist of superoxide anions ($O_2^{\cdot -}$),[53, 54] whereas the secondary one is a quartet at a peak intensity ratio of 1:2:2:1 and a g value of 2.005, suggesting the formation of hyrodxyl

radicals (•OH).[53] This aligns very closely with the predicted band structure in **Figure 11b**, where production of superoxide and hydroxyl radicals were energetically favorable by reduction of oxygen of CB electrons. Additionally, one can see that the variation of the sextet intensity was in good alignment with the materials' piezoelectric properties (**Figure 13a**), with 4%CubTiO featuring the most intense signals, whereas the hydroxyl quartet remained virtually invariant among the samples. This suggests that superoxide anions were the primary ROS produced piezocatalytically, which then followed a Fenton-like pathway to produce hydroxyl radicals catalytzed by the Cu^{2+}/Cu^{+} couples.[55]

5.4. Experimental Section

5.4.1 Chemicals

Titanium butoxide (Acros Organics), cupric nitrate ($Cu(NO_3)_2$, Fisher Scientific), sodium borohydride ($NaBH_4$, 99%, Sigma-Aldrich), 5,5'-dimethyl-1-pyrroline-N-oxide (DMPO, Fisher Scientific), isopropyl alcohol (Fisher Scientific), methanol (Fisher Scientific), ethanol (Sigma-Aldrich), acetone (Fisher Scientific), and methylene blue hydrate (MB, Acros Organics) was all used as received. Water was purified with a Barnstead Nanopure Water System (resistivity 18.3 MΩ cm).

5.4.2 Sample Synthesis

In a typical experiment, 10 mL of titanium butoxide was dispersed into a mixture of 100 mL isopropanol and 10 mL of methanol under magnetic stirring for 60 min at 60

ºC. Separately, a calculated amount of $Cu(NO_3)_2$ (at the Cu:Ti molar ratio of X = 1% to 8%) was dissolved in a mixture of 20 mL of water and 10 mL of ethanol under sonication for 5 min. The $Cu(NO_3)_2$ solution was then added dropwise into the titanium butoxide solution under sonication at 70 ºC, and the produced gel was transferred to a Teflon liner and autoclaved at 180 ºC for 12 h. The resulting samples were then washed with isopropanol, methanol, water, and ethanol until the solvent was clear. After being dried overnight, the samples were placed in a ceramic boat and heated at 450 ºC for 4 h in a muffle furnace under ambient condition before being washed again with water, ethanol, isopropanol and methanol until the solvents were clear, and referred to as X%CuTiO. A control sample was prepared in the same fashion but without the addition of $Cu(NO_3)_2$ and denoted as TiO.

200 mg of the samples prepared above were mixed with 75 mg of $NaBH_4$ in mortar and pestle until the mixture was a uniform fine white powder. 50 mg of the mixture was placed on an iron sheet lined with graphitic paper, which was placed on a fire brick in a quartz tube. The assembly was purged with ultrahigh-purity argon for 10 min before MIH treatment at the induction current of 600 A for 12 s.[20, 22] After heating, the samples were washed with water, ethanol, and acetone, until a clear supernatant was produced with no bubbles, and denoted as X%CubTiO and bTiO.

A series of control samples were also prepared in the same manner as that for 4%CubTiO but by replacing $Cu(NO_3)_2$ with an equivalent amount of $Co(NO_3)_2$, $Fe(NO_3)_3$, and $Mn(NO_3)_2$, and denoted as 4%CoTiO, 4%FeTiO and 4%MnTiO, respectively.

5.4.3 Characterization

Transmission electron microscopy (TEM) images were acquired with a Tecni G2 operated at 200 kV. Raman measurements were conducted using a Horiba Jobin Yvon Lab-RAM ARAMIS automated scanning confocal Raman microscope under 532 nm excitation. UV-vis absorption measurements were conducted with a Perkin-Elmer Lambda 35 spectrometer. X-ray diffraction (XRD) patterns were acquired with a Rigaku Smartlab diffractometer (Cu K_a radiation, l = 0.154 nm). X-ray photoelectron spectroscopy (XPS) measurements were carried out with a Thermo Fisher K-alpha system, where the binding energy was calibrated against the C 1s peak. Electron paramagnetic resonance (EPR) was recorded at room temperature with a Bruker ElexSys E500 spectrometer operating at the X-band frequency (~9.8 GHz) using an ER 4122SHQE resonator. Spectra were recorded using a microwave power of 20.03 mW, modulation amplitude of 1 G, modulation frequency of 100 kHz, and conversion time of 20.48 ms. Contact angles were measured with a Tantec CAM-PLUS contact angle meter.

5.4.4 Electrochemistry

Mott-Schottky and transient photocurrent measurements were carried out with a Gamry Reference 600 instrument in a three-electrode setup. The working electrode was a rotating disk electrode with a surface area of 0.196 cm^2, a graphite rod was used as the counter electrode, Ag/AgCl as the reference electrode, and 0.5 M Na_2SO_4 as the supporting electrolyte. Mott-Schottky analysis was performed within a frequency range

of 500 to 1500 Hz. Transient piezocurrent measurements were performed at a constant potential of -0.25 V vs Ag/AgCl under controlled sonication.

5.4.5 Piezocatalytic disinfection of water

E. coli cells were grown in Luria−Bertani (LB) agar in a 37 °C incubator. A single colony was selected and used to inoculate 3 mL of LB broth and allowed to shake at 37 °C for 18 h. The resulting liquid was centrifuged at 5000 rpm for 5 min and resuspended in phosphate buffered saline (PBS) 3 times before being diluted to an optical density (OD) of 0.1 at 600 nm. Then 1 mL of the spiked PBS solution was diluted into 99 mL of sterile PBS, and 100 mL of this solution was added to 9.9 mL of PBS with 100 mg of the samples prepared above for a final concentration of 10 mg mL^{-1}. The vials containing the bacteria were then sonicated for 2 h with 10 μL aliquots removed every 20 min and pipetted into a 96-well plate along with 200 μL of sterile LB broth. The 96-well plate was placed in a Molecular Device VERSA max microplate reader, where the OD was measured at 600 nm every 10 min with intermittent shaking between each reading over a 24 h incubation period at 37 °C.

5.4.6 EPR Measurements

To assess the ROS generation, 1 mg mL^{-1} solutions of the samples were prepared in water. Then 63 mL of the solution was mixed with 7 mL of 1 M DMPO in water for a total of 70 mL, which were then either left unmoved on the counter as controls or subject to sonication for 10 min. 10 mL of the solutions was loaded into a 1.5 mm O.D. borosilicate capillary tube (Friedrich & Dimmock Borosilicate Capillary). Spectra were

recorded at room temperature with a Bruker ElexSys E500 spectrometer operating at the X-band frequency (~9.8 GHz) using an ER 4122SHQE resonator using a microwave power of 20.03 mW, modulation amplitude of 1 G, modulation frequency of 100 kHz, and conversion time of 20.48 ms.

5.5 Conclusions

In this study, copper-doped titanium oxide nanoparticles were produced by a facile thermal procedure, and subject to chemical reduction via magnetic induction heating in the presence of $NaBH_4$ to copper oxide/titanium suboxide heterostructures. The resultant CubTiO exhibited markedly enhanced piezoelectric properties, as compared to the pre-reduction counterparts, with the 4%CubTiO sample showing the greatest d_{33} coefficient at 92 pC N^{-1}, and the highest antibacterial activity where the growth of *E. coli* was fully inhibited after sonication for under 1 h, due to the effective production of superoxide anions and hydroxyl radials. Results from this work provide insights into the significance of structural engineering in enhancing the piezoelectric activity and antibacterial performance of metal oxides.

5.6 References

(1) An, T.; Yin, H.; Cai, Y.; Chen, M.; Sun, T.; Wang, W.; Li, G. Photocatalysis Inhibits the Emergence of Multidrug-Resistant Bacteria in an Antibiotic-Resistant Bacterial Community in Aquatic Environments. *Environ Sci Technol* **2024**, *58* (40), 17937-17947. DOI: 10.1021/acs.est.4c06752.

(2) Rojas-Andrade, M. D.; Chata, G.; Rouholiman, D.; Liu, J. L.; Saltikov, C.; Chen, S. W. Antibacterial mechanisms of graphene-based composite nanomaterials. *Nanoscale* **2017**, *9* (3), 994-1006.

(3) Meng, F.; Guo, C.; Cui, T.; Wang, Y.; Julian, R. A.; Chen, X.; Yu, B.; Pan, D.; DuBois, D. B.; Tressel, J. Rapid synthesis of single-layer iron-doped 2H tungsten sulfide via magnetic induction heating for piezocatalytic reduction of oxygen to hydrogen peroxide. *Applied Catalysis B: Environment and Energy* **2025**, *371*, 125224.

(4) Meng, F. Q.; Guo, C. X.; Cui, T. C.; Xu, M. Y.; Chen, X. X.; Xu, H. W.; Liu, C.; Chen, S. W. Piezoelectric catalysis for antibacterial applications. *Mater Chem Front* **2025**, *9* (2), 171-188. DOI: 10.1039/d4qm00848k.

(5) Zhu, P.; Chen, Y.; Shi, J. Piezocatalytic Tumor Therapy by Ultrasound-Triggered and BaTiO3-Mediated Piezoelectricity. *Advanced Materials* **2020**, *32* (29), 2001976. DOI: https://doi.org/10.1002/adma.202001976.

(6) Mahapatra, S. D.; Mohapatra, P. C.; Aria, A. I.; Christie, G.; Mishra, Y. K.; Hofmann, S.; Thakur, V. K. Piezoelectric Materials for Energy Harvesting and Sensing Applications: Roadmap for Future Smart Materials. *Advanced Science* **2021**, *8* (17), 2100864. DOI: https://doi.org/10.1002/advs.202100864.

(7) Xia, T.; Lu, L.; Zhang, H.; Wang, J.; Huang, Z.; Wang, H.; Yang, W.; Gao, S.; Li, Q. Inducing piezoelectricity in distorted rutile TiO 2 for enhanced tetracycline hydrochloride degradation through photopiezocatalysis. *Journal of Advanced Ceramics* **2024**, *13* (3), 323-331.

(8) Feizpoor, S.; Pouran, S. R.; Habibi-Yangjeh, A. Recent progress on photocatalytic evolution of hydrogen gas over TiO2-x-based emerging nanostructures. *Materials Science in Semiconductor Processing* **2023**, *162*, 107444.

(9) Khorashadizade, E.; Rahimi, K.; Mohajernia, S.; Hejazi, S.; Naseri, N.; Moradlou, O.; Moshfegh, A.; Schmuki, P. Comparing plasma reduction and thermal hydrogenation in oxygen deficient TiO2-x nanotubes for photoelectrochemical H2 production. *International Journal of Hydrogen Energy* **2024**, *74*, 434-446.

(10) Ekanayake, S. A.; Seeber, A.; Olorunyomi, J. F.; Mai, H.; Mahasivam, S.; Shah, D.; Lu, J.; Wen, X.; Sampath, N.; Schumann, S. L. Activated charcoal-mediated non-contact carbothermal reduction of TiO 2 for controlled synthesis of Magnéli phase titanium suboxides. *Journal of Materials Chemistry A* **2024**, *12* (24), 14734-14743.

(11) Wang, K.; Han, C.; Li, J.; Qiu, J.; Sunarso, J.; Liu, S. The mechanism of piezocatalysis: energy band theory or screening charge effect? *Angewandte Chemie International Edition* **2022**, *61* (6), e202110429.

(12) Kumar, A.; Barbhuiya, N. H.; Singh, S. P. Magneli phase titanium sub-oxides synthesis, fabrication and its application for environmental remediation: Current status and prospect. *Chemosphere* **2022**, *307*, 135878. DOI: ARTN 135878

10.1016/j.chemosphere.2022.135878.

(13) Han, X.; Huang, J.; Jing, X.; Yang, D.; Lin, H.; Wang, Z.; Li, P.; Chen, Y. Oxygen-deficient black titania for synergistic/enhanced sonodynamic and photoinduced cancer therapy at near infrared-II biowindow. *Acs Nano* **2018**, *12* (5), 4545-4555.

(14) Zhang, S.; Zhang, L.; Hu, J.; He, X.; Geng, B.; Pan, D.; Shen, L. Trienzyme-like Co3O4@ TiO2-x nanozymes for heterojunction-enhanced nanocatalytic-sonodynamic tumor therapy. *Chemical Engineering Journal* **2023**, *458*, 141485.

(15) Wang, C.; Wu, S.; Mao, C.; Jin, L.; Liu, H.; Zheng, Y.; Liang, C.; Zhu, S.; Li, Z.; Jiang, H. Accelerating Sono-Piezoelectric Charge Transport for Antibacterial Therapy and Bone Regeneration by Metal-Deficient TiO2 Spin-Polarization Effect. *Advanced Science* **2025**, *12* (30), e03186.

(16) Tressel, J.; Nguyen, A.; Nguyen, P.; Jones, C.; Cui, T.; Warshana, A.; Singewald, K.; Millhauser, G.; Saltikov, C.; Chen, S. Ultrafast Synthesis of Titanium Suboxide via Magnetic Induction Heating for Enhanced Photodynamic Activity. *Chemistry–A European Journal* **2026**, e03354.

(17) Liu, Q.; Lu, B.; Nichols, F.; Ko, J.; Mercado, R.; Bridges, F.; Chen, S. Rapid preparation of carbon-supported ruthenium nanoparticles by magnetic induction heating for efficient hydrogen evolution reaction in both acidic and alkaline media. *SusMat* **2022**, *2* (3), 335-346.

(18) Liu, Q.; Nichols, F.; Bhuller, A.; Singewald, K.; Kuo, H.-L.; Lu, J. Q.; Millhauser, G. L.; Bridges, F.; Ge, Q.; Chen, S. Ultrafast synthesis of amorphous molybdenum sulfide by magnetic induction heating for hydrogen evolution reaction. *Applied Catalysis B: Environmental* **2023**, 123399.

(19) Liu, Q.; McNair, S.; Nichols, F.; Lu, B.; Yu, B.; Pan, D.; Ko, J.; Bhuller, A.; Bridges, F.; Chen, S. Ultrafast synthesis of cobalt/carbon nanocomposites by magnetic

induction heating for oxygen evolution reaction. *Advanced Sensor and Energy Materials* **2023**, *2* (1), 100046.

(20) Pan, D. J.; Liu, Q. M.; Yu, B. Z.; DuBois, D. B.; Tressel, J.; Yu, S.; Kaleekal, N.; Trabanino, S.; Jeon, Y.; Bridges, F.; et al. Rapid Synthesis of Ruthenium-Copper Nanocomposites as High-Performance Bifunctional Electrocatalysts for Electrochemical Water Splitting. *Small* **2024**, 2404729. DOI: 10.1002/smll.202404729.

(21) Tressel, J.; Liu, Q.; DuBois, D.; Yu, B.; Warshana, A.; Bridges, F.; Saltikov, C.; Chen, S. Ultrafast Modification of Copper Chlorophyllin by Magnetic Induction Heating for Water Electrodisinfection by Selective Reduction of Oxygen to Hydrogen Peroxide. *The Journal of Physical Chemistry C* **2025**.

(22) Yu, B. Z.; Liu, Q. M.; Pan, D. J.; Singewald, K.; Dubois, D.; Tressel, J.; Hou, B. Y.; Millhauser, G. L.; Bridges, F.; Chen, S. W. Ultrafast preparation of ruthenium nanoparticle/molybdenum oxide/nitrogen-doped carbon nanocomposites by magnetic induction heating for efficient hydrogen evolution reaction. *J Mater Chem A* **2024**, *12* (26), 16087-16097. DOI: 10.1039/d4ta00884g.

(23) Dai, Y.; Zhao, J.; Liu, X.; Yu, X.; Jiang, Z.; Bu, Y.; Xu, Z.; Wang, Z.; Zhu, X.; Xing, B. Transformation and species identification of CuO nanoparticles in plant cells (Nicotiana tabacum). *Environmental Science: Nano* **2019**, *6* (9), 2724-2735.

(24) Wang, G. R.; Liu, Y.; Ye, J. W.; Yang, X. J.; Lin, Z. F. Formation mechanism of Ti4O7 phase prepared by carbothermal reduction reaction. *Journal of the American Ceramic Society* **2020**, *103* (6), 3871-3879. DOI: 10.1111/jace.17045.

(25) Badr, H. O.; Lagunas, F.; Autrey, D. E.; Cope, J.; Kono, T.; Torita, T.; Klie, R. F.; Hu, Y.-J.; Barsoum, M. W. On the structure of one-dimensional TiO2 lepidocrocite. *Matter* **2023**, *6* (1), 128-141.

(26) Huang, H. L.; Wang, C.; Li, Q.; Wang, R. Q.; Yang, Y. Y.; Muhetaer, A.; Huang, F. Q.; Han, B.; Xu, D. S. Efficient and Full-Spectrum Photothermal Dehydrogenation of Ammonia Borane for Low-Temperature Release of Hydrogen. *Advanced Functional Materials* **2021**, *31* (8), 2007591. DOI: ARTN 2007591

10.1002/adfm.202007591.

(27) Aswathappa, S.; Dai, L.; Sathiyadhas, S. J. D.; Kumar, R. S.; Almansour, A. I.; Freire, P. T. C.; Athiruban, S.; Kang, G. Quantitative analysis of anatase-rutile mixtures of TiO2 employing X-ray diffractometry and visible-Raman spectroscopy at normal heating and superheating conditions-Implications and limitations of the Spurr-Mayers equation. *Ceramics International* **2025**.

(28) Aswathappa, S.; Dai, L.; Dhas, S. S. J.; Kumar, R. S.; Palaniyasan, E. Size-dependent anatase to rutile phase transition under acoustic shocked conditions–A case study of TiO2 bulk and nanoparticles. *Applied Surface Science* **2025**, *681*, 161501.

(29) Jung, S.; Senthil, R. A.; Min, A.; Kumar, A.; Moon, C. J.; Choi, M. Y. Laser-synthesized Co-doped CuO electrocatalyst: unveiling boosted methanol oxidation kinetics for enhanced hydrogen production efficiency by in situ/operando Raman and theoretical analyses. *Small Methods* **2024**, *8* (8), 2301628.

(30) Yao, S.; Xue, S.; Zhang, Y.; Shen, X.; Qian, X.; Li, T.; Xiao, K.; Qin, S.; Xiang, J. Synthesis, characterization, and electrochemical performance of spherical

nanostructure of Magnéli phase Ti4O7. *Journal of Materials Science: Materials in Electronics* **2017**, *28* (10), 7264-7270.

(31) Lin, H.; Xiao, R.; Xie, R.; Yang, L.; Tang, C.; Wang, R.; Chen, J.; Lv, S.; Huang, Q. Defect engineering on a Ti4O7 electrode by Ce3+ doping for the efficient electrooxidation of perfluorooctanesulfonate. *Environmental Science & Technology* **2021**, *55* (4), 2597-2607.

(32) Yuan, T.; Wei, W.; Wang, Y.; Jin, N.; Ye, J. Effect of V-doping on structure and electrical conductivity of Magnéli phase Ti4O7. *Journal of Alloys and Compounds* **2024**, *978*, 173492.

(33) Wang, J.; Li, Y.; Deng, L.; Wei, N.; Weng, Y.; Dong, S.; Qi, D.; Qiu, J.; Chen, X.; Wu, T. High-performance photothermal conversion of narrow-bandgap Ti2O3 nanoparticles. *Advanced Materials* **2017**, *29* (3), 1603730.

(34) Li, Y.; Weng, Y.; Yin, X.; Yu, X.; Kumar, S. R. S.; Wehbe, N.; Wu, H.; Alshareef, H. N.; Pennycook, S. J.; Breese, M. B. H. Orthorhombic Ti2O3: a polymorph-dependent narrow-bandgap ferromagnetic oxide. *Advanced Functional Materials* **2018**, *28* (7), 1705657.

(35) Tressel, J.; Nguyen, A.; Nguyen, P.; Jones, C.; Cui, T. C.; Warshana, A.; Singewald, K.; Millhauser, G.; Saltikov, C.; Chen, S. W. Ultrafast Synthesis of Titanium Suboxide via Magnetic Induction Heating for Enhanced Photodynamic Activity. *Chemistry-a European Journal* **2026**, *32*, e03354. DOI: PMID 9513783

10.1002/chem.202503354.

(36) Varnagiris, S.; Medvids, A.; Lelis, M.; Milcius, D.; Antuzevics, A. Black carbon-doped TiO2 films: Synthesis, characterization and photocatalysis. *Journal of Photochemistry and Photobiology A: Chemistry* **2019**, *382*, 111941.

(37) Katal, R.; Salehi, M.; Davood Abadi Farahani, M. H.; Masudy-Panah, S.; Ong, S. L.; Hu, J. Preparation of a new type of black TiO2 under a vacuum atmosphere for sunlight photocatalysis. *ACS applied materials & interfaces* **2018**, *10* (41), 35316-35326.

(38) Guo, X.; Li, C.; Zhou, Y.; Chen, Y.; Deng, W.; Li, R. Ti2O3 (H2PO4) 2· 2H2O as a Novel Intercalated Anode for Ultralong Lifespan "Rocking-Chair" Aqueous Zinc-Ion Batteries. *Angewandte Chemie International Edition* **2025**, *64* (22), e202502446.

(39) Salcedo-Abraira, P.; Babaryk, A. A.; Montero-Lanzuela, E.; Contreras-Almengor, O. R.; Cabrero-Antonino, M.; Grape, E. S.; Willhammar, T.; Navalón, S.; Elkäim, E.; García, H. A novel porous Ti-squarate as efficient photocatalyst in the overall water splitting reaction under simulated Sunlight irradiation. *Advanced Materials* **2021**, *33* (52), 2106627.

(40) Yu, B. Z.; Diniz, J.; Lofgren, K.; Liu, Q. M.; Mercado, R.; Nichols, F.; Oliver, S. R. J.; Chen, S. W. Copper/Carbon Nanocomposites for Electrocatalytic Reduction of Oxygen to Hydrogen Peroxide. *Acs Sustain Chem Eng* **2022**, *10* (47), 15501-15507. DOI: 10.1021/acssuschemeng.2c04746.

(41) Wu, R. J.; Gao, S.; Jones, C.; Sun, M. M.; Guo, M.; Tai, R.; Chen, S. W.; Wang, Q. Bi/BSO Heterojunctions via Vacancy Engineering for Efficient Photocatalytic

Nitrogen Fixation. *Advanced Functional Materials* **2024**, *34* (24), 2314051. DOI: ARTN 2314051

10.1002/adfm.202314051.

(42) Koshevoy, E.; Gribov, E.; Lyulyukin, M.; Selishchev, D.; Kozlov, D. Photoelectrochemical study of M/TiO2 (M = Pt, Pd, Au) supported catalysts: flat-band potentials and photoelectrocatalytic properties in glycerol oxidation reaction. *Journal of Photochemistry and Photobiology a-Chemistry* **2026**, *471*, 116678. DOI: ARTN 116678

10.1016/j.jphotochem.2025.116678.

(43) Koppenol, W. H.; Butler, J. Energetics of interconversion reactions of oxyradicals. *Advances in Free Radical Biology & Medicine* **1985**, *1* (1), 91-131.

(44) Nosaka, Y.; Nosaka, A. Understanding hydroxyl radical (• OH) generation processes in photocatalysis. *ACS Energy Letters* **2016**, *1* (2), 356-359.

(45) Cheng, K.; Li, H.; Laszakovits, J. R.; Sharpless, C. M.; Rosario-Ortiz, F.; McKay, G. Probing the photochemical formation of hydroxyl radical from dissolved organic matter: insights into the H2O2-dependent pathway. *Environmental Science & Technology* **2025**, *59* (4), 2245-2256.

(46) Chata, G.; Nichols, F.; Mercado, R.; Assafa, T.; Millhauser, G. L.; Saltikov, C.; Chen, S. W. Photodynamic Activity of Graphene Oxide/Polyaniline/Manganese Oxide Ternary Composites toward Both Gram-Positive and Gram-Negative Bacteria. *Acs Appl Bio Mater* **2021**, *4* (9), 7025-7033. DOI: 10.1021/acsabm.1c00677.

(47) Hao, B.; Guo, J.; Zhang, L.; Ma, H. Magnetron sputtered TiO2/CuO heterojunction thin films for efficient photocatalysis of Rhodamine B. *Journal of Alloys and Compounds* **2022**, *903*, 163851.

(48) Tripathi, S.; Pandey, N. K.; Verma, V. Efficient CO2 monitoring of cabin air in airplanes utilizing α-MnO2-TiO2 hetero-nanocomposite sensor. *Materials Science and Engineering: B* **2025**, *322*, 118671.

(49) Deng, C.; Li, S.; Wang, J.; Yang, Q.; Chen, H.; Tang, F.; Yang, X. Fabrication of α-Fe2O3/TiO2 heterojunction for photocatalytic degradation of doxycycline hydrochloride. *Journal of Molecular Liquids* **2025**, *417*, 126618.

(50) Ullah, F.; Ghani, U.; Saheed, M. S. M. A PN-type CuO@ TiO2 nanorods heterojunction for efficient PEC water splitting: DFT model and experimental investigation on the effect of calcination temperature. *International Journal of Hydrogen Energy* **2023**, *48* (100), 39866-39884.

(51) Uvarov, V.; Krutel, J.; Mašek, K.; Mysliveček, J.; Johánek, V. Thermal stability of cobalt oxide thin films and its enhancement by cerium oxide. *Applied Surface Science* **2022**, *593*, 153430.

(52) Han, Y. J.; Zhang, H. R.; Yang, R. H.; Yu, X. Y.; Marfavi, Z.; Lv, Q. J.; Zhang, G. X.; Sun, K.; Yuan, C. L.; Tao, K. Ba2+-doping introduced piezoelectricity and efficient Ultrasound-Triggered bactericidal activity of brookite TiO2 nanorods. *Journal of Colloid and Interface Science* **2024**, *670*, 742-750. DOI: 10.1016/j.jcis.2024.05.148.

(53) Dubois, D. B.; Tressel, J.; Hergenroeder, D.; Jones, C.; Yu, B. Z.; Singewald, K.; Millhauser, G. L.; Saltikov, C.; Chen, S. W. Antibacterial activity of bismuth tungstate

against Escherichia coli: Enhanced piezocatalysis by morphological engineering. *J Environ Chem Eng* **2025**, *13* (5), 118871. DOI: ARTN 118871

10.1016/j.jece.2025.118871.

(54) Ding, Y.; Zhao, Y.; Yao, S.; Wang, S.; Wan, X.; Hu, Q.; Li, L. Enhanced Sonodynamic Cancer Therapy through Iron-Doping and Oxygen-Vacancy Engineering of Piezoelectric Bismuth Tungstate Nanosheets. *Small* **2023**, *19* (24), 2300327. DOI: https://doi.org/10.1002/smll.202300327.

(55) Kim, B.; Brueggemeyer, M. T.; Transue, W. J.; Park, Y.; Cho, J.; Siegler, M. A.; Solomon, E. I.; Karlin, K. D. Fenton-like chemistry by a copper (I) complex and H2O2 relevant to enzyme peroxygenase C–H hydroxylation. *Journal of the American Chemical Society* **2023**, *145* (21), 11735-11744.

Chapter 6 Summary

Chapter 2 explored the use of a porphyrin derivative copper chlorophyllin to produce CuN_4 active site electrocatalysts for the two-electron oxygen reduction reaction. This was used for the direct disinfection of water sources by antibacterial and dye degradation testing. Chapter 3 was an expansion of this work now looking at tetraphenyl porphyrins, to examine the effects of different metal centers and organic side chains on the catalytic process. Chapter 4 pivots to semiconductive photocatalysts as a way to produce water disinfection catalysts with the need for a dedicated electrical source. Here TiO_2 was reduced to improve its visible light utilization. Chapter 5 is an expansion of that semiconductive work but applied to piezocatalysis, by doping reduced TiO_2 with other metal oxides both n-p heterojunctions and noncentrosymmetric crystalline structures can be produced. Creating a composite material that is highly effective in the production of reactive oxygen species and water disinfection.